UNIVERSITÀ
DEGLI STUDI
DI PADOVA

Sede Amministrativa: Università degli Studi di Padova

Dipartimento di INGEGNERIA DELL'INFORMAZIONE

SCUOLA DI DOTTORATO DI RICERCA IN : INGEGNERIA DELL'INFORMAZIONE
INDIRIZZO: SCIENZA E TECNOLOGIA DELL'INFORMAZIONE
CICLO: XXVI°

Characterization and Reliability of Dye-sensitized Solar Cells: Temperature, Illumination, and Bias Effects

Direttore della Scuola: Ch.mo Prof. MATTEO BERTOCCO
Coordinatore d'indirizzo: Ch.mo Prof. CARLO FERRARI
Supervisore : Ch.mo Prof. ANDREA CESTER Andrea Cester

Dottorando : DANIELE BARI
Daniele Bari

Abstract

Dye-sensitized solar cells (DSC) have recently proved to be a low-cost alternative to inorganic photovoltaics and they could attract a remarkable market share in the future. On the other hand, reliability issues must be solved to improve the competitiveness of this new solar energy technology. The present thesis deals with a characterization and reliability study of DSC aiming to have a comprehensive picture of the efficiency, stability, and degradation mechanisms of DSC, with the purpose to promote these devices as an alternative energy source in agreement with the European Community directions.

Since Michael Gratzel advanced the concept of sensitized materials and nanoporous semiconductors in 1991, dye-sensitized solar cells have attracted the interest of many academic and solar company researchers opening the road to photovoltaics of the third generation. Noticeable achievements in dye synthesis and wide band-gap semiconductor fabrication allow physicists, chemists, and engineers to produce more efficient and reliable DSC. At the time of this dissertation, DSC efficiency has reached 15% allowing them to compete with conventional inorganic photovoltaic systems in terms of cost and material complexity especially in those applications where the efficiency-to-production ratio cost must be maximized. There are several applications where the performances of photo-electrochemical solar cells are already sufficient: outdoor applications such as windows of buildings and greenhouse coverage; indoor applications such as windows, decoration structures, and shop windows. In spite of the advantages, many technological and reliability issues still have to be solved. Those include: the stability of the electrical characteristics, weak or damaged sealing, environmental related factors (i.e. UV exposure for outdoor applications), humidity, high temperature, and the improvement of DSC lifetime.

Intensive research is performed by researchers all around the world to understand the reliability and causes of instability in DSC: those efforts involve the study of many physic aspects including the effects of the different layers and materials, morphology, dyes, electrolytes, counter electrodes, growth conditions and the presence of oxygen and moisture.

The characterization methods used to understand and monitor the electrical properties of silicon-based solar cells cannot be used ”‘as is”’ for DSC without considering the completely different nature of DSC compared to silicon-based solar cells. Starting from the knowledge about the characterization of silicon base solar cells and a background on electrochemistry, we carefully transposed the same characterization technique to DSC. Access to full details of the devices and to ”‘ad hoc”’ structures for the analysis has been granted thanks to the collaboration with our University of Rome ”‘Tor Vergata”’.

We developed a measurement procedure, which allows us to define the standards for the characterization of dye-sensitized solar cells. This procedure is based on DC measurements as well as electrochemical impedance spectroscopy (EIS), the latter coming from electrochemistry. This technique allowed us to characterize DSC interfaces and identify which interfaces were been degraded during accelerated tests. This measurement set gives a comprehensive description of the behavior of all analyzed devices.

Our characterization and reliability study mostly involves the use of the AM1.5 solar simulator, where its spectrum spreads from UV to far IR wavelength. As an alternative illumination source, we designed a LED-based monochromatic light source in order to illuminate solar cells during characterization. We designed the illuminator as well as the driver circuitry. We found that these monochromatic sources trigger different portions of the solar cells' absorption spectrum as a function of the illumination source wavelength, giving the possibility of gathering additional information about DSC efficiency and degradation. In addition, during accelerated stresses we found that the degradation kinetic of open-circuit voltage, short-circuit current, efficiency, and fill-factor change if the characterization is performed with different illumination source wavelengths. This fact points out that characterization performed under monochromatic light could give additional information about the degradation mechanism behind DSC degradation.

To make a picture of DSC reliability, we carried out several accelerated stresses, stressing devices under different illumination sources. All these tests were carried out indoors. We analyzed the degradation of samples subjected to accelerated life tests with different illumination conditions and the role of the temperature on the device degradation by means of: the AM1.5 solar simulator, white LED, UV exposure, and both thermal and electrical stresses.

Since DSC gain heat during sunlight exposure thereby increasing their temperature, we examined the role of temperature on the DSC degradation. We showed that the temperature alone may strongly impact on the degradation rate of DSC reducing the overall DSC performance; in addition, we proved that the temperature has a twofold impact on cell performance. A moderate temperature induces an annealing process: it enhances the performances of the dye material likely recovering and rearranging some dangling or weak bonds at the transparent semiconductor interface or among the dye molecules. On the other hand, at high temperatures or for longer storage times regardless of the temperature level, the temperature strongly reduces the DSC performance as well as its lifetime.

In order to understand the effects induced by sun illumination exposure, we carried out accelerated optical stresses by means of AM1.5 solar simulator. Furthermore, we compared the degradation kinetics of DC parameters gathered from optical and thermal stresses. The responsible of the degradation during thermal or illumination stress is the formation of defects and chemical species at transparent semiconductor/sensitizer/electrolyte interface which reduces the charge transfer at interface and the ion migration across electrolyte. During optical stresses, we observed a main difference between the open-circuit degradation kinetics and the short-circuit degradation kinetics: the latter usually features a turnaround phase during optical stresses. The turnaround phase is strongly dependent on the illumination intensity used during the accelerated stress: the higher the illumination level, the shorter the turnaround phase. The device features faster degradation kinetics with higher illumination levels likely due increase of the interface temperature, as also confirmed by pure thermal stresses.

High power-to-weight ratio allows DSC to be used as solar energy harvester in space application. To make some light on the high energetic photons effects (even present at ground level) on DSC, we performed accelerated UV illumination stresses. We designed and assembled a UV illuminator as well as the driving circuitry. We found that UV exposure has detrimental effects on DSC and the main responsible for the cell failure during UV exposure is the electrolyte bleaching. It is worth to remark that the sensitizer seems to have a minor role in cell degradation as we proved. Concerning DSC studied in this Thesis, we strongly recommend some solutions in order to prevent electrolyte bleaching. Good UV filtering and encapsulation bring benefits for a reliable operation over time, even though they potentially go against the low weight and transparency nature of DSC.

High efficiency even at low illumination intensity or under diffused light allows DSC to be taken into account for indoor applications. We carried out accelerated stresses by means of high power white LED and we compared the DC parameters degradation kinetics as well as the EIS plot evolution measured by means both AM1.5 solar simulator and white-led illuminator. In addition, we proposed a white led-based illumination system as a cheap and versatile alternative to expensive AM1.5 solar simulator. We designed the white LED-based illuminator as well as the driving circuit. We found that white led exposure leads to the degradation of DSC performance and even though the white spectrum has not UV component, dye-molecules are not be able to absorb wavelength in the UV. Comparing white-led and AM1.5 solar simulator characterizations, we proved and showed that the latter provides more information than the former.

From the solar panel point of view, some DSC could be run into failure or be shaded during solar exposure. This likely real situation forces a single cell or a whole DSC string to work under certain bias conditions. To examine this non-trivial real condition, we designed and assembled current drivers and we performed forward and reverse biased constant current stresses (CCS) on dye-sensitized solar cells kept in the dark. We showed that DC parameters feature different degradation rates depending on that bias polarity and current intensity. We showed that forward CCS lead to the modification in the electrolyte composition, lowering the dark current of the cell while reverse CCS lead to the degradation of counter-electrode, accelerating the corrosion of the counter electrode by the electrolyte. In addition, we proved that most degradation occurs at those interfaces where the electrons are emitted during stress.

Sommario

Dye-sensitized solar cells (DSC) hanno recentemente dimostrato di essere un'alternativa a basso costo al fotovoltaico inorganico e in futuro non lontano potrebbero detenere una quota di mercato notevole. Tuttavia, i problemi di affidabilitá devono essere risolti per migliorare la competitivitá di questa nuova tecnologia. La presente tesi tratta la caratterizzazione e lo studio affidabilitá di DSC al fine di avere un quadro completo circa l'efficienza, la stabilitá e i meccanismi di degradazione nelle DSC, al fine di promuovere questi dispositivi come un nuova fonte di energia rispettando inoltre le normative della Comunitá Europea.

Da quando Michael Gratzel nel 1991 avanzò il concetto di materiali sensibilizzati e semiconduttori nanoporosi, dye-sensitized solar cells hano attirato l'interesse di molti ricercatori universitari e di aziende operanti nel fotovoltaico, aprendo cosíla strada al fotovoltaico di terza generazione. Risultati notevoli nella sintesi di cromofori sempre piú pancromatici e nella fabbricazione di semiconduttori ad ampio bad-gap, consentono a fisici, chimici ed ingegneri di produrre DSC sempre piú efficienti e affidabili. Al momento di questa tesi, l'efficienza delle DSC ha raggiunto il 13.4% il che consente loro di competere con i sistemi fotovoltaici inorganici convenzionali in termini di costi di produzione e complessitá materiale, in particolar modo in quelle applicazioni in cui il rapporto efficienza costi di produzione deve essere massimizzato. Ci sono diverse applicazioni in cui le prestazioni di queste celle solari foto-elettrochimiche sono giá sufficienti: applicazioni outdoor, come le finestre degli edifici e la copertura delle serre; applicazioni indoor come finestre, strutture di decorazione, e le vetrate dei negozi. Nonostante i vantaggi, molti problemi tecnologici e di affidabilitá devono ancora essere risolti. Alcune delle problematiche sono: stabilitá delle caratteristiche elettriche, incapsulamento, effetti dei fattori ambientali (ad esempio l'esposizione ai raggi UV per applicazioni esterne), l'umiditá, la temperatura elevata, l'incremento del lifetime. Un'intensa attivitá di ricerca é portata avanti da ricercatori di tutto il mondo per capire l'affidabilitá e le cause di instabilitá delle DSC: questi sforzi coinvolgono lo studio di molti aspetti fisici e chimici compresi gli effetti nell'uso di diversi materiali, strutture, morfologie, coloranti, elettroliti, controelettrodi, fabbricazione in condizioni e presenza di ossigeno e di umiditá.

I metodi di caratterizzazione utilizzati per caratterizzare celle solari silicon-based non possono essere utilizzati "'as is"' per le DSC senza considerare la diversa natura delle DSC rispetto alle celle silicon-based. Partendo dalla conoscenza nella caratterizzazione di celle solari silicon-based e da un background in elettrochimica, abbiamo attentamente trasposto i metodi di caratterizzazione alle DSC. L'accesso a tutti i dettagli tecnologici delle DSC sono disponibili grazie alla collaborazione con l'Universitá di Roma "'Tor Vergata"'. Abbiamo sviluppato una procedura di misura che permette di definire gli

standard per la caratterizzazione di dye-sensitized solar cells. Questa procedura si basa su misure DC e spettroscopia di impedenza (EIS), dove quest'ultima tecnica proviene dall'elettrochimica. Questa tecnica permette di caratterizzare le interfacce presenti nelle DSC e di identificare quali interfacce stanno degradando durante gli stress accelerati. Questo set di misure fornisce una descrizione completa delle celle e del loro comportamento durante gli stress accelerati.

La caratterizzazione e lo studio di affidabilitá viene esguita illuminando le celle con un simulatore solare AM 1.5, dove il suo spettro si estende dagli UV sino al lontano IR. Come fonte di illuminazione alternativa, abbiamo progettato una sorgente di luce monocromatica basata su LED per illuminare le celle solari durante la caratterizzazione. Abbiamo progettato l'illuminatore nonché la circuiteria di pilotaggio. Abbiamo scoperto che queste sorgenti monocromatiche eccitano una porzione diversa dello spettro di assorbimento delle celle: in particolare, la porzione dello spettro eccitata é funzione della lunghezza d'onda della sorgente di illuminazione. Ciò permette di avere ulteriori informazioni sull'efficienza e sulla degradazione delle DSC. Inoltre, durante gli aging test, abbiamo notato che la cinetica di degradazione della tensione di circuito aperto, della corrente di corto circuito, dell'efficienza, e del fill factor, cambia se la caratterizzazione viene eseguita con diverse lunghezze d'onda della sorgente di illuminazione. Questo fatto sottolinea che la caratterizzazione effettuata con luce monocromatica potrebbe dare ulteriori informazioni sul meccanismo di degradazione che causa il degrado delle DSC.

Per avere un quadro sull'affidabilitá delle DSC, abbiamo effettuato molti ageing test, con altrettante fonti di illuminazione o in generale di stress. Tutte queste prove sono state effettuate indoor. Abbiamo studiato il degrado delle celle sottoposte a stress accelerati con diverse condizioni di illuminazione e il ruolo della temperatura nel degrado delle celle. Questo studio é stato possbile effettuando stress accelerati per mezzo di: simulatore solare AM1.5, camere climatiche, illuminatore a LED bianco, illuminatore UV, e driver in corrente per gli constant current stress (CCS).

Poiché le DSC si scaldano durante l'esposizione alla luce solare e quindi la loro temperatura interna aumenta, abbiamo cercato di capire il ruolo della temperatura nella degradazione delle DSC. Abbiamo dimostrato che la sola temperatura può incidere fortemente sul tasso di degradazione delle DSC riducendo le prestazioni complessive delle celle; inoltre, abbiamo dimostrato che la temperatura ha un duplice impatto sulle prestazioni delle celle. Una temperatura moderata induce un processo di annealing: migliora le prestazioni del colorante probabilmente ristabilendo alcuni legami liberi o deboli all'interfaccia semiconduttore trasparente/colorante o tra le molecole di colorante. D'altra parte, a temperature elevate o per tempi piú lunghi di stress, indipendentemente dal livello di temperatura, la temperatura riduce fortemente le prestazioni DSC nonché il lifetime.

Per capire gli effetti indotti da esposizione alla luce solare, abbiamo effettuato stress ottici accelerati per mezzo di un simulatore solare AM 1.5. Inoltre, abbiamo confrontato la cinetica di degradazione dei parametri DC misuratu durante gli stress ottici e termici. Il responsabile della degradazione durante lo stress termico o ottico é la formazione di difetti e di specie chimiche all'interfaccia tra il semiconduttore trasparente/dye/elettrolita i quali riducono la capacitá di trasferimento di carica all'interfaccia e la migrazione degli ioni attraverso l'elettrolita. Durante gli stress ottici, abbiamo osservato una chiara differenza tra la cinetica di degradazione della tensione di circuito aperto e la cinetica di degradazione della corrente di corto circuito: quest'ultimo solitamente presenta una fase di inversione di tendenza durante gli stress ottici. La fase di inversione di tendenza é fortemente dipendente dalla intensitá di illuminazione utilizzata durante lo stress accelerato: maggiore é il livello di illuminazione, minore é la durata della fase di inversione di tendenza. La degradazione della cella é piú veloce con livelli di illuminazione piú elevati probabilmente dovuta all'aumento della temperatura di interfaccia, come confermato anche dagli stress termici puri.

L'elevato rapporto efficienza-peso consente alle DSC di poter essere utilizzate come fonte di energia in applicazioni spaziali. Per indagare gli effetti di fotoni ad alta energia (presenti anche a livello del suolo) sulle DSC, abbiamo effettuato stress accelerati utilizzando una fonte di illuminazione UV. Abbiamo progettato e assemblato un illuminatore a raggi UV, cosícome il circuito di pilotggio. Abbiamo scoperto che l'esposizione ai raggi UV ha effetti negativi su DSC e il principale responsabile della degradazione delle celle durante l'esposizione ai raggi UV é il bleaching dell'elettrolita (scolorimento dell'elettrolita). Vale la pena notare che il dye sembra avere un ruolo secondario nella degradazione della cella come é stato dimostrato. Per quanto riguarda le DSC studiate in questa tesi, si consiglia di adottare alcune soluzioni per evitare il bleaching dell'elettrolita. Il filtraggio UV e un buon incapsulamento potrebbero portare benefici per un funzionamento affidabile nel tempo, anche se potenzialmente vanno contro il peso contenuto e la naturale trasparenza delle DSC.

Alta efficienza anche a basse intensitá di illuminazione o con luce diffusa permette alle DSC di essere prese in considerazione per applicazioni indoor. Abbiamo effettuato ageing test tramite LED bianchi ad alta potenza e abbiamo confrontato la cinetica di degradazione dei parametri DC cosícome l'evoluzione dell'impedenza (EIS). Queste caratteristiche sono state misurate illuminando le celle sia con simulatore solare AM 1.5 che con un illuminatore a LED bianchi. Congiuntamente allo studio di affidabilitá, abbiamo proposto un sistema di illuminazione basato su LED bianchi come un'alternativa economica e versatile ai costosi simulatori solari AM 1.5. Abbiamo progettato l'illuminatore basato su LED bianchi cosi come il suo circuito di pilotaggio. Dai risultati raccolti durente gli stress, abbiamo scoperto che l'esposizione alla luce bianca porta al degrado delle prestazioni delle DSC. Anche se lo spettro bianco non ha componente UV, le molecole del dye non sono piú in grado di assorbire lunghezze d'onda nella regione UV. Confrontando le caratteristiche (DC ed EIS) misurate con il simulatore solare a LED bianchi e con il simulatore solare AM 1.5, abbiamo mostrato e provato che quest'ultimo fornisce piú informazioni rispetto al primo.

Dal punto di vista pannello solare, alcune DSC potrebbero incorrere in guasti o essere ombreggiate durante l'esposizione solare. Tale situazione potrebbe verificarsi nel caso in cui una cella/stringa di un pannello solare non sia funzionante oppure sia in ombra e non siano state adottate soluzioni atte a prevenirne una condizione operativa non convenzionale (ovvero non sono presenti diodi di by-pass o blocking diode). Per esaminare questa condizione reale non banale, abbiamo progettato e assemblato diversi driver di corrente e abbiamo eseguito molti constant current stress (CCS). I CCS eseguiti sono di due tipi: postive CCS e negative CCS. Il primo prevede di polarizzare la cella in modo tale che la corrente scorra nello verso che scorre quando esposta a luce solare, cioé in condizione standard di funzionamento; negative CCS, prevede di polarizzare la cella nel senso opposto al positive CCS. Durante gli stress le DSC vengono mantenute al buio, per evitare effetti dovuti all'illuminazione. Dai dati raccolti durante i due tipi di CCS, si é potuto envincere che entrambe portano ad una degradazione delle performance della cella e che all'aumentare del modulo della corrente di stress diminuisce il tempo di vita della DSC. Osservando le caratteristiche DC delle celle stressate, positive e negative CCS degradano le DSC in maniera diversa: i primi portano ad un degrado lento e costante della cella, i secondi, apparentemente non degradano le celle in maniera significativa all'inizio dello stress, ma ne causano un'improvvisa e rapida degradazione (sudden failure) dopo diverse ore. L'istante in cui si verifica il sudden failure della DSC é funzione dell'intensitá della corrente di stress. Abbiamo mostrato che durante i positive CCS, la composizione elettrolita cambia, abbassando la dark current della cella solare, mentre i negative CCS portano alla degradazione del contro-elettrodo, accelerandone la corrosione da parte dell'elettrolita. Inoltre, abbiamo dimostrato che la maggior della degradazione avviene alle interfacce in cui gli elettroni sono emessi durante lo stress. I risultati ottenuti, dimostrano che i CCS hanno effetti irreversibili sulle prestazioni elettriche delle DSC e che alcune soluzioni circuitali devono essere adottate allo scopo di prevenire inoppurtune condizioni di funzionamento delle celle.

Acknowledgements

My sincere thanks to Prof. Andrea Cester for the tutoring during my Ph.D. course.

Besides my tutor, I would like to thank the rest of MOST group: Prof. Gaudenzio Meneghesso and post-doc Nicola Wrachien for their help during the last four years.

In addition I would like to thank all the colleagues of the u-Lab at the Department of Information Engineering of the University of Padua, Italy.

A special thank to Prof. Aldo Di Carlo and CHOSE for supplying all the devices studied in this work and for the insightful comments and suggestions.

I would like to thank Prof. Sue A. Carter and Glenn B. Alers for giving me the chance to spend a pleasant and priceless stay at the Physics Department at the University of California at Santa Cruz.

A special thank in advance to the reviewer(s) for reading my thesis and for the useful suggestions and valuable comments that I will receive.

Contents

List of Figures

List of Tables

Chapter 1

Introduction

The energy can be considered as the engine of technological, economic, and social development of a country. At the time of this dissertation, fossil fuels have been the main sources of energy production, but the depletion of oil, coal and natural gas is causing their inevitable exhaustion. Concern with the significant environmental impact and the prospect for depletion of traditional energy sources has produced a great interest in renewable energy sources. Today, most of the important renewable resources are: biofuel, biomass, ethanol fuel, geothermal, hydropower, solar energy, tidal power, wave power, and wind power. Among these resources, solar energy stands out as inexhaustible energy

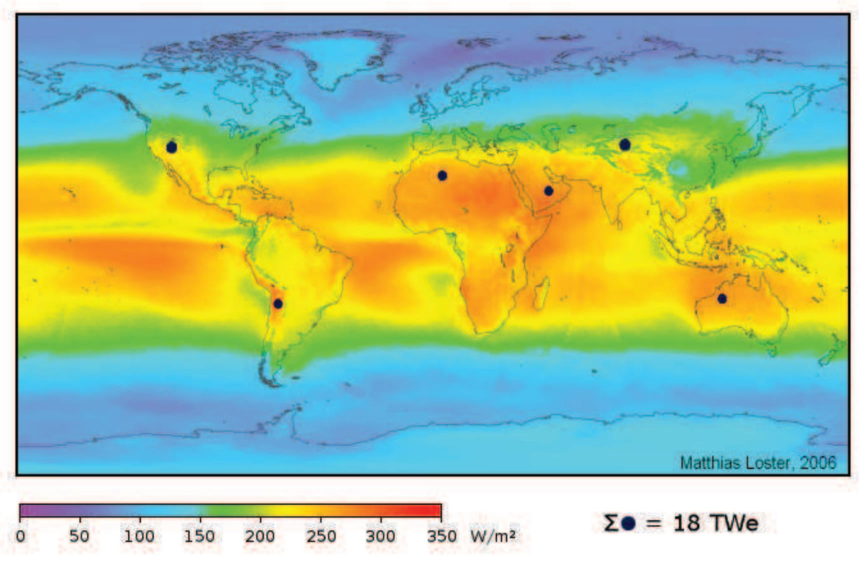

FIGURE 1.1: Average sun exposure showing land area (small black dots) required to replace the world primary energy supply with solar electricity (18 TW is 568 Exajoule, EJ, per year). Sun exposure for most people is from 150 to 300 W/m^2 or 3.5 to 7.0 kWh/m^2/day.

source with an unquenchable source of life, which can be continuously used to meet our growing energy needs.

Photovoltaics is the key to exploit the solar energy.

Photovoltaics (PV) is a method that generates electrical power, which is measured in Watts (W) or kiloWatts (kW), by converting solar radiation into direct current (DC) by means of semiconductors that exhibit the photovoltaics effect[1]. As long as light is shining on the solar cell (the name for the individual PV element), it produces electrical power. When the light stops, the electricity stops. Solar cells never need recharging like a battery and some have been working in continuous outdoor operation on Earth or in space for over 30 years.
Although the traditional photovoltaics technologies have gained a considerable market share, high production and installation costs and the competition with other renewable energies still limit the spread and use them as a serious alternative to fossil fuels.
Table 1.1 shows the most important advantages and disadvantages of photovoltaics listing both technical and nontechnical issues. In many cases, the advantages and disadvantages of photovoltaics are almost completely opposite to conventional fossil-fuel power plants. For instance, disadvantages of fossil-fuel energy plants are: a wide range of environmentally hazardous emissions, parts which wear out, steadily increasing fuel costs, and low public opinion. Photovoltaics suffers none of these problems. Notice that several of the PV disadvantages reported in Table 1.1 are nontechnical but relate to economics and infrastructure and they are partially compensated by a very high public acceptance and awareness of the environmental benefits. Concerning low public opinion, photovoltaics may suffer of that in those place where the artistic heritage is extremely important. During the late '90s, the average growth rate of PV production was over 33% a year.

The today photovoltaic market is dominated by silicon-based devices. The monocrystalline and polycrystalline (even more if nanocrystalline) silicon solar cells have good reliability and efficiency, nevertheless they still have in the high cost their real Achilles' heel. Although several form of incentives in order to purchase solar panels, the price of kW/peak obtained from photovoltaic silicon is not yet affordable by the most of the private customers, and it makes convenient the consumption of electricity produced from fossil fuels. The amorphous silicon-based photovoltaic features instead lower yields than

---

[1] The photovoltaic effect is the creation of voltage or electric current in a material upon exposure to light.

Table 1.1: Advantages and disadvantages of photovoltaics

Advantages	**Disadvantages**
Fuel source is vast and essentially infinite	Fuel source is diffuse (sunlight is a relatively low-density energy)
No emissions, no combustion or radioactive fuel for disposal (does not contribute perceptibly to global climate change or pollution)	High installation costs
No moving parts (no wear)	Poorer reliability of auxiliary (balance of system) elements including storage
Ambient temperature operation (no high temperature	Lack of widespread commercially available system integration and installation so far
Low operating costs (no fuel)	Lack of economical efficient energy storage
High reliability in modules (>20 years)	
Modular (small or large increments)	
Quick installation	
Can be integrated into new or existing building structures	
Can be installed at nearly any point-of-use	
Daily output peak may match local demand	
High public acceptance	
Excellent safety record	

the previous, but also a much lower cost. However, the lower price is not that low to ensure advantageous investment, at least for small size systems.

The streets that scientists and researchers are pursuing to boost photovoltaic technology aim to two main goals. On the one hand, improving the performance of the silicon-based solar cells, adopting multi-junction structures and concentration system allowing, for the same conversion efficiency, the reduction of the photo-active surface and/or the increase electrical power gained. On the other hand, many efforts have been spent into the research of new technologies, such as the thin-film (TF) technology, which could be an alternative (some of them are already available on the PV market) to the actual technology in terms of costs and/or application fields.

The main TF alternatives to silicon-based PV technology are: cadmium telluride (CdTe), copper indium gallium selenide (CIS or CIGS), organic and polymeric solar cells (OPV), and dye-sensitized solar cells (DSC). These technologies will be discussed further in section 2.5. Among those alternatives, the use of organic-based solar cells, either they are purely organic thin-film cells or dye-sensitized solar cells, are gaining the interest of academic researchers and of R&D branch of many solar companies. The efficiencies achievable by these solar cells are not yet comparable to those that can be achieved with current technology, but the continuous studies and improvements of these devices have led to a gradual technology improvement. The DSC are the closest to the current technological maturity with performance comparable to those Si-based thin-film devices.

Since Michael Grätzel advanced the concept of sensitized materials and nanoporous semiconductors, dye-sensitized solar cells have been intensively studied [1, 2]. Due to the low production and material costs, and the suitability to many applications, this type of photochemical solar cells could detain a remarkable share in the renewable-energy market in the future. Moreover, DSC can be fabricated on many different types of substrates such as polymers, flexible materials, glass, etc. [3–5]. In particular, the study and improvement of the DSC technology is rapidly bringing to good results on efficiency: these results are very similar and in some cases even higher than those of amorphous silicon technology. So far, this type of solar cell have recently reached global AM 1.5 (100mW/cm^2) power conversion efficiencies of 15% [6]. Chapter 3 will go over details of DSC structures, materials, and working principle.

Even though many efforts have been spent in the research of newer and more efficiency materials, the stability and reliability of DSC is still an open and critical issue. The materials used to fabricated DSC are in fact sensitive to temperature changes and ultraviolet radiation exposure, and react easily with oxygen and water when exposed to air. Since these devices are predominantly still experimental, there are no well documented explanations about those issues and in turn there are no estimations of their lifetime in various environmental and operating conditions. On the other hand, the reliability of the silicon-based competitor technology is well understood and it provides a solar panel lifetime of at least 20 years, after that a decrease in the efficiency to more than 20% is expected. This points out that more work on the understanding of DSC reliability becomes paramount to bring this technology to fruition. Therefore, in order to allow DSC to have competitive lifetime, it is essential to assess the stability and reliability determining the main causes of degradation under sunlight exposure.

1.1 Work presented in this dissertation

This work presented in this dissertation dealt with the characterization and the reliability study of dye-sensitized solar cells, in order to get a comprehensive picture and add a contribution to the knowledge of the DSC technology. The whole work was carried out at Molecular & Organic Semiconductor LAB (MOSLAB) at the Department of Information Engineering at University of Padua (Italy) and all the devices studied were fabricated and provided by Center for Hybrid and Organic Solar Energy (CHOSE) at the University of Rome "'Tor Vergata"' (Italy). The characterization phase was extremely important: it aimed to understand which of the characterization methods used for Si-based solar cells apply to DSC, and to which not, to try to adapt them, carefully tuning measurement parameters. In addition, we borrowed measurement techniques from electro-chemistry and other new measurements were explored. This phase required a lot of bibliography search and chemistry/physics studies in order to be aware of the state of the art and understand the chemical and physical processes involved in the DSC working principle respectively. Due to the results obtained from the characterization phase, this work provided CHOSE a significant feedback in order to identify the most effective technology improvement and/or the best design rules to fabricate stable, efficient, and reliable DSC to be competitive on the renewable energy market. Concerning the reliability study, this work provides a DSC failure analysis trying to figure out the physical and chemical processes that lead to the degradation of these solar cells under sunlight exposure and, in turn, a forecast of the lifetime. In order to accomplish this purpose, several reliability tests were performed by means of accelerated stresses. Chapter 4 goes over details of this technique. More in specific, the reliability study cast some light on the effects of: sun and white light and ultraviolet exposure with different bias of the devices, thermal soaking and constant current stresses in dark. Chapter 5 goes over details about the results and discussion of accelerated stresses. Chapter 6 summarizes the results of the accelerated stresses, possible technological solutions, final statements and remarks on this work.

Chapter 2

Photovoltaics

2.1 History of Photovoltaics

The history of photovoltaics (PV) dates back to the 19^{th} century, as shown in Table A.1 in the Appendix A. The progenitor of the solar cells in use today was invented, or rather discovered, at the end of the second half of the nineteenth century, during the construction of the first communications network in the world seamlessly through transoceanic telegraph cables. During the deposition of the cables on the sea floor, engineers used selenium to verify the integrity of submerged cables, and while working with this material, they found that the performance of selenium were strongly influenced by the amount of sunlight that shone. This discovery aroused considerable interest among scientists from all over Europe, including William Grylls Adams and Richard Evans Day latter during one of their experiments on selenium observed as the solid material, whether radiated by sunlight, could generate electricity.

At that time, science was not able to explain why selenium was able to produce electricity when struck by sunlight and most of the scientists scoffed at the work of Adams and Day. Later, however, in the mid-twenties, some scientists theorized that when sunlight strikes a material such as selenium, there are packages of photons with enough energy to rip electrons less bound to their atomic orbital. Some researchers imagined how the modules of solar cells based on selenium could provide electricity for factories and homes. Despite efforts, no one was able to realize that the selenium solar cells can convert a little more than half percent of the incident light energy into electricity. This certainly did not play in favor of PV, thus deferring the use as a possible source of supply of electricity.

The first functional, intentionally made PV device was by Fritts [7] in 1883. He melted Se into a thin sheet on a metal substrate and pressed a Au-leaf film as the top contact.

It was nearly 30 cm^2 in area. He proposed that the current, if not wanted immediately, can be either stored where produced, in storage batteries, or transmitted a distance and there used. This man foresaw today's PV technology and applications over a hundred years ago.

The turning point, and then in turn the modern era of photovoltaics, was in 1954 when researchers at Bell Labs in the USA accidentally discovered that silicon-based pn junction diodes generated a voltage when the room lights were on: Gerard Pearson and Calvin Fuller were the pioneers in the design of the first silicon transistor, by theorizing the production of the first devices. In particular Fuller came up with a technique change the characteristics of the semiconductor introducing impurities ("‘doping"’) into the silicon. Fuller gave Pearson a portion of a doped silicon, on which Pearson carried out a series of experiments to evaluate their characteristics. Among these experiments there was also the exposure to sunlight and electrical characterization: unexpectedly Pearson observed that exposing the doped silicon to solar radiation, it was capable of producing an electric current five times higher than that obtained by the devices based on selenium. After many experiment and a lot of efforts, Bell Laboratories disclosed the world the first solar cell can provide an appreciable amount of power [8].

In 1955, the U.S. government announced the intention to launch satellites, provided with solar panels made of of silicon-based solar cells in order to provide for their energy needs. Unlike satellites powered by the battery pack, which lost efficiency in a short time, the launch of the Vanguard satellite demonstrated the value of silicon solar cells. The communications with the earth in fact continued for several years, and were also completed many experiments [9]. Within a year, they had produced a 6% efficient Si pn junction solar cell [10]. In the same year, the group at Wright Patterson Air Force Base in the US published results of a thin-film hetero-junction solar cell based on Cu_2SCdS also having 6% efficiency [11].

In 1956, GaAs pn junction solar cell by RCA Lab scored a 6% efficiency in the US [12]. By 1960, many significant works by Prince [13], Loferski [14], Rappaport and Wysoski [15], Shockley (a Nobel laureate) and Queisser [16], developed the fundamentals of pn junction solar cell operation including the theoretical relation between band gap, incident spectrum, temperature, thermodynamics, and efficiency. Thin films of CdTe were also produced, giving cells with 6% efficiency [17]. By this time, the U.S. space program was utilizing Si PV cells for powering satellites. Since space was still the primary application for photovoltaics, studies of radiation effects and more radiation-tolerant devices were made using Li-doped Si [18].

In 1970, a group at the Ioffe Institute led by the nobel prize awarded Alferov, in the USSR, developed a heteroface GaAlAs/GaAs [19] solar cell which figured out one of the main problems that GaAs devices had been experiencing till that time and pointed the way to new device structures. GaAs cells gained interest due to their high efficiency and their resistance to harsh environment, especially against the ionizing radiation in outer space. The year 1973 was a milestone for photovoltaics, in both technical and nontechnical areas. A significant improvement in performance was recorded in 1973 scored by the ”‘violet cell”’ having an improved short wavelength response leading to a 30% relative increase in efficiency over the current most developed and efficient devices, that is Si cells [20]. GaAs hetero-structure cells were also developed at IBM in the USA having 13% efficiency [21].

In the 1980s, manufacturing facilities for producing PV modules from Si wafer pn junction solar cells were built in the USA, Japan, and Europe. New technologies began to move out of the government, university and industrial laboratories, and into precommercialization or ”pilot” line production. Companies attempted to scale up the thin-film PV technologies like a-Si and $CuInSe_2$, which had achieved >10% efficiency for small area (1 cm^2) devices made with carefully controlled laboratory scale equipment. Much to their disappointment, they found that this was far more complicated than merely scaling the size of the equipment. Most large US semiconductor companies, gave up their R&D efforts (IBM, General Electric, Motorola) lacking large infusions of private or government support to continue. One common result was the purchase of American companies and their technologies by foreign companies [8].

In the 90s another momentous step in the PV growing was made, that is with the birth of the building integrated PV (BIPV [22]), where PV cells are incorporated into a standard building product, such as a window or a roof shingle, or into an architectural feature like an exterior sun awning or semitransparent skylight. In this way, the cost of the PV is partially lowered by the cost of the building materials, which would have been required anyway, and then the incremental cost of the photovoltaics is much lower. The success of grid-connected residential or BIPV commercial applications has been possible because several countries led by Germany have established high rates o pay for the PV electricity produced by solar installations in private houses. In this scenario, the installation owner receives \$0.5/kWh for the electricity they feed into the public electric grid (as of 2001). But the owner buys the electricity consumed in their own house at the normal cost of about \$0.1/kWh from the grid. Additionally, German banks provided generous loans for purchasing the installation. Similar concepts are used in Spain, the Netherlands, and other countries in Europe. But, the success has been still bigger in Japan where home-builders receive a rebate from the government for about 30% of the PV system cost. Then, their electric bill is determined by the utility using the ”‘net metering”’ where the customer pays only the net difference between what they used and what they generated. Rebates and net metering are available in some, but not all, states in the USA as of 2002. Interestingly, government support of photovoltaics in Japan has been decreasing while the market for PV homes has continued showing an impressive growth rate [8].

From late '50s to the present day solar cells have taken on an increasing importance in the production of electricity from alternative sources. The birth of the Kyoto Protocol has sanctioned the choice of participating countries, including those outside the European Union, to drastically reduce CO_2 emissions, establishing substantial financial penalties against Member States that exceed their quotas. AppendixB describes the European Standards and regulation. This choice can not be separated from a project

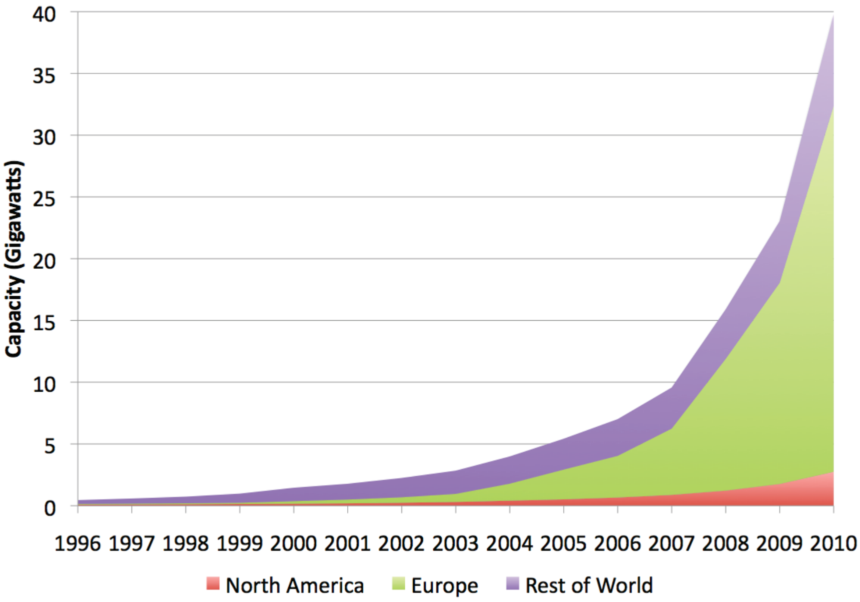

FIGURE 2.1: Electric power from photovoltaics by country. Date update till 2010 [23].

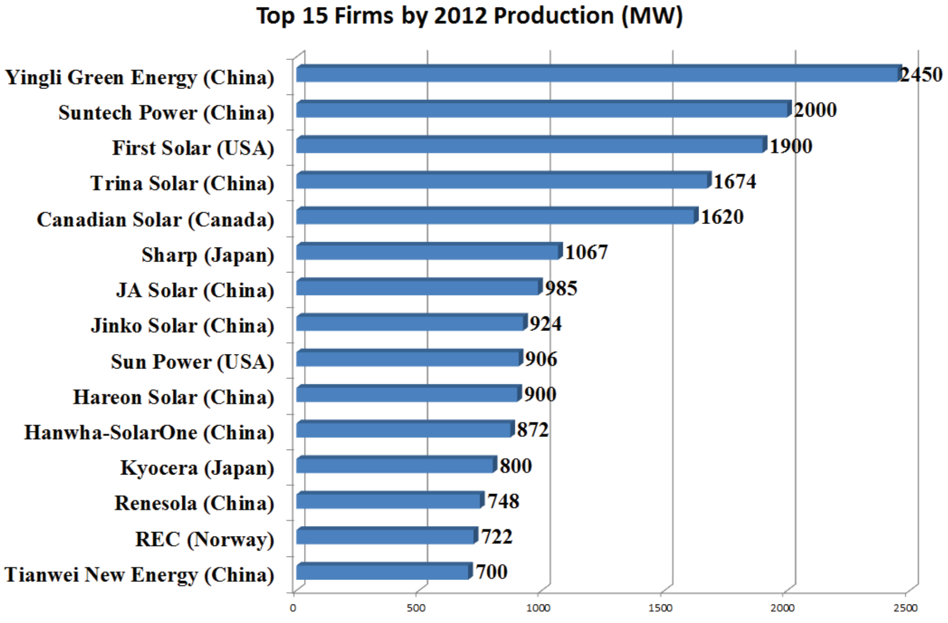

FIGURE 2.2: The chart mentions the top 15 global manufacturers of solar cells in 2012 [24], [25].

and an energy supply system in which the use of coal as a raw material is less preponderant, without going to affect the economic development of industrialized countries and emerging countries. In this context there is a clear need for each country to diversify as much as possible their energy, giving more space to renewable energy sources such as photovoltaic, see Fig. 2.1.

2.2 Solar Energy

The solar radiation is the electromagnetic energy radiated by the Sun as a result of thermonuclear fusion reactions of hydrogen into helium atoms. The amount of solar radiation that reaches the earth is huge, about ten thousand times greater than all the energy used by world population.

The average amount of solar energy that orthogonally hit a spherical surface placed outside the atmosphere per unit of time is called the solar constant and has the average value of 1353 W/m^2. This value is meant to be as an average reference value since the power oscillates, especially, due to the periodic variation of the distance earth sun.

While crossing the Earth's atmosphere, solar radiation undergoes different effects.

A part of the sunlight is reflected back toward the space mainly by the clouds; another part is scattered in all directions due to the interaction with the air, which is composed by: nitrogen, oxygen, water vapor, carbon dioxide, and ozone; a part is absorbed by these molecules which make warm the atmosphere: they absorb the solar radiation and remit as infrared radiation; finally a part reaches the Earth's surface.

The diffuse radiation is the sum of the radiation scattered by the atmosphere and the infrared radiation emitted by the air molecules after solar radiation absorption; the direct radiation is the proportion of solar radiation that reaches the Earth's surface directly. An inclined surface may also receive radiation reflected from the ground, by water or by other horizontal surfaces. This contribution is called albedo.

The amount of direct and diffuse radiation and albedo collected by a surface depends on:

- the weather conditions. On a cloudy day, the radiation is almost totally diffuse while on a clear day with dry weather the predominant direct component which can reach up to 90% of total radiation;
- the inclination of the surface with respect to the horizontal plane. A horizontal surface receives the maximum direct radiation and minimum reflected radiation;
- the presence of reflective surfaces. The greatest contribution to the reflected radiation is given by clear surfaces: so the reflected radiation increases in the winter

due to the snow and iced surfaces and decreases in summer due to the strong absorption by the grass or the ground.

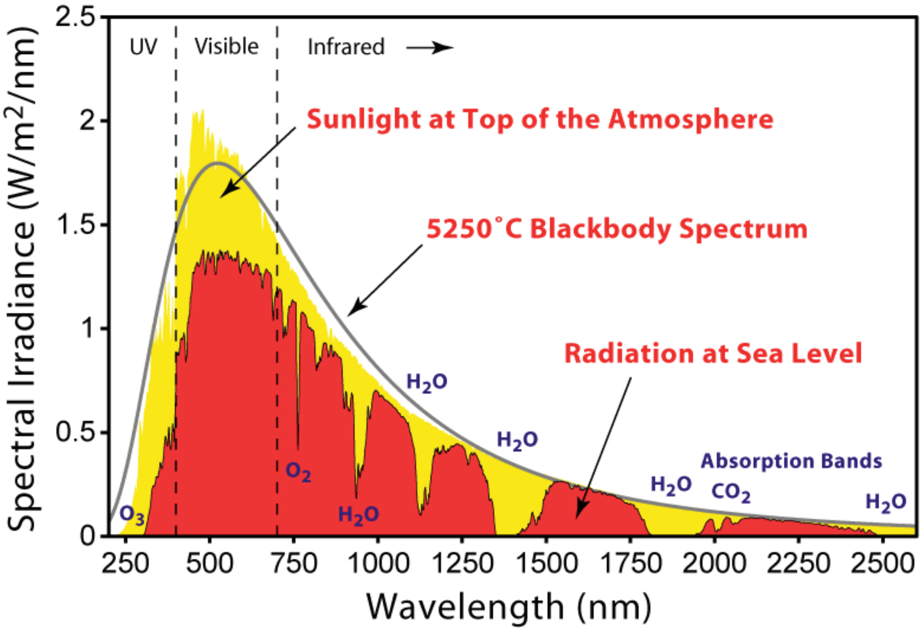

FIGURE 2.3: Solar spectral irradiance [26].

The spectral distribution of solar radiation (see Fig. 2.3) that reaches the earth's surface depends on the composition of the atmosphere: the ground solar energy is concentrated in the range of wavelength between 200nm and 2500nm and its spectral composition is (the percentages refer to the total sun irradiance):

- 200nm - 380nm: ultraviolet (UV), 6.4%;
- 380nm - 780nm: visible (VIS), 48%;
- 780nm - 2500nm: infrared (IR), 45.6%.

The power density of the solar radiation reduces with the gradually increase of the thickness of the air layer crossed. Typical values can range between 1000 and 300W/m^2. The value of 1kW/m^2 (or equivalently 100mW/cm^2 which is also called 1Sun) corresponds to the maximum radiation on the ground surface with the sun at its zenith and with a atmosphere perfectly transparent. To quantify the power density that reaches the Earth's ground according to the position of the Sun and the atmosphere effects, people usually refer to the concept of Relative Air Mass or simply Air Mass (AM).
Given θ the angle between the position of the Sun and the zenith and h is height of the Sun respect to the ground, the distance d traveled by the light through the atmosphere is equal to:

$$d = \frac{h}{\cos\theta} \tag{2.1}$$

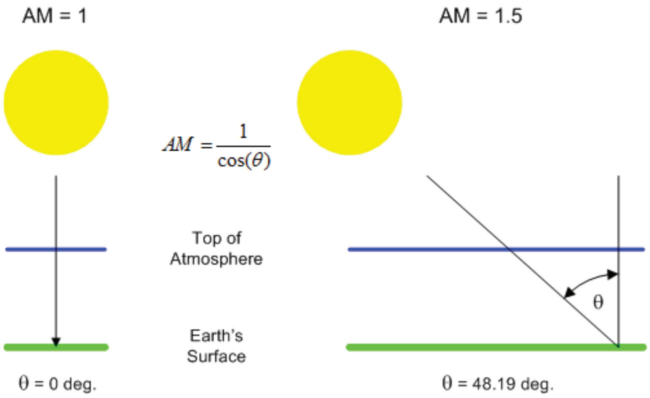

FIGURE 2.4: Air mass: schematic definition.

Out of the atmosphere the AM index is taken as reference and referred to as AM0. On the Earth's surface is mathematically expressed as:

$$AM = \frac{1}{\cos\theta} \rightarrow d = h \cdot AM \tag{2.2}$$

In the following list, some of the values of the AM index are reported as a function of the angles of elevation of the Sun respect to the zenith:

$$\theta = 0 \rightarrow AM = 1(AM1) andd = h \tag{2.3}$$

$$\theta = 60 \rightarrow AM = 2(AM2) andd = 2h \tag{2.4}$$

$$\theta = 48 \rightarrow AM = 1.5(AM1.5). \tag{2.5}$$

AM1.5 is considered the standard in laboratory tests for the characterization of solar cells.

2.3 Photovoltaic effect: basic concept

At the time of this dissertation, the majority of solar cells present in the market are made of semiconductors, which have weakly bonded electrons occupying a band of energy called the valence band. When energy exceeding a certain threshold, called the band gap energy, is applied to a valence electron, the bonds are broken and the electron is somehow free to move around in another band called the conduction band where it can conduct electricity through the material. Thus, the free electrons in the conduction band are separated from the valence band by the band gap. This energy needed to promote the electron into the conduction band can be provided by photons, which are particles of light. Fig. 2.5 shows a representation of the photovoltaics effect. When the solar cell is exposed to sunlight, photons hit the electrons in the valence band, breaking the bonds

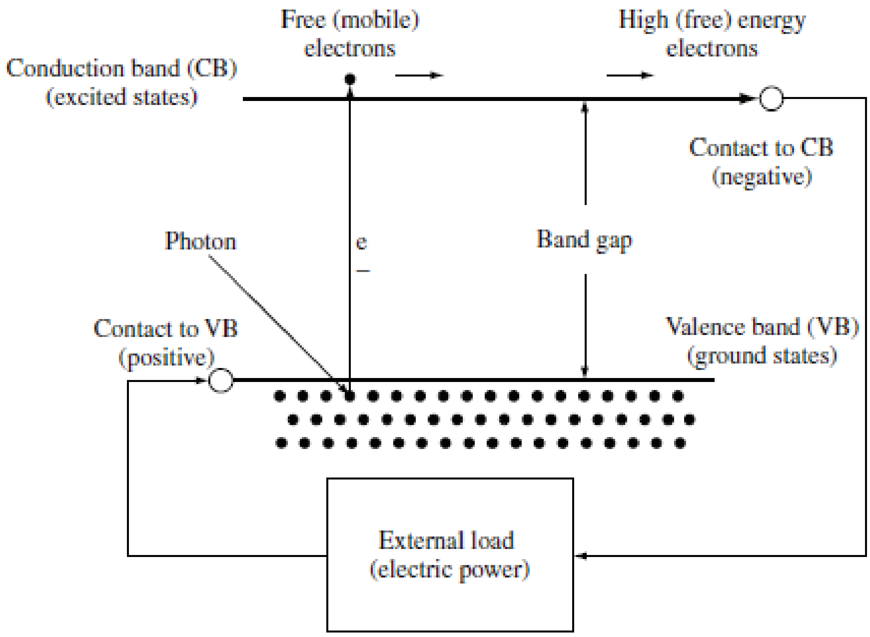

FIGURE 2.5: Schematic of PV effect in a solar cell. Electrons are pumped by photons from the valence band to the conduction band. There they are collected by a contact selective to the conduction band and delivered to the external circuit, where they do work, then are returned to the valence band.

and pumping them to the conduction band. This phenomenon is called photovoltaic effect. The solar cell has two contacts: one of the contact collects the electrons present in conduction-band of the semiconductor and it drives such electrons to the external circuit. The other contact collects the electrons coming from the external circuit and restores them to the solar cell. The electrons lose their energy by doing work) flowing through the external circuit, for example pumping water, spinning a fan, powering a sewing machine motor, a light bulb, or a computer. They are restored to the solar cell by the return loop of the circuit via a second selective contact, which returns them to the valence band with the same energy that they started with. The movement of these electrons in the external circuit and contacts is called the electric current. The potential at which the electrons are delivered to the external circuit is slightly less than the threshold energy that excited the electrons; that is, the band gap. Thus, in a material with a 1 eV band gap, electrons excited by a 2 eV photon or by a 3 eV photon will both still have a potential of slightly less than 1 V (i.e. the electrons are delivered with an energy of 1 eV). The electric power produced is the product of the current times the voltage; that is, power is the number of free electrons times their potential.

Sunlight has a photons with an energy that spreas all over its spectrum. Only those photons with energy greater than the band gap energy can excite electrons from the valence to conduction band where they can exit the device and generate electrical power, as described above. Photons with energy less than the energy gap fail to excite free

electrons and they travel through the solar cell and they are absorbed at the rear producing heat or being reflected. Solar cells in direct sunlight can be somewhat (20–30°C) warmer than the ambient air temperature. The heart of the most common used solar cells is the pn junction and modeling and understanding is very much simplified when the pn junction concept is adopted. This pn junction comes from the intimate contact between an N-doped and P-doped semiconductors: the fist has an excess of negative (n-type) charge while the second has an excess of positive charge (p-type).
Silicon (Si), one of the most abundant materials in the Earth's crust and the most known in the electronics filed, is the semiconductor used in monocrystalline (c-Si) and polycrystalline (poly-Si) form for almost 90% of the PV applications today. Other semiconductors can be used for PV and surprisingly they are better suited to absorb the solar energy spectrum. These other materials has been extensively developed and they are already commercialized. They are called thin-film semiconductors, of which amorphous silicon (a-Si), copper indium gallium diselenide ($Cu(InGa)Se_2$ or CIGS), and cadmium telluride (CdTe) receive most of the attention, see section 2.5 [8].

2.4 State of the Art

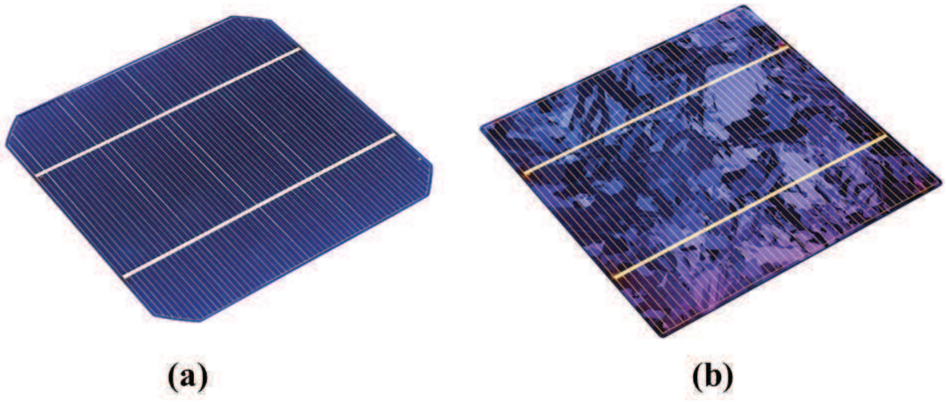

FIGURE 2.6: (a) Monocrystalline solar cells, (b) poly crystalline solar cells. Unquestionable leaders in the PV market.

The material more widespread for the production of photovoltaic cells is undoubtedly the crystalline silicon (c-Si), which covers about 84-90% of the world production. The silicon monocrystalline, obtained from crystals of high purity, allows to obtain cells with efficiencies greater than or equal to 21% [27] and it detains about the 37% of PV market share. About 48% of the market for silicon-based solar cells are produced using polycrystalline silicon (poly-Si), see Fig. **??**, which allows to produce cheaper solar cells but at the expense of efficiency, which ranges between 11-15%. Despite the low cost of maintenance and the remarkable longevity (20-25years), the main issues concerning Si-based PV is still the high costs to install and have a system connected to the grid,

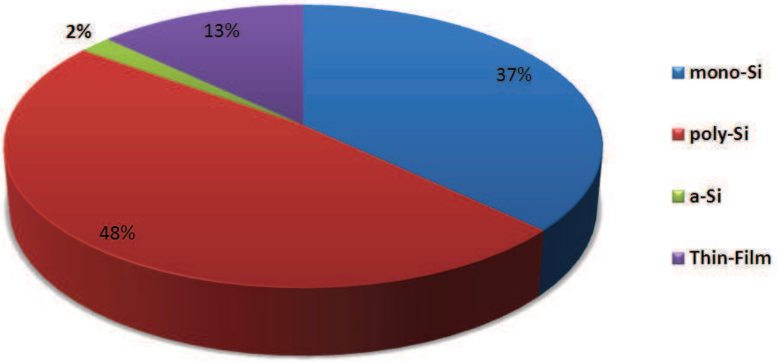

Figure 2.7: Market share of the different PV technologies in 2010.

which is around 6000 €/kWp. Besides various forms of incentives, the cost of energy from Si-based solar panel ranges between 0.25-0.4 €/kWh, making it non-competitive with energy produced by conventional sources (i.e. fossil fuels) [28].
In order to lower the cost of the Si-based PV technology, the research has undertaken two main roads to deal with the incomplete market competitiveness of traditional photovoltaic technology:

- increase the ratio efficiency to modules surface, in order to have a lower panel surfaces with the same energy gained or, alternatively, the same panel size with a higher electrical power gained. In this case, the research focuses on:
  - multi-junction cells: they are made by the "‘overlapping"’ of multiple cells made by different semiconductor compound which are characterized by a different value of the energy gap. In this way, each junction absorbs a certain portion of the solar spectrum and consequently are able to absorb a wider band of the solar spectrum than a single junction solar cells; overall efficiency can even reach 38%. Although this solution allows to obtain high efficiency solar cells, it requires a more sophisticated fabrication process;
  - solar concentrator: through the use of optical systems based on mirrors or lenses or both is possible to concentrate the solar radiation flux on areas of semiconductor material reduced and targeted. Since the most expensive element is the silicon, which forms the active area of the cell, the less material used, the less then the cost of the device. It is also possible to create a cogeneration system using the thermal energy of the cooling system of the cells; using concentrator system with multi-junctions solar cell can reaches and efficiency of about 45%;
- reduce the cost of production:

- thin-film technology, which allows to strongly reduce the amount of material used and uses low cost fabrication process;
- nanostructured cells: they are now in the initial search state; offer promising potential, by virtue of nanoscale dimensions.

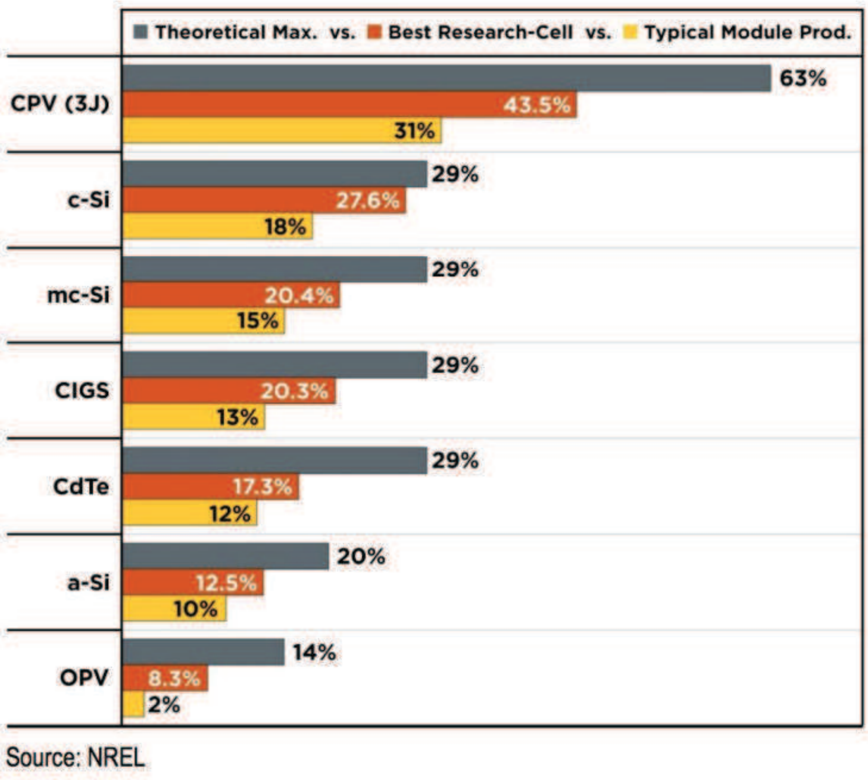

Source: NREL

Figure 2.8: Theoretical and actual solar cells efficiencies by technology [29].

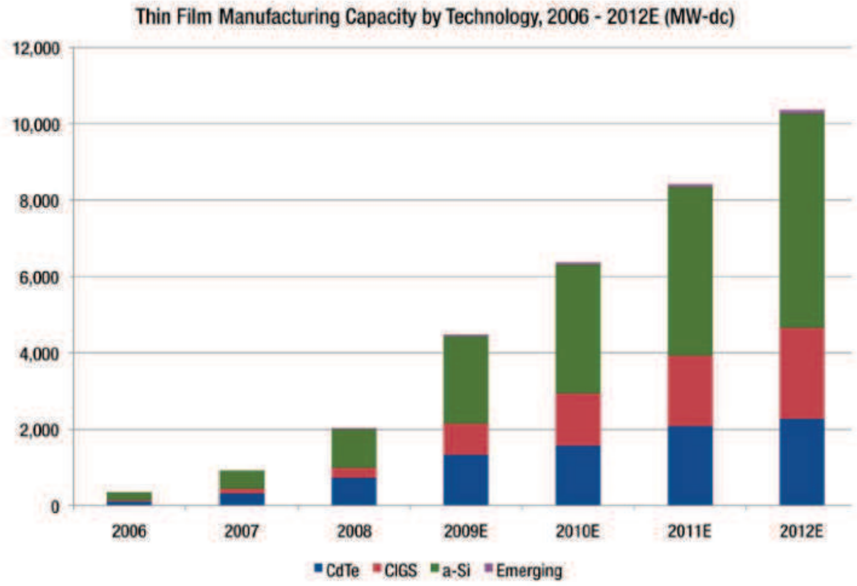

Figure 2.9: Thin-film manufacturing capacity by technology [30].

2.5 Thin-film PV technologies

A thin-film solar cell (TFSC), also called a thin-film photovoltaic cell (TFPV), is a solar cell that is made by depositing one or more thin layers (thin film) of photovoltaic material on a substrate and it is a cheap alternative to monocrystalline and polycrystalline Si-based solar cells. The thickness range of such a layer is wide and varies from a few nanometers to tens of micrometers.It has not yet reached full ripeness, however it has clear advantages that enhance its potential. The possibility to produce devices by depositing layers of a few microns of semiconductor material on several substrates and media, even light and flexible, makes this technology very appealing and it could detain a very broad market in the future.

Thin-film solar cells are usually categorized according to the photovoltaic material used:

- Amorphous silicon (a-Si) and other thin-film silicon (TF-Si);
- Cadmium telluride (CdTe);
- Copper indium gallium selenide (CIS or CIGS);
- Dye-sensitized solar cell (DSC) and other organic solar cells.

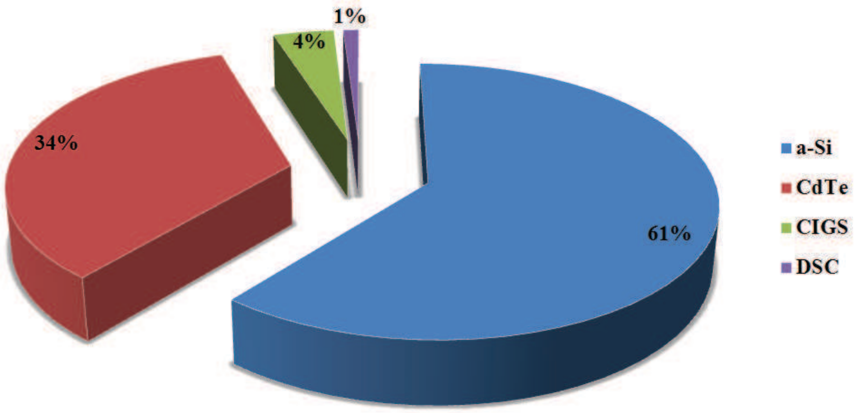

Figure 2.10: The chart shows the market share by thin-film technology (from Greentech media report on thin-film PV) [30].

Some of the advantages of the thin-film technology can be summarized as follows:

- small thickness required to high absorption, small diffusion length and high recombination velocity;
- materials economy, very low weight GHT per unit power;
- various simple and sophisticated deposition techniques;

- variety of structures available: amorphous, polycrystalline, epitaxial;
- topography ranging from very rough to atomically smooth;
- different type of junction possible: homo, hetero, schottky, pec;
- tandem and multi-junction cells possible;
- in-situ cell integration to form modules;
- compatibility with solar thermal devices;
- tailor-ability of various opto-electronic properties (e.g.: energy gap, electron affinity, work function, graded gap, etc.).

In the following sections, a brief review of the most important thin-film PV technologies is presented.

2.5.1 Amorphous silicon (a-Si)

Significant progress has been made in the understanding of properties and of deposition processes for a-Si-based materials and solar cells over the last 35 years. Achievements both in increasing the conversion efficiency of solar cells and in reducing the cost of fabrication have been made. In 1997, a-Si-based solar cells with 15.2% initial efficiency and 13% stable efficiency were demonstrated [31]. The manufacturing volume of a-Si solar modules has increased drastically over the past 20 years, and capacity is presently more than 85 MWp/year. There are now several a-Si PV manufacturers with production capacity of 2 MWp/year or more.

The use of microcrystalline silicon (μc-Si) as the narrow band gap absorber layer in an a-Si-based tandem solar cell has been demonstrated, and cells exceeding 12% conversion efficiency (stabilized) have been produced in different labs. The cells incorporating μc-Si show superior light stability over extended light soaking.

Amorphous Si-based PV technology is unique compared with other Si-based PV technologies. Due to its nature, amorphous Si absorbs sunlight more strongly than c-Si and poly-Si; since c-Si has and indirect band-gap semiconductor, it is subjected to weak absorption while this is not the case of a-Si. A rather thin layer of a-Si is sufficient to absorb sunlight. Amorphous Si can be made at a low temperature on inexpensive substrates. The product is made through a low-cost process. The energy payback time (the time required for an a-Si module to generate the energy used in its production) was estimated as one to two years in 1989, and has probably shrunk substantially since then [32]. Remarkable is the substrates availability. When deposited on selected substrates, the product can be made lightweight and flexible, which is important for many applications. The output power of a-Si PV products also has a positive temperature coefficient: at higher ambient temperature, for example, in areas with more sunshine, the efficiency is higher [8].

a-Si photovoltaics looks more attractive than other types of thin-film PV technologies, such as CdTe and copper-indium-diselenide (CIS)-based PV due to several reasons. Firstly, it has been developed for more than 20 years and the production process is more mature and proven; secondly, the product does not contain any toxic materials such as Cadmium as in CdTe solar cells or a large amount of expensive metal such as indium as in CIS-based solar cells. The materials in amorphous silicon–based cells originate in raw materials that are abundant on earth.

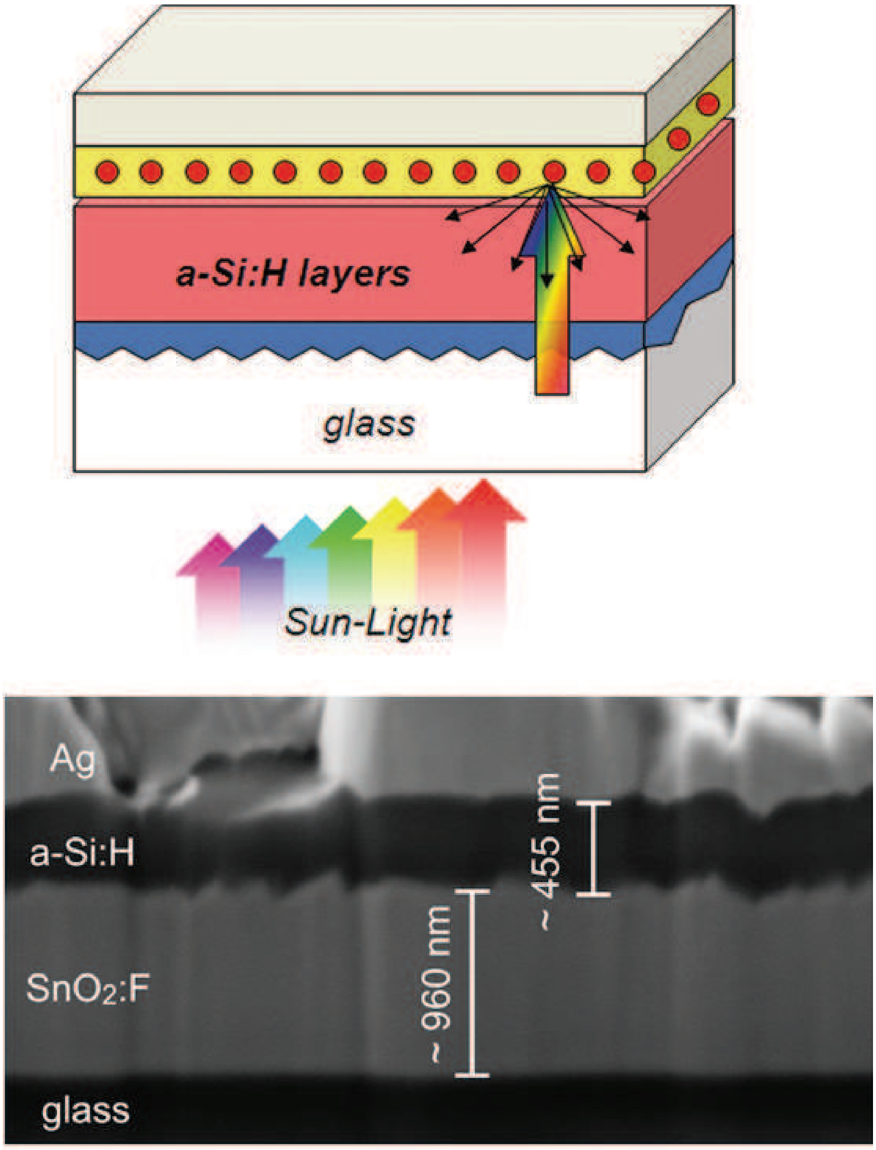

FIGURE 2.11: Cross-section of a a-Si thin film solar cell [33], [34].

The amorphous silicon has a lower efficiency than the c-Si and poly-Si based devices.

The main advantage of a-Si in large scale production is not efficiency, but cost. a-Si cells use approximately 1% of the silicon needed for typical c-Si cells. Moreover, thin-film solar cells can be produce by depositing the silicon from the vapor phase and, reducing even more the cost of the finished product. Actually, these technology has a 2% of PV market share.

2.5.2 Cadmium telluride CdTe

Cadmium telluride (CdTe) emerged as a new electronic material in 1947 when Frerichs synthesized CdTe crystals by the reaction of Cd and Te vapors in a hydrogen atmosphere and measured their photo-conductivity [35]. Cadmium telluride photovoltaics describes a photovoltaics technology that is based on the use of cadmium telluride. A typical CdTe solar cells structure is shown in Fig. 2.12. Cadmium telluride PV is the only thin film photovoltaic technology to surpass crystalline silicon PV in cheapness for a significant portion of the PV market, namely in multi-kilowatt systems [36]. CdTe PV is considered the ecologically leading technology as it provides a solution to key ecological issues including climate change, energy security, and water scarcity. Recently,

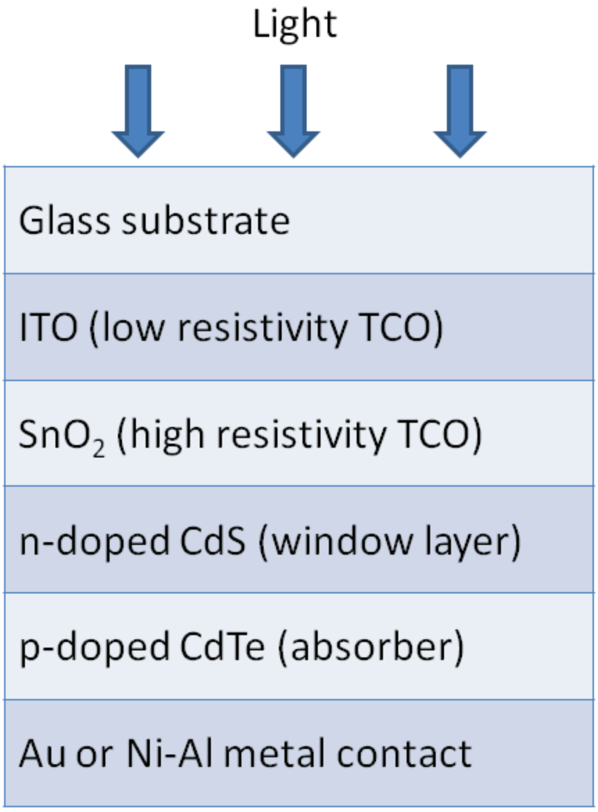

FIGURE 2.12: Cross-section of a CdTe thin film solar cell.

First Solar, Inc. and GE/Primestar have made a series of advances in research cell efficiencies with the most recent record being made in 2013 at 19.6% [37]. In 2013, the record module efficiency was 16.1%. First Solar's record-breaking module efficiency marks a substantial increase from the 14.4% record of the previous year [38]. These achievements demonstrate that CdTe's efficiency potential is far from saturated. By 2017, average production line module efficiency for CdTe PV is projected to be 17% [39]. Since CdTe has the optimal band gap for single-junction devices, it may be expected that efficiencies close to exceeding 20% (such as already shown in CIS alloys) should be achievable in practical CdTe cells.

Questions have been raised over the scalability of CdTe PV and its potential of being constrained by the supply of tellurium. Tellurium production and reserves estimations are subject to a considerable degree of uncertainty and vary considerably. Tellurium (Te) is an element that is primarily used as a machining additive to steel. The existing supply is almost exclusively obtained by recovering Te as a by-product of copper refining. Only a small amount, estimated to be about 800 metric tons per year, is available. According to USGS, global tellurium production in 2007 was 135 metric tons. Most of it comes as a by-product of copper, with smaller byproduct amounts from lead and gold. One gigawatt (GW) of CdTe PV modules would require about 93 metric tons (at current efficiencies and thicknesses), Through improved material efficiency and increased PV recycling systems, the CdTe PV industry has the potential to fully rely on tellurium from recycled end-of-life modules by 2038 [40]. In the last decade, new supplies of tellurium-rich ores have been located, e.g., in Xinju, China as well as in Mexico and Sweden [41]. Since CdTe is now regarded as an important technology in terms of PV's future impact on global energy and environment, the issue of tellurium availability is significant. Recently, researchers have added an unusual twist – astrophysicists identify tellurium as the most abundant element in the universe with an atomic number over 40 [42]. This surpasses, e.g., heavier materials like tin, bismuth, and lead, which are common. Researchers have shown that well-known undersea ridges (which are now being evaluated for their economic recover-ability) are rich in tellurium and by themselves could supply more tellurium than we could ever use for all of our global energy [43]. It is not yet known that this undersea tellurium is recoverable, nor whether there is much more tellurium elsewhere that can be recovered.

2.5.3 Copper indium gallium selenide (CIGS)

Copper indium gallium selenide (CIGS) is a very challenging technology and it is based on the ternary compound semiconductors $CuInSe_2$, $CuGaSe_2$, $CuInS_2$. The first results of single crystal work on $CuInSe_2$ (CIS) were extremely promising but the complexity

TABLE 2.1: CdTe Summary

CdTe Summary
Theoretical Efficiency: 29%
Deposition Techniques: (1)CdTe by Evaporation/sublimation/Chemical Solution/ScreenPrinting (2)CdS by Evaporation/Sublimation/Chemical Solution
Lab Cell Efficiency Achieved: 17.3%
Module Efficiency: 12%
Nature of Junction: Controversial
Formation of Good Junction: Empirical requiring Suitable Heat, Chemical and $CdCl_2$ Treatment required
Estimated Production Cost: about $ 1/Wp for 100 MW plant
Pay back Time: 1.6 months for 10MW plant
Good stability
Issues
Cd Toxicity and Te Availability
Production Technology : Empirical & Temperamental

of the material looked complicated as a thin-film technology. However, after pioneering work in 1976 showed immediate success [44]. It became evident that CIS process technology is very flexible with respect to process conditions. In later developments the addition of Ga and S helped to increase the efficiency giving birth to the CIGS technology.

Copper indium gallium selenide is a direct band-gap semiconductor which is a I-III-VI_2 compound semiconductor material composed of copper, indium, gallium, and selenium. The material is a solid solution of copper indium selenide (CIS) and copper gallium selenide, with a chemical formula of $CuIn_{(x)}Ga_{(1-x)}Se_2$, where the value of x can vary from 1 (pure copper indium selenide) to 0 (pure copper gallium selenide). It is a tetrahedral bonded semiconductor, with the chalcopyrite crystal structure. The band-gap varies continuously with x from about 1.0 eV (for copper indium selenide) to about 1.7 eV (for copper gallium selenide). The CIGS absorber is deposited on a glass or plastic backing, along with electrodes on the front and back to collect current. Because the material has a high absorption coefficient and strongly absorbs sunlight, a much thinner film is required than of other semiconductor materials.

The most common device structure for CIGS solar cells is shown in Fig.2.13. Soda lime glass is commonly used as a substrate, because it contains Na, which has been shown to yield a substantial open-circuit voltage increase, notably through surface and grain boundary defects passivation [46]. However, many companies are also looking at lighter and more flexible substrates such as polyimide or metal foils [47]. A Mo layer is deposited by sputtering which serves as the back contact and to reflect most unabsorbed

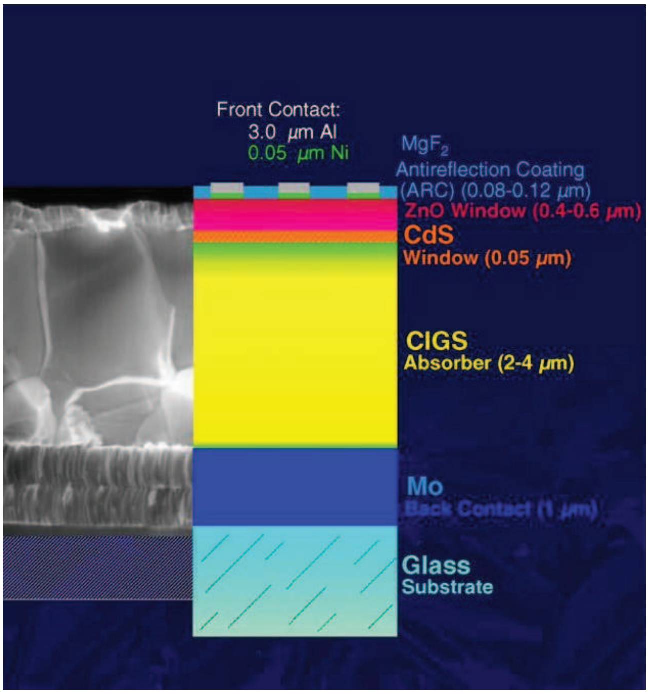

FIGURE 2.13: Cross-section of a CIGS thin film solar cell [45].

light back into the absorber. Following Mo deposition a p-type CIGS absorber layer is grown. CIGS films can be manufactured by several different methods:

1. co-evaporate or co-sputter copper, gallium, and indium onto a substrate at room temperature, then anneal the resulting film with a selenide vapor to form the final CIGS structure. An alternative process is to co-evaporate copper, gallium, indium and selenium onto a heated substrate;
2. A non-vacuum-based alternative process deposits nanoparticles of the precursor materials on the substrate and then sinters them in situ.
3. Electroplating is a low cost alternative to apply the CIGS layer.

A thin n-type buffer layer is added on top of the absorber. The buffer is typically CdS deposited via chemical bath deposition. The buffer is overlaid with a thin, intrinsic ZnO layer (i-ZnO) which is capped by a thicker, Al doped ZnO layer. The i-ZnO layer is used to protect the CdS and the absorber layer from sputtering damage while depositing the ZnO:Al window layer, since the latter is usually deposited by DC sputtering, known as a damaging process [47]. The Al doped ZnO serves as a transparent conducting oxide to collect and move electrons out of the cell while absorbing as little light as possible. The best efficiency obtained on a glass a substrate in 2013 was 20.8% [48]. Still, in

2013, scientists at Empa, the Swiss Federal Laboratories for Materials Science and Technology, developed CIGS cells on flexible polymer foils with a new record efficiency of 20.4% [49] [8].

TABLE 2.2: CIGS Summary

CIGS Summary
Theoretical Efficiency: 29%
Deposition Techniques: (1) Co-evaporation and homogenization (2) Layered vacuum deposition followed by selenization with Se or H2Se (3) Sputter deposition followed by selenization (4) Spray deposition (5) Screen printing followed by selenization (6) Electroplating
Lab Cell Efficiency Achieved: 20.3%
Module Efficiency: 13%
Nature of Junction: Controversial
Formation of Good Junction: Empirical requiring Suitable Heat, Chemical and $CdCl_2$ Treatment required
Pay back Time: about 4 months for 100MW plant
Good stability
Issues
Multiple Binary Phases; Polymorphism;Structural and Electronic Disorder
Availability of In and Ga
Sensitive Structure
Sophisticated Controls required
Upscaling Problematic

2.5.4 Organic solar cells (OPV)

The discovery of electro-luminescence properties in 1976 by the nobel prize awarded Mac-Diarmid, created a new electronic research field, which puts together different field, such as chemistry, physics, and electronics. This is called Organic Electronics. Organic LED (OLED), organic thin-film transistor (OTFT), and organic solar cells (OPV) have been intensively studied recently and most of these devices already detain a remarkable market in the electronic devices field. In fact, considering the fact that OLEDs have been already realized and place on the electronic devices market, there is a realistic chance to achieve efficient photovoltaic conversion also in such materials because this is just the reverse process.

Due to the knowledge on organic chemistry, the organic compounds available to produce semiconductor is nearly infinite. Beside this, the large interest in these materials results from remarkable advantages: materials availability, large-scale manufacturing, low-temperature and low cost fabrication processes. The up-scaling of organic solar cells into large-area devices, always a big challenge with inorganic solar cells, has already been demonstrated to be straightforward.

Organic semiconductors display high absorption coefficients which allows to produce very thin solar cells (much more below than 1mm) and in turn, a small amount of materials is required. Moreover, organic solar cells can be reproduced on flexible substrates, which allows the integration of solar cells on textiles. Finally, since the fabrication process of those devices is very cheap, the energetic pay-back time of organic solar cells is expected to be very short [8].

Several issues are still open about organic electronics and then on OPV, about efficiency only modest solar conversion efficiencies up to 1% were reached until 1999. Nevertheless, the very appealing advantages cause a largely growing interest in the development of such solar cells. In fact, OPV efficiencies are increasing rapidly (about 8% in 2012 [24].

The next chapter covers separately the thin-film technology studied in this work, that is the dye-sensitized solar cells.

Chapter 3

Dye-Sensitized Solar Cells

3.1 Introduction

So far, photo-electrochemical cells (PSC) are an alternative to the all solid state solar cells and the most successful PSC are the dye sensitized solar cells (DSC) developed by Grätzel and co-workers in 1991, which are now commonly referred to as *Grätzel cells* [2].

To improve light-harvesting efficiencies and cell performance, researchers used two approaches: developing photo-electrodes with larger surface areas that could adsorb large amount of dye and synthesizing dyes with broader absorption ranges. Significant improvements in the performance of a dye-sensitized solar cell have been mainly due to the development of high-performance nanoporous TiO_2 thin-film electrodes that have a large surface area capable of adsorbing a large amount of photo-sensitizer, and due to the synthesis of new Ru complex photo-sensitizers capable of absorbing in the wide visible and near-IR region from 400 to 800 or 900 nm.

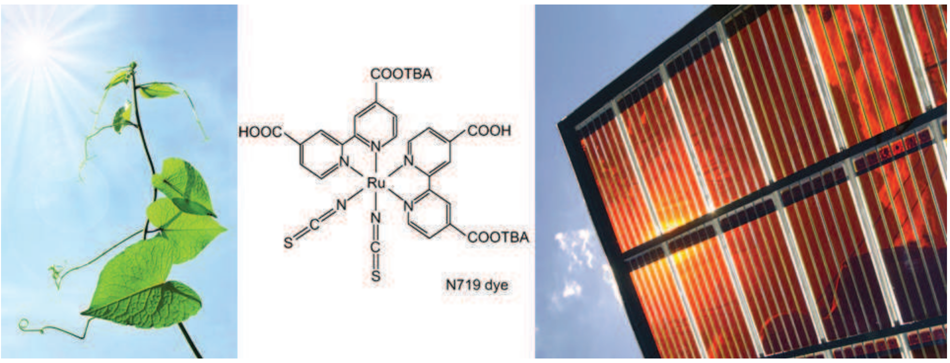

Figure 3.1: The invention of dye-sensitized solar cells has been inspired by nature and in particular by the photosynthesis phenomenon.

Ru complexes, and in particular in its bipyridyl complex, are suitable photo-sensitizers because the excited states of the complexes have long lifetimes and oxidized Ru(III) has long-term chemical stability. Therefore, Ru bipyridyl complexes have been studied intensively as photo-sensitizers for homogeneous photo-catalytic reactions and dye-sensitization systems. An Ru bipyridyl complex, bis(2,2'-bipyridine)(2,2'-bipyridine-4,4'-dicarboxylate)ruthenium(II), having carboxyl groups as anchors to adsorb onto the semiconductor surface, was synthesized and single-crystal TiO_2 photo-electrodes sensitized by the Ru complex were studied in 1979 to 1980 [50, 51].
Remarkable improvements in the performance of DSC have been made by Grätzel and coworkers at the Swiss Federal Institute of Technology (EPFL). They achieved a solar energy efficiency, η, of 7 to 10% under AM1.5 irradiation using a DSC consisting of a nanocrystalline TiO_2 thin-film electrode having a nanoporous structure with large surface area, a novel Ru bipyridyl complex, and an iodine red-ox electrolyte [2, 4]. They also developed a Ru terpyridine complex that absorbs in the near-IR region up to 900 nm as a photo-sensitizer for a nanocrystalline TiO_2 photo-electrode: the resulting cell obtained $\eta = 10.4\%$ under AM1.5 with a short-circuit photo-current density (J_{SC}) of 20.5 mA/cm^2, an open-circuit voltage (V_{OC}), of 0.72 V, and a fill factor (FF) of 0.70 [52, 53]. Recently, they have developed a new DSC with an overall efficiency of $\eta = 15\%$ [6].
The DSC is an attractive and promising device for solar cell applications that have been intensively investigated worldwide, and its PV mechanism is well understood [54]. Recently, commercial applications of the DSC have been under intensive investigation. The cost of commercially fabricating DSC is expected to be relatively low because the cells are made of low-cost materials and assembly is simple and easy [8].

In the following section, the DSC technology is described, including its structure, used materials, working principle, advantages and disadvantages, and applications.

3.2 DSC: structure and working principle

The general structure of a DSC is shown Fig. 3.2 and consists of:

- a transparent conductive oxide (TCO) usually indium-tin oxide (ITO) fluorine doped (FTO);
- a transparent semiconductor oxide, very often titanium dioxide (TiO_2) is used which acts as photo-anode and it is also called working electrode (WE);
- a mono-layer of dye-sensitizer. Typically, a ruthenium based dye is used due to its great properties;

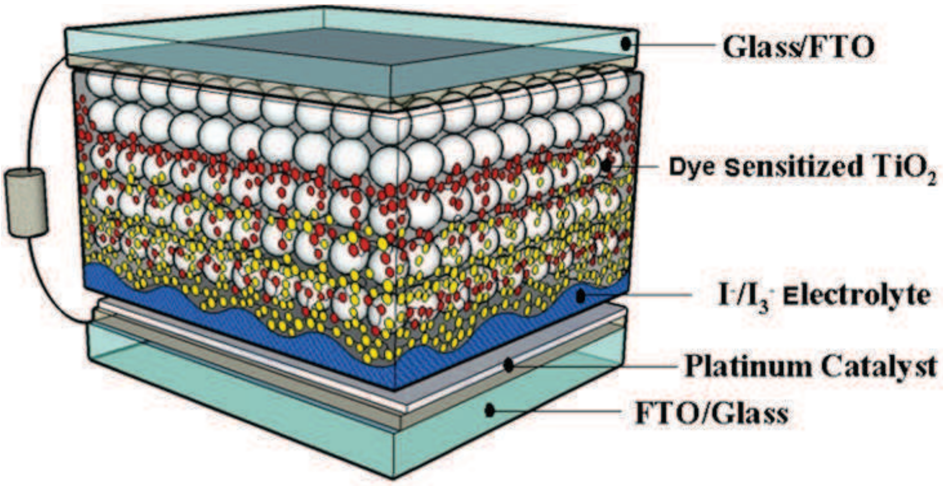

FIGURE 3.2: The picture shows a the structures of a typical DSC.

- an electrolyte solution, typically tri-iodide/iodide (I_3^-/I^-) based electrolyte;
- another TCO, which is again indium-tin oxide (ITO) fluorine doped (FTO). This acts as photo-cathode and it is covered with a thin layer of platinum (Pt) which acts as catalyst.

The dye molecules are quite small (nanometer sized), so in order to capture a reasonable amount of the incoming light the layer of dye molecules needs to be made fairly thick, much thicker than the molecules themselves. To address this problem, a nanomaterial is used as a scaffold to hold large numbers of the dye molecules in a 3-D matrix, increasing the number of molecules for any given surface area of cell. In existing designs, this scaffolding is provided by the semiconductor material, which serves double-duty.
As anticipated above, the photovoltaic mechanism of DSC is different from that of conventional Si-based solar cells. In order to better understand the working mechanism of DSC, it is mandatory to go over details of the red-ox mediator I_3^-/I^-.

3.2.1 Red-ox mediator: basic concepts

The most used red-ox mediator in the electrolyte preparation is the couple tri-iodide/iodide (I_3^-/I^-). In solution, iodine (I) will bind with iodide (I^-) to form tri-iodide (I_3^-) in an equilibrium reaction with an equilibrium constant for formation, K_1:

$$I_2 + I^- \Leftrightarrow I_3^-, K_1 \tag{3.1}$$

If the iodine concentration is high, poly-iodide species like I_5^-, I_7^-, and I_9^- may also be formed, but in practice, only tri-iodide seems to be of importance in DSC electrolytes. Because K_1 is high (in the organic solvents typically used for electrolytes in DSC) and the iodide concentration is high, the concentration of free iodine will be very low[1]. The red-ox potential of the electrolyte ($E_{\text{red-ox}}$) is given by the Nernst equation Eq. 3.3, which reads for the tri-iodide/iodide couple:

$$I_3^- + 2e^- \Leftrightarrow 3I^- \tag{3.2}$$

$$E_{red-ox} = E^0 + \frac{RT}{2F} \ln \frac{[I_3^-]}{[I^-]^3} \tag{3.3}$$

where E^0 is the formal potential, R the gas constant, T the absolute temperature, and F the Faraday constant. A number of one-electron red-ox reactions can occur in the tri-iodide-iodine system. These reactions involve the unstable radicals atomic iodine ($I^\bullet$) and diiodide ($I_2^{-\bullet}$). Their red-ox potentials are related through a series of equilibria and equilibrium constants:

$$2I^\bullet = I_2, K_2 \tag{3.4}$$

$$I^\bullet + I^- = I_2^{-\bullet}, K_3 \tag{3.5}$$

About seven red-ox reactions could take place in the iodide-iodine system and some of them are important for the DSC. Red-ox potentials of the iodide/tri-iodide system are summarized in Tab. 3.1. In the dye-sensitized solar cell, the two-electron reaction 3.2 sets the counter electrode at the red-ox potential of the electrolyte. Reaction 3.2 is, however, not directly responsible for the regeneration of the oxidized dye, as will be discussed in the section on dye regeneration below. Instead, the one-electron reaction 3.6, seems to be responsible for reduction of the oxidized dye.

$$2I^- \rightarrow I_2^{-\bullet} + e^- \tag{3.6}$$

An energy scheme of the DSC is shown in Fig. 3.3. For the standard sensitizer cis-$Ru(dcbpy)_2(NCS)_2$, also known as N3 or N719, $E^0(D^+/D)$ is 1.10 V vs NHE if the dye is fully protonated [53]. Electrochemistry of $Ru(dcbpy)_2(NCS)_2$ adsorbed onto a conducting tin oxide glass gave the same value, for both N3 and N719. The potential difference between $E^0(D^+/D)$ and $E^0(I_3^-/I^-)$ amounts to 0.75 V. This potential is used to drive the forward reactions in the DSC. Based on the reaction scheme for dye regeneration, which

TABLE 3.1: Red-ox potential of red-ox mediator by solvent

solvent	E^0 (I_3^-/I^-)	E^0 ($I^\bullet/I^-$)	E^0 ($I_2^{-\bullet}/I^-$)	E^0 ($I_3^-/I_2^{-\bullet}$)
water	+0.536	+1.33	+1.03	+0.04
acetonitrile	+0.29	+1.23	<0.93	>-0.35

---

[1] For example, in a red-ox electrolyte prepared from 0.5 M LiI and 0.05 M I_2 in acetonitrile ($\log(K_1/M^{-1})$) 6.76), a free iodine concentration of 2 x 10^{-8} M is calculated.

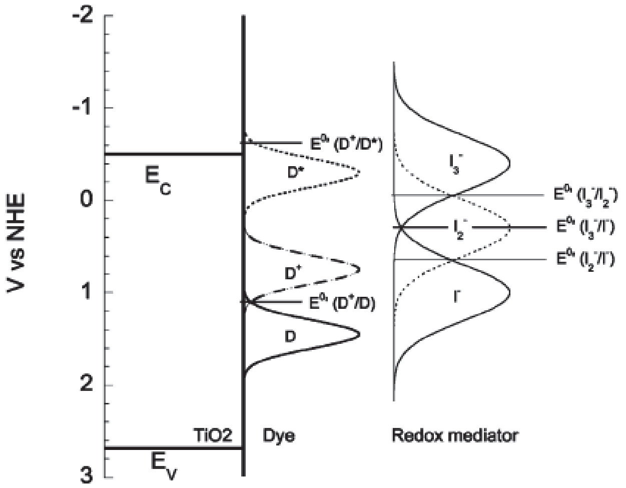

FIGURE 3.3: Energy scheme of the cis-Ru(dcbpy)$_2$(NCS)$_2$-sensitized TiO$_2$ solar cell with I_3^-/I^-- red-ox mediator.

will be discussed in the next section, the driving force for dye regeneration reaction is given by the difference between $E^0(I_2^-/I^-)$ and $E^0(D^+/D)$. The unstable $I_2^{-\bullet}$ radical, which is formed during dye regeneration, is converted into I_3^-. This corresponds to a potential loss of several hundred millivolts $[E^0(I_2^-/I^-) - E^0(I_3^-/I^-])$ in the DSC [55].

3.2.2 DSC: working principle

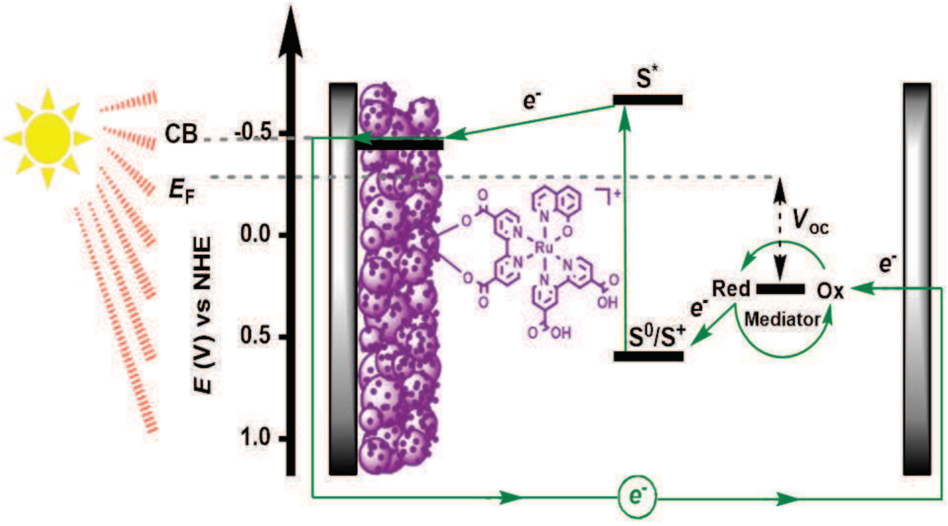

FIGURE 3.4: A representation of the DSC working principle.

The working principle of the solar cells is shown in Fig. 3.4. When the dye molecule is hit by sunlight it becomes photo-excited and instantly injects an electron into the conduction band of the semiconductor oxide. The time scale of this process is tens of femtosecond to hundreds of picoseconds and depends on the electronic coupling and energetic overlap between donor and acceptor states. Its original state is then restored by the donation of an electron from the electrolyte, containing the red-ox system I_3^-/I^-previously mentioned. The regeneration of the dye by iodide intercepts the recapture of the electron of the conduction band by the oxidized dye.

The half-time for regeneration of the most common sensitizer, cis-Ru(dcbpy)$_2$(NCS)$_2$, in the presence of about 0.5 M iodide is in the range of 100 ns to 10 μ, depending on the precise composition of the electrolyte [56]. The nature of the cation in the electrolyte plays a significant role: faster dye regeneration when using electrolytes containing cations that adsorb at the TiO_2surface [57]. This was attributed to a higher local concentration of the iodide anion near the TiO_2/electrolyte interface. The reaction between oxidized dye and iodide leads to the formation of diiodide radicals ($I_2^{-\bullet}$) [58].

$$D + h\eta \rightarrow D^* \tag{3.7}$$

$$D^* \rightarrow D^+ + e^-(TiO_2) \tag{3.8}$$

$$D^+ + I^- \rightarrow (D \cdots I) \tag{3.9}$$

$$(D \cdots I) + I^- \rightarrow D + I_2^{-\bullet} \tag{3.10}$$

$$2I_2^{-\bullet} \rightarrow I_3^- + I^-, \tag{3.11}$$

The full working mechanism inside a DSC, is described by reaction 3.7-3.11. The process for the reduction of the oxidized dye (D^+) by iodide is given by reactions 3.8-3.11. After electron injection from the excited dye (D^*), the oxidized dye D^+ is reduced by iodide, under the formation of a complex ($D \cdots I$). The formation of such a complex is confirmed by [**?**]. The complex dissociates when a second iodide ion comes in and dye in the ground state D and $I_2^{-\bullet}$ are formed, reaction 3.10. Two diiodide radicals react to form triiodide and iodide from disproportionation[2], reaction 3.11. The concentration of $I_2^{-\bullet}$in a DSC under operation can be estimated as follows: if we assume that the solar cell generates a photo-current of 10 mA/cm^2, the formation rate of $I_2^{-\bullet}$is 10 x 10^{-3}/F) 1.0 x 10^{-7} mol/(cm^2 s). The generation is confined to the pores in the TiO_2film. Assuming a 10 μm film with 50% porosity, the pore volume is 5 x 10^{-4} cm^{-3}, and the $I_2^{-\bullet}$generation rate per volume is 0.2 mol L^{-1} s^{-1}. With the second-order rate constant for reaction 3.11 in acetonitrile of 2.3 x 10^{10} M^{-1} s^{-1} [59], the steady state concentration of $I_2^{-\bullet}$is calculated to be 3 μM. This is 2 orders of magnitude higher than the concentration of free I_2in a typical acetonitrile-based red-ox electrolyte.

Under certain conditions, an alternative pathway is possible in dye-sensitized solar cells

---

[2] Dispropornation is a specific type of red-ox reaction in which a species is simultaneously reduced and oxidized to form two different products.

involving the reductive quenching of excited dye molecules by iodide:

$$D^* + I^- \rightarrow D^- + I^\bullet \tag{3.12}$$

$$I^\bullet + I^- \rightarrow I_2^{-\bullet} \tag{3.13}$$

$$D^- \rightarrow D + e^-(TiO_2) \tag{3.14}$$

$$D^- + I_3^- \rightarrow D + I_2^{-\bullet} + I^-, \tag{3.15}$$

This pathway can be significant if electron injection for the excited dye into the conduction band of the semiconductor is relatively slow or in the presence of very high concentrations of iodide. The excited dye is reduced by iodide, leading to the formation of the reduced dye D^- and $I_2^{-\bullet}$, see 3.12 and 3.13. Initially, iodine radicals may be formed, reaction 3.12. The reduced dye can either inject an electron into the conduction band of TiO_2, reaction 3.14, leading to photo-current or react with triiodide, reaction 3.15, which is a recombination reaction [60]. In practical dye-sensitized solar cell devices, the reductive quenching pathway may play a role in ionic liquid electrolytes, where iodide concentration can be very high (>5 M). Recent discoveries reported that optimum solar cell performance was obtained in a binary ionic liquid electrolyte containing 50% 1-phenyl 3-methyl imidazolium iodide, while higher concentrations led to a decrease in photo-current, suggesting that reaction 3.15 is dominant over reaction 3.14 after reductive quenching (the Ru complex Z907 was used as a sensitizer) [61].

When the DSC is illuminated under open circuit conditions, the net rate of electron injection from dyes into the $TiO_2$is balanced by the net rate of electron transfer from the electrode to the electrolyte. Because the V_{OC} depends on the electron concentration in the TiO_2, changes in V_{OC} can be related to the recombination process. The following expression has been derived for the steady-state V_{OC} in the DSC:

$$V_{OC} = \frac{kT}{e} \ln \left(\frac{J_{inj}}{k_{rec} n_{c,0} \left[I_3^- \right]} \right) \tag{3.16}$$

where J_{inj} is the flux of injected electrons, k_{rec} is the rate constant for triiodide reduction, and $n_{c,0}$ the conduction band electron density in the dark. Eq.3.16 predicts that V_{OC} will increase by 59 mV for a 10-fold increase in light intensity, because J_{inj} is proportional to light intensity. Values close to 60 mV are indeed frequently found [62], but higher values have also been reported.

At the counter electrode, iodide is regenerated, by the reduction of tri-iodide opposite electrode and the circuit is completed through electronic migration through the external load, see reaction 3.2.

The potential difference generated during the illumination corresponds to the difference between the Fermi level of the electron in the semiconductor electrode and the red-ox potential of the electrolyte, see Eq. 3.17.

$$V_{OC} = E_F^{TiO_2} - \Phi_{red-ox}, \tag{3.17}$$

Overall, all the electric power is generated without any permanent chemical changes within the device. Must be notice, that in parallel with these processes, the electrons in the conduction band of the semiconductor, can be recombined with the oxidized dye or with electron-acceptor species in the electrolyte solution. Dye-sensitized solar cells separate the two functions provided by silicon in a traditional cell design. Normally the silicon acts as both the source of photo-electrons, as well as providing the electric field to separate the charges and create a current. In the dye-sensitized solar cell, the bulk of the semiconductor is used solely for charge transport, the photo-electrons are provided from a separate photosensitive dye. Charge separation occurs at the surfaces between the dye, semiconductor and electrolyte.

When it comes to solid-state dye-sensitized solar cells, the electrolyte solution is replaced by a p-type organic semiconductor with a wide band gap. Under these conditions, when the dye is excited, injects electrons in the oxide-type n, being regenerated by the injection of holes from the semiconductor complementary, organic or organic, p-type. This type of variant has however a AM 1.5 solar conversion significantly more abundant low 10% of the previous [55].

3.3 Materials

The present section goes over details of the materials that are used in DSC.

3.3.1 Nanoporous semiconductor

The semiconductor constitutes the substrate on which the dye is deposited, however this is not the only function. In fact, it has to collect and transport the electrons that are injected on its conduction band. Moreover it must provide a fairly good transparency to allow light to go through and hit the photo-active material. The main characteristics of the transparent semiconductor must have are:

- it must be transparent to most of the visible sun spectrum;
- its conduction band must be properly aligned with the excited energy level of the dye to allow a easy electron injection;

- be thermally stable and resist to corrosion;
- have a low cost and widely available.

The semiconductor layer has also not be too thick in order to not introduce a high series resistance. A key feature of the semiconductor layer is the porosity. The semiconductor should have a nanostructured porous structure, with a porosity that gradually increases moving toward the inside of the cell. Specials deposition techniques allows to deposit a high porosity semiconductor which in turn offer a large area on which the dye molecules can be adsorbed, increasing the overall efficiency of the cell.

Photo-anodes made of materials such as Si, GaAs, InP, and CdS experience decomposition under irradiation in solution due to photo-corrosion. In contrast, oxide semiconductor materials have good chemical stability under visible irradiation in solution and in addition, they are nontoxic, cheap, and widely available. The most used oxide semiconductor for DSC is TiO_2. The chemical structure of rutile TiO_2 is shown in Fig. 3.5.

Usually, the TiO_2 thin-film photo-anode is prepared by a very simple process. TiO_2 colloidal solution (or paste) is coated on a TCO substrate and then sintered, producing a TiO_2 film about 10μm in thickness. Typical sintering temperature range from 450°C to 500°C. Because this film is composed of TiO_2 nanoparticles (10–30 nm), giving it a nanoporous structure, the actual surface area of TiO_2 compared to its apparent surface area, roughness factor (RF), is >1000; that is, a 1 cm^2 TiO_2 film (10μ m thickness) has an actual surface area of 1000 cm^2. The dye is considered to be adsorbed on the TiO_2 surface in a mono-layer. Thus, if the nanoporous TiO_2 film has a high RF, the amount of dye adsorbed is extremely increased (on the order of 10^{-7} mol/cm^2), resulting in an increase of the light-harvesting efficiency (LHE) that is near 100% at the peak absorption wavelength of the dye. In comparison, the amount of adsorbed dyes on the surface of single-crystal and poly-crystal materials is quite small, with only 1% LHE even at the peak wavelength.

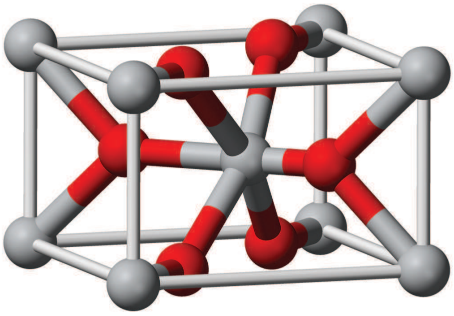

FIGURE 3.5: Rutile titanium dioxide molecule structure.

Normally, the TiO_2 film contains also large TiO_2 (see Fig. 3.6, picture on the left

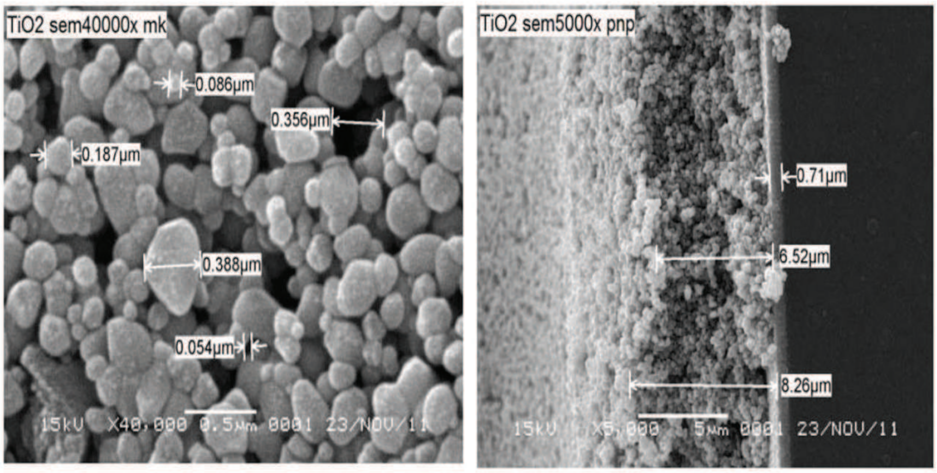

Figure 3.6: AFM picture of titanium dioxide. Left, titanium dioxide nanoparticles. Right, multi-layer titanium dioxide with different size of the nanoparticles in order to improve LHE.

side) particles (250–300 nm), which can scatter incident photons significantly, to have a high LHE. Besides having a large area on which deposit the photo-active material, the porosity of the film is also important to allow the electrolyte, which contains the red-ox ions, to penetrate the film effectively to suppress the rate-determining step via diffusion of red-ox ions into the film. Appropriate porosity, 50% to 70%, is controlled in the sintering process by the addition of a polymer such as polyethylene glycol (PEG) and ethyl cellulose (EC) into the TiO_2 colloidal solution or paste.

Fig. 3.7 shows a scanning electron microscope (SEM) photograph of a typical nanocrystalline TiO_2 film deposited by doctor blading technique, which one of the most used technique to deposit TiO_2.

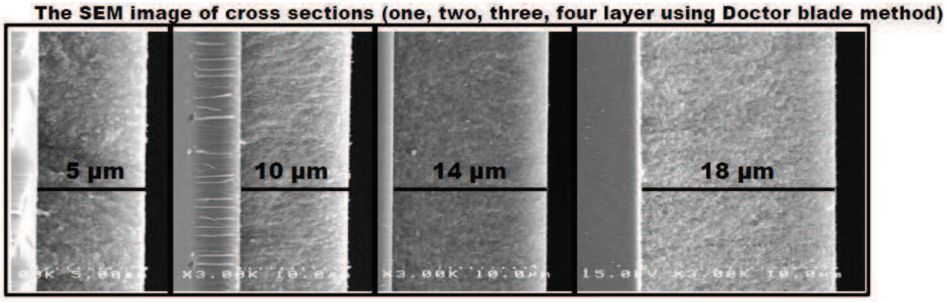

Figure 3.7: AFM picture of titanium dioxide.

3.3.2 Dyes

The dye is the photo-active material of a DSC and allows to intercept the solar radiation and convert it into a stream of electrons. Its characteristics are critical because they determine the absorption spectrum and the and the efficiency of the cell. The characteristics that a good dye must possess are:

- ensure the absorption of all light below the threshold of 920nm;
- be firmly anchored to the surface the transparent semiconductor;
- the energy level of its excited state should be properly aligned with the conduction band of the semiconductor, in order to promote the injection of electrons on the conduction band of the semiconductor which in turn improves the overall efficiency of the cell;
- it should possess a red-ox potential high enough in order to be reduce as soon as possible by the ions present in the electrolyte;
- must demonstrate good stability over time, such as to ensure at least 10^8 red-ox cycles.

The first dyes used were natural and were based on anthocyanin and its derivatives, a substance present in many fruits. Anthocyanins are among the most important groups of pigments present in the plants, and are responsible for the colors red, blue and violet, which are found in flowers and fruits. They belong to flavonoids and consist of a molecule of benzene fused with a pyran connected with a phenyl group which may in turn be due to different substituents. Varying these secondary groups it is possible to obtain a wide range of compounds with different optical properties. The largest concentrations of anthocyanins can be found in: eggplant, red grapes, cherries, blackberries and blueberries. Even if they allow to obtain good cell efficiencies, the key role of the dye in the cell prompted researchers to find new dyes capable of absorbing a more amount of solar radiation. The most used dyes so far are ruthenium-based sensitizers due to their great thermal stability and good optical properties. The chemical structure of typical Ru complexes photo-sensitizers are shown in Fig. 3.8. The cis-bis(4,4'-dicarboxy-2,2'-bipyridine)dithiocyanato ruthenium(II) ($RuL_2(NCS)_2$ complex), which is referred to as N3 dye (or red dye), can absorb over a wide range of the visible regions from 400 to 800nm. The trithiocyanato 4,4'4"-tricarboxy-2,2':6',2"-terpyridine ruthenium(II) (black dye) ($RuL'(NCS)_3$ complex), absorbs in the near-IR region up to 900nm. Fig. 3.9 shows absorption and transmission spectra of N3 and black dyes in solution. Absorption by these dyes in the visible and near-IR regions is attributed to the metal-to-ligand charge-transfer (MLCT) transition. The highest occupied molecular orbital (HOMO) and the lowest unoccupied molecular orbital (LUMO) originate from the d-orbitals of the Ru metal and the π^* orbital of the ligand, respectively. The NCS ligand shifts the HOMO level negatively, leading to a red shift in the absorption spectrum of the complex, and

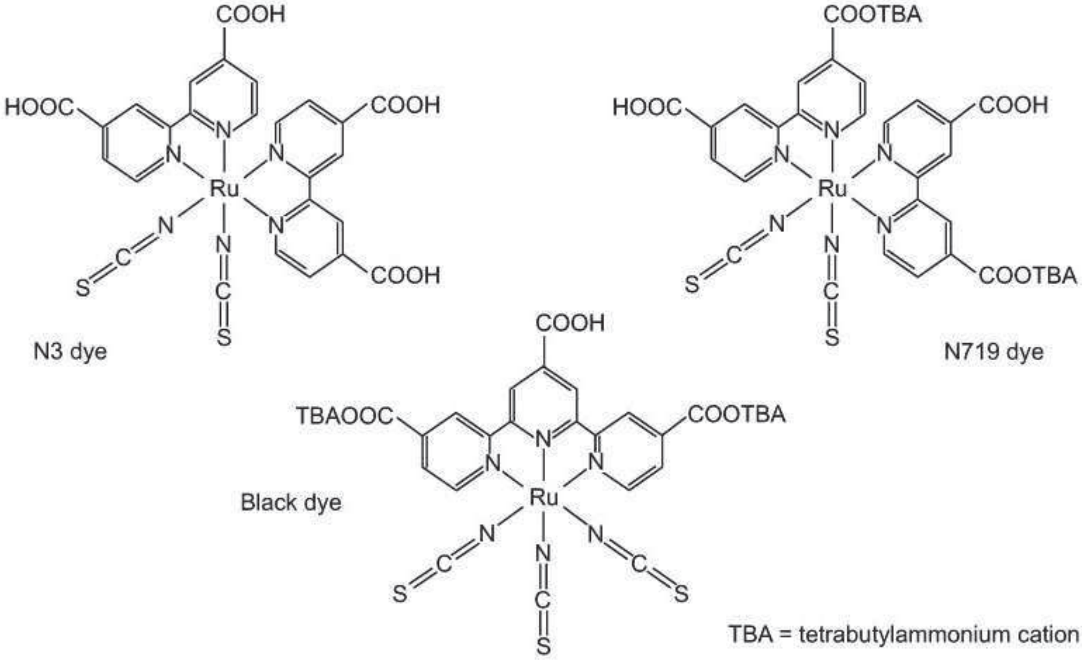

FIGURE 3.8: Chemical representation of ruthenium based-dyes. They are the most used and the most efficient dyes known so far.

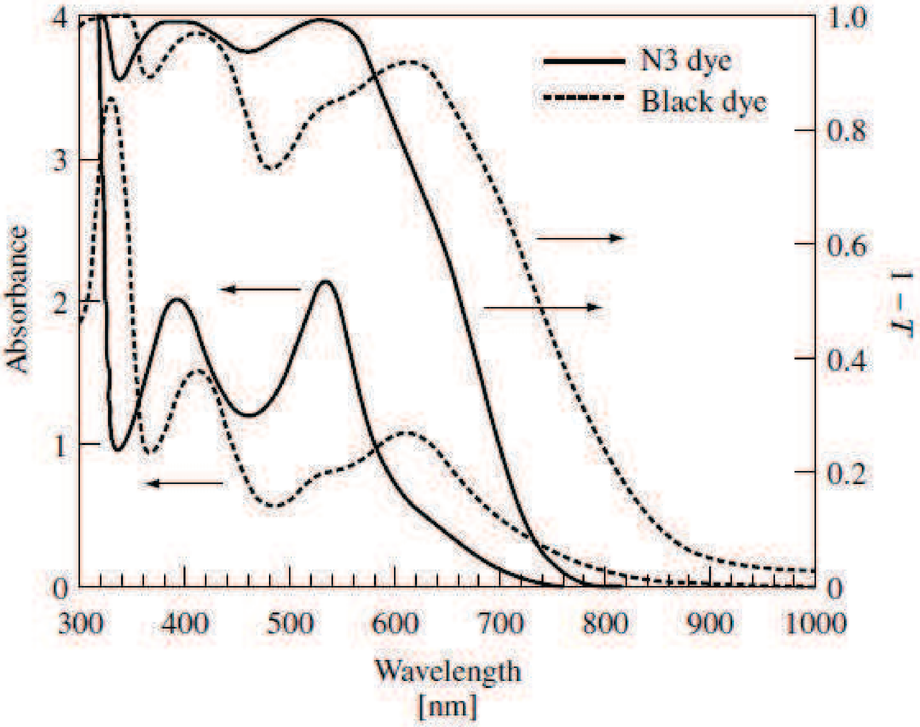

FIGURE 3.9: Absorption and transmission spectra of N3 and 'black' dyes. The y-axis is represented by absorbance (A) and 1 - T (1 - 10^{-A}), where t is the transmittance.

also contributes electron acceptance from reduced red-ox ions (I^-). The Ru complex is adsorbed on the TiO_2 surface due to relatively strong bonds. These Ru complexes have either carboxylate bidentate coordination groups and ester bonding -(-C(=O)O-) to anchor to the TiO_2 surface. Anchoring which causes a large electronic interaction between the ligand and the conduction band of TiO_2, resulting in effective electron injection from the Ru complex into the TiO_2.

Fig. 3.10 shows the anchoring structure of the N3 dye adsorbed on the (101) surface of TiO$_2$. The coverage of the TiO_2 surface with the N3 dye reaches near 100% as derived from the surface area of TiO_2 and the amount of the dye.

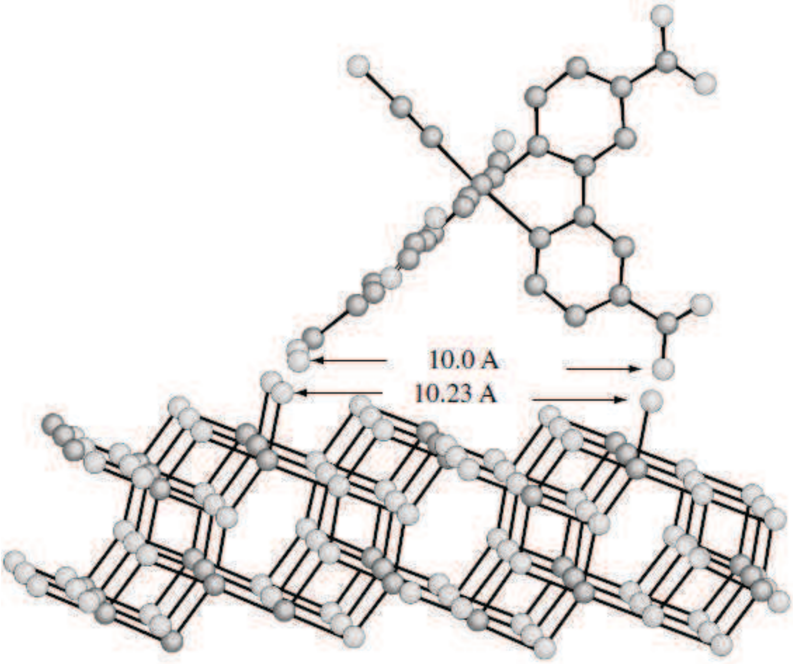

FIGURE 3.10: Representation of N3 dye adsorbed onto the titanium dioxide surface [8].

In order to improve the overall cell efficiency, a "‘multi-junction"’ structure can be used. As for the solid state solar cells, it has been proven that a multi-dye solar cell can be realized. As discussed above, dyes can be tuned in order to absorb a different portion of the solar spectrum and in turn to make the solar cell of the desired color. See for instance, Figs. 3.11 and 3.12. As for the solid state solar cells and concerning for instance a double-dye DSC, the dye with the higher energy gap is anchored to the titanium dioxide and the other dye is anchored to the first. In this way, the dye facing the exposed surface will absorb high photon energy (violet-blue) and let low energy photon (green and red) to go through itself and hit the second dye. In Fig. 3.13 is shown the process to realize multi-dye DSC.

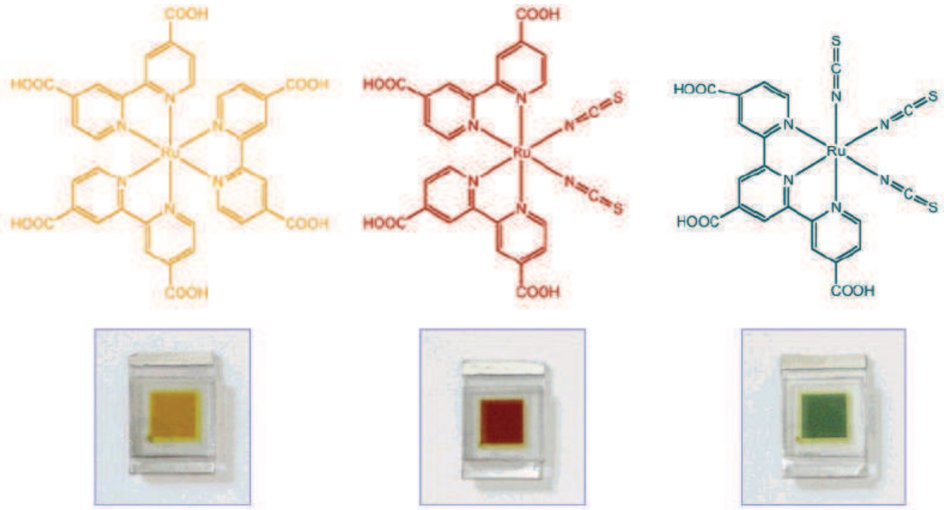

FIGURE 3.11: Examples of different ruthenium-based dyes tuned to absorb different portion of the solar spectrum and then with different colors.

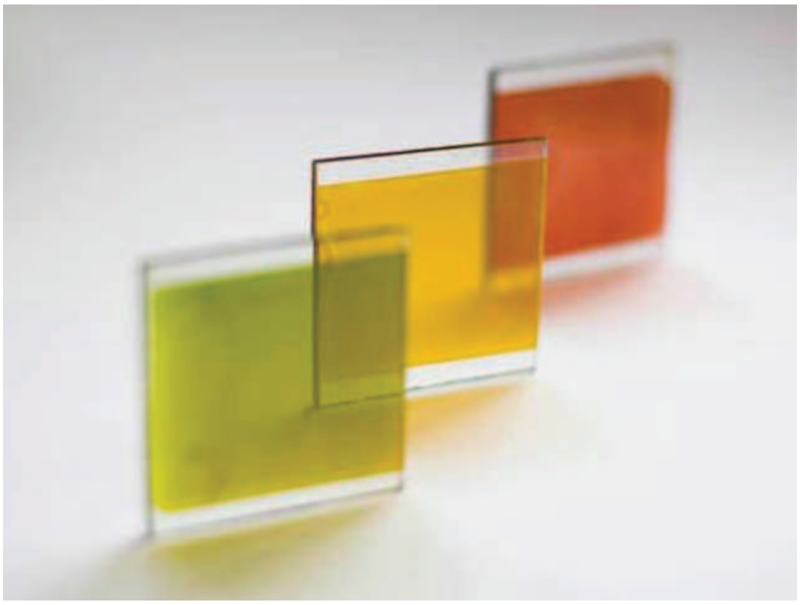

FIGURE 3.12: Examples of DSC substrates with different dye and then different colors.

3.3.3 Electrolytes

The electrolyte is another key component to design and obtain high efficiency DSC. Its task is to close the circuit between the anode and cathode inside the cell, returning electrons to the oxidized dye and, on the other side, collecting electrons from the external circuit. Usually the electrolyte contains a re-dox couple derived from the dissolution of a salt in a aqueous solution. The modification of its chemicals composition or electrolyte leakage will inevitably affect the efficiency of the cell.
The charge transport in the electrolyte is mainly by diffusion, which is slower than the charge transport in the titanium dioxide. Due to this reason, the distance that a carrier

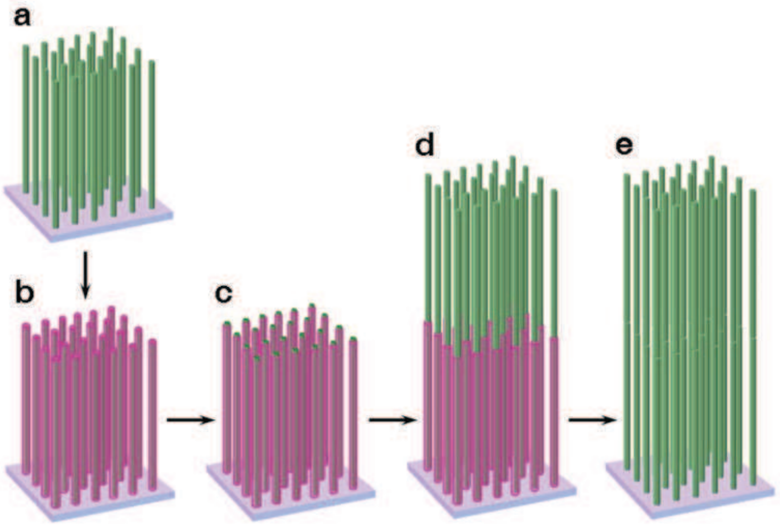

FIGURE 3.13: A schematic representation of a multilayers dye-based solar cells.

travels in the electrolyte must be minimized and this can be done by minimizing the amount of electrolyte. If the ions diffusion is too slow, a low concentration of reducing ions is expected near the dye molecules, promoting secondary reactions between the oxidized dye molecules and chemical compound present in the electrolyte.

Br^-/Br_2, bipyridyl cobalt(III/II), triiodide-iodide (I_3^-/I^-), $SCN_-/(SCN)_2$, $SeCN_-/(SeCN)_2$, and hydroquinone have also been used as red-ox electrolyte for DSC [63, 64], but so far, the most used red-ox couple for the fabrication of DSC is the I_3^-/I^-, which, among all the re-dox couples options, allows to obtain the highest DSC efficiency.

As described above, I_3^-/I^-red-ox ions mediate electrons between the TiO_2 photo-anode and the counter electrode. Mixtures of iodides such as LiI, NaI, KI, etraalkylammonium iodide (R_4NI), and imidazolium-derivative iodides with concentrations of 0.1 to 0.5 M (M: molar concentration) and 0.05 to 0.1 M I_2 dissolved in nonprotonic solvents (e.g. acetonitrile, propionitrile, methoxyacetonitrile, propylene carbonate, and their mixture) are employed.

Cell performance of DSC depends on counter cations of iodides such as Li_+, Na_+, K_+, and R_4N_+ owing to different ion conductivity in the electrolyte or adsorption on the TiO_2 surface, leading to a shift of the conduction-band level of the TiO_2 electrode [63, 65].

As anticipated above, the viscosity of solvents directly affects ion conductivity in the electrolyte, and consequently the cell performance: in fact, the more viscose is an electrolyte, the higher will be the the time required to an ion to diffuse from the dye to the counter-electrode and vice versa. Therefore, to improve cell performance, high-viscosity solvents should be avoided. For example, the diffusion coefficient of I_3- in methoxyacetonitrile is estimated as 5.4-6.2 x 10^{-6} cm^2/s [63]. Basic compounds such as tert-butylpyridine are added to the electrolyte solution to improve cell performance [2, 4].

The electrons injected on the conduction band of the oxide semiconductor can run into recombination with oxidized ions present in the electrolyte instead of being collected by the TCO. This charge recombination is also called dark current which lowers the current that the cell can supply. In order to suppress this current as much as possible, additives are added in the electrolyte solution.

3.3.4 Counter electrodes and catalyst

Tri-iodide ions, I_3^-, formed by the reduction of dye cations with I^- ion, are re-reduced to I^- ions at the counter electrode, as described section 3.2.2. To reduce the tri-iodide ions, the counter electrode must have high electrocatalytic activity. To provide the counter-electrode this property, a catalyst is deposited on its surface. The catalyst has the function of accelerating the transfer of electrons from the photo-cathode to the tri-iodide ion. The presence of the catalyst is not indispensable for the functioning of the cell, but the solutions that implement it show a higher DSC efficiency. The deposition on the TCO-glass should lead to a catalyst surface as porous as possible, to increase the effective contact surface with the electrolyte. There are several solutions, with different costs and benefits:

- the graphite is the most used catalyst used in the DSC. Although it is a good catalyst, however, its deposition on the TCO-glass is challenging;
- the PEDOT is a polymer made from conductive doped PSS. Its solubility allows homogeneous deposition compared to the graphite;
- the two previous solutions can be put together giving the graphite PEDOT/PSS;
- the PEDOT/PSS conductive nanotubes CNT leverages the capabilities and mechanical properties of carbon nanotubes;
- platinum provides significant increases in DSC efficiency and then it is the most used catalyst in DSC manufacturing. On the other hand, it presents a high cost respect to the previous options.

Pt coated on TCO substrate (5-10 $\mu g/cm^2$ or approximately 200nm thickness) or carbon are usually used as the counter electrode.

3.3.5 Encapsulation

The encapsulation is a main challenge in the design of solar cell that uses liquid electrolyte. In fact a disadvantage of this kind of solar cell is the loss of solvent and the evaporation of the electrolyte. A sealing material is needed to prevent the leakage of the electrolyte and the chemical and photochemical stability the electrolyte components. Surlyn (Du Pont), a copolymer of ethylene and acrylic acid, meets these requirements. Alternatively, to avoid the issues related to the use of a liquid electrolyte, the liquid electrolyte can be substituted with a p-type semiconductor, but the conversion efficiency is significantly lower compared to liquid electrolytes.

3.4 Advantages and disadvantages

The DSC have a number of attractive features. They are simple to make using conventional doctor blading or roll-printing techniques, is semi-flexible and semi-transparent which offers a variety of uses not applicable to glass-based systems, and most of the materials used are low-cost. In practice it has proven difficult to eliminate a number of expensive materials, notably platinum and ruthenium, and the liquid electrolyte presents a serious challenge to making a cell suitable for use in all weather. Although its conversion efficiency is less than the best thin-film cells, in theory its price/performance ratio should be good enough to allow them to compete with fossil fuel electrical generation by achieving grid parity. Commercial applications, which were held up due to chemical stability problems, are now forecast in the European Union Photovoltaic Roadmap to significantly contribute to renewable electricity generation by 2020.
The DSC have other unique characteristics which are summarized in the following:

- high energy conversion efficiency: a DSC efficiency equal to that of the amorphous-Si solar cell has been obtained during laboratory development and efficiencies greater than 10% may be possible;
- low-cost fabrication: the DSC are very simple to construct and are made of low-cost materials. Fabrication costs will therefore be less than that for conventional solar cells. For instance, US \$0.60/W, which may be competitive for conventional solar cells, has been estimated for a DSC with 10% efficiency [66];
- abundant supply of component materials: oxide semiconductors such as TiO_2, dye, and iodine are abundantly available. Although metal deposits of Ru are limited, the amount of Ru complex used in the DSC is only 1×10^{-7} mol/cm^2. Eventually,

organic dye photo-sensitizers could be used rather than Ru complexes if resource limitation is a problem;

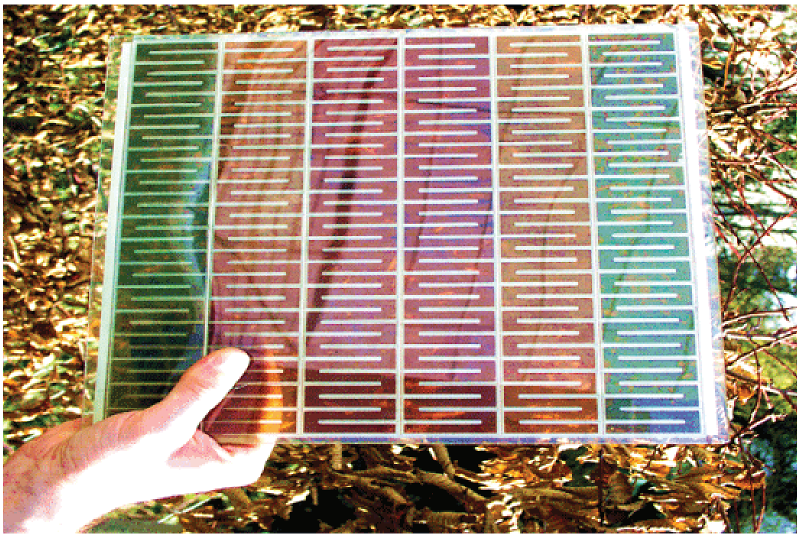

FIGURE 3.14: Example of a DSC panel with different dyes and then different colors. The possibility to set the panel color is one of the advantages of DSC technology.

- good potential for colorful, adaptable consumer products: colorful and transparent solar cells can be made using various kinds of dyes, depending on the use of the cell see Fig. 3.14;

FIGURE 3.15: Housing application of DSC panels.

- transparency. For example, transparent solar cells could be used in place of windowpanes 3.15 or as a coverage for greenhouses, see Fig. 3.16. Additionally, the use of a plastic substrate, rather than glass, is possible if low temperature processing of the TiO_2 film preparation ($<250\,^\circ C$) is available and would expand the use of DSC;

FIGURE 3.16: Greenhouse application of DSC panels.

- higher efficiency at low illumination intensity if compared with other PV technology. This will open DSC market to indoor applications;
- low potential for environmental pollution: the TiO_2, dyes, and iodine used in the DSC are nontoxic. The only component that could potentially cause harm is the organic solvents used in the electrolyte solution. Future research should be directed toward developing a solid-state electrolyte;
- good recyclability: the organic dye photo-sensitizers adsorbed on the electrode can be removed by washing the electrode with alkali solutions or combustion, providing recyclability of the DSC.

The major issues regarding DSC are summarized as follows:

- liquid electrolyte, which has temperature stability problems. At low temperatures the electrolyte can freeze, ending power production and potentially leading to physical damage. Higher temperatures cause the liquid to expand, making sealing the panels a serious problem;
- even though their required quantities are very low, ruthenium-based dye and platinum (as catalyst) have a high cost;
- TCO (ITO) or plastic (contact) are needed to produce a DSC. However, it must be reminded that this cost is present even in other TF technology;
- encapsulation issues: the electrolyte solution contains volatile organic compounds, solvents which must be carefully sealed as they are hazardous to human health and the environment.

As listed above, the major issues regards the presence of an liquid electrolyte and then the encapsulation. Replacing the liquid electrolyte with a solid has been a major ongoing field of research. Recent experiments using solidified melted salts have shown some promise, but currently suffer from higher degradation during continued operation, and are not flexible [67]. Another solution is to substitute the liquid electrolyte with a type p organic semiconductor. Even though it has been proven that this solution guarantees the functioning of the cell, the efficiency of this DSC is lower than the efficiency of a DSC that implies a liquid electrolyte. In addition, must be reminded that this solution does not totally avoid the encapsulation issue: in fact, if the p organic semiconductor is used instead of the liquid electrolyte, it must be not sensitive to air. Nevertheless, recent discoveries demonstrated that it is possible to produce organic semiconductors that do not react with oxygen/water moisture.

Chapter 4

Methodology

4.1 Introduction

This chapter describes the characterization methods and the accelerated stress technique adopted during this work. In addition, it provides a short description of the device used during the experiments and the fabrication process which allows to fabricate them.

4.2 Devices

In this work, we studied ruthenium-based dye-sensitized solar cells (DSC) made on a glass substrate. The DSC structure and fabrication process are presented in the followings. The core of each cell is a mesoporous titanium dioxide (TiO_2) layer on which is anchored the sensitizing material. The core of each cell is the TiO_2at which is anchored the sensitized material. The 12μm-TiO_2layer is deposited on one of the conductive TCO-glass substrates by sintering nanoparticles of TiO_2at high temperature 450°C. In order to improve the cell performance, an additional TiO_2scattering layer is deposited on the previous TiO_2layer. The ruthenium-based dye used in this work is called N719 and it is one of the most used sensitizer for DSC, due to its great properties in terms of thermal stability and efficiency (see subsection 3.3.2 for more details). This dye is impregnated onto the TiO_2. The resulting active area, which harvests the sunlight, is 25mm^2. Using a thermoplastic gasket, the working electrode is hot-sealed with the second conductive Platinum-coated TCO-glass substrate, which acts as the counter electrode. Finally, the tri-iodide/iodide (I_3^-/I^-) based liquid electrolyte is injected in the structure through the counter electrode by vacuum back filling technique. The pinhole is finally sealed by the same thermoplastic sealant previously used [68]. Alternatively, on the gasket a little path is made before to inject the Iodine/Iodide-based liquid electrolyte into the structure

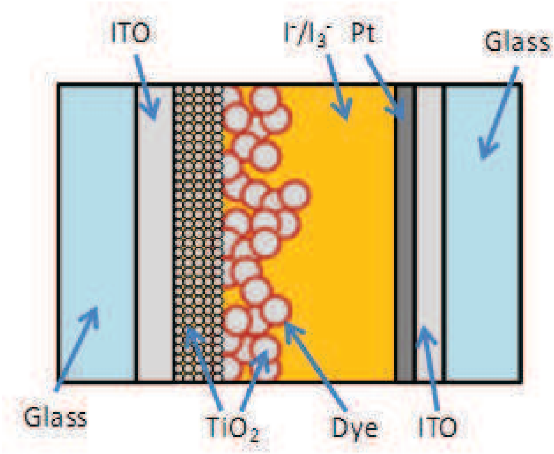

FIGURE 4.1: Structure of DSC used in this work. From left to right: glass substrate, TCO (FTO), double-layer of TiO_2, monolayer of dye (N719), electrolyte (I_3^-/I^-), Pt layer, TCO (FTO), and glass substrate.

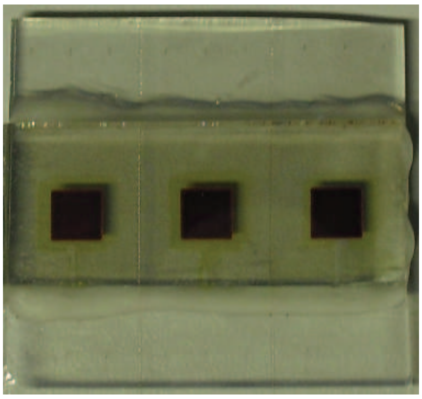

FIGURE 4.2: An prototype of DSC sample used in this work, featuring three isolated cell.

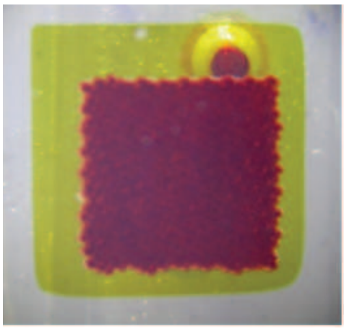

FIGURE 4.3: A magnification of the active area of a DSC. The solar cells studied in this work have an active area of $25mm^2$.

by vacuum back filling technique. The path is finally closed depositing a drop of UV curable glue on entrance of the path. These two methods to inject the electrolyte and the sealing of the injection path are equally reliable. Each sample contains three electrically isolated solar cells as shown in Fig. 4.2 and in Fig. 4.3 a magnification of the active area is shown. Due to the structure and shape of these samples, a description of the connections of the DSC substrates is mandatory. Referring to Fig. 4.4(which the side view of the sample reported in Fig. 4.2), as described previously, a substrate contains three DSC sandwiched between two glasses. The bottom glass contains contacts that face upward and they are the photo-cathodes while the upper glass contains contacts that face downward and they are the photo-anodes. Since the unique shape of this device, how to electrically connect to the instruments is not straightforward. The next section will describe how the electrical connection were made.

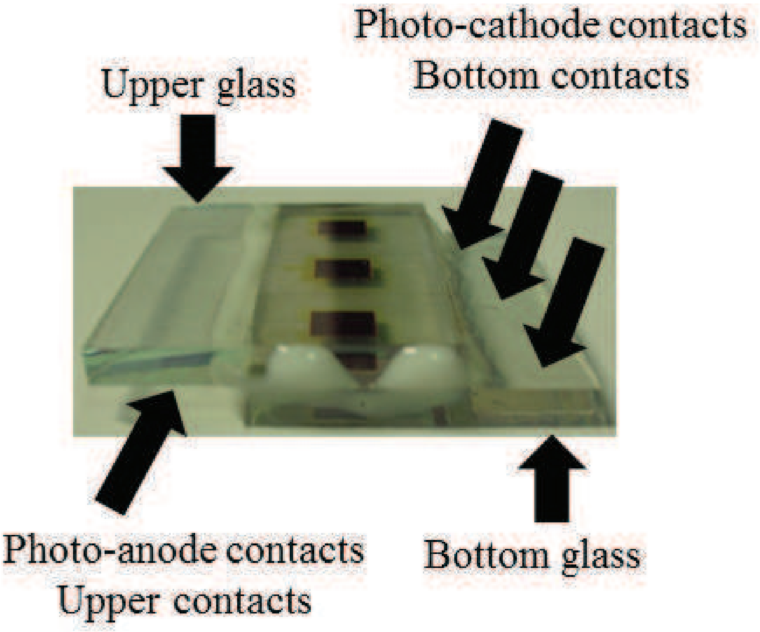

Figure 4.4: DSC substrate side view.

4.3 DSC characterization and measurement setup

4.3.1 Materials characterization

In this work, we mainly focused on the electrical characterization of the solar cells as described in the previous subsections. However, in order to have more information about the knowledge about the devices, we carried out environmental scanning electron microscope (ESEM) measurements. We asked CHOSE to prepare some ”‘open”’ substrates in order to perform this kind of measurements. CHOSE produced some substrates made of:

a glass substrate with the TCO layer which has on top the sensitized titanium dioxide. The $TiO_2$is sensitized with the same dye described in the previous sections. In order to avoid devices contamination due to air composition, this device were kept in a controlled environment till measurements were performed.

Briefly, ESEM is a scanning electron microscope (SEM) that allows for the option of collecting electron micrographs of specimens that are ”‘wet”’, not coated, or both by allowing for a gaseous environment in the specimen chamber. In the followings, some graphs and images of the data collected from ESEM measurements are shown. We collected data about the composition of glass, TCO, and the sensitized TiO_2. Fig. 4.5 shows three plots about three different position in the analyzed substrate. In particular, graph number 1 refers to the glass and as shows by the plot, this substrate contains the

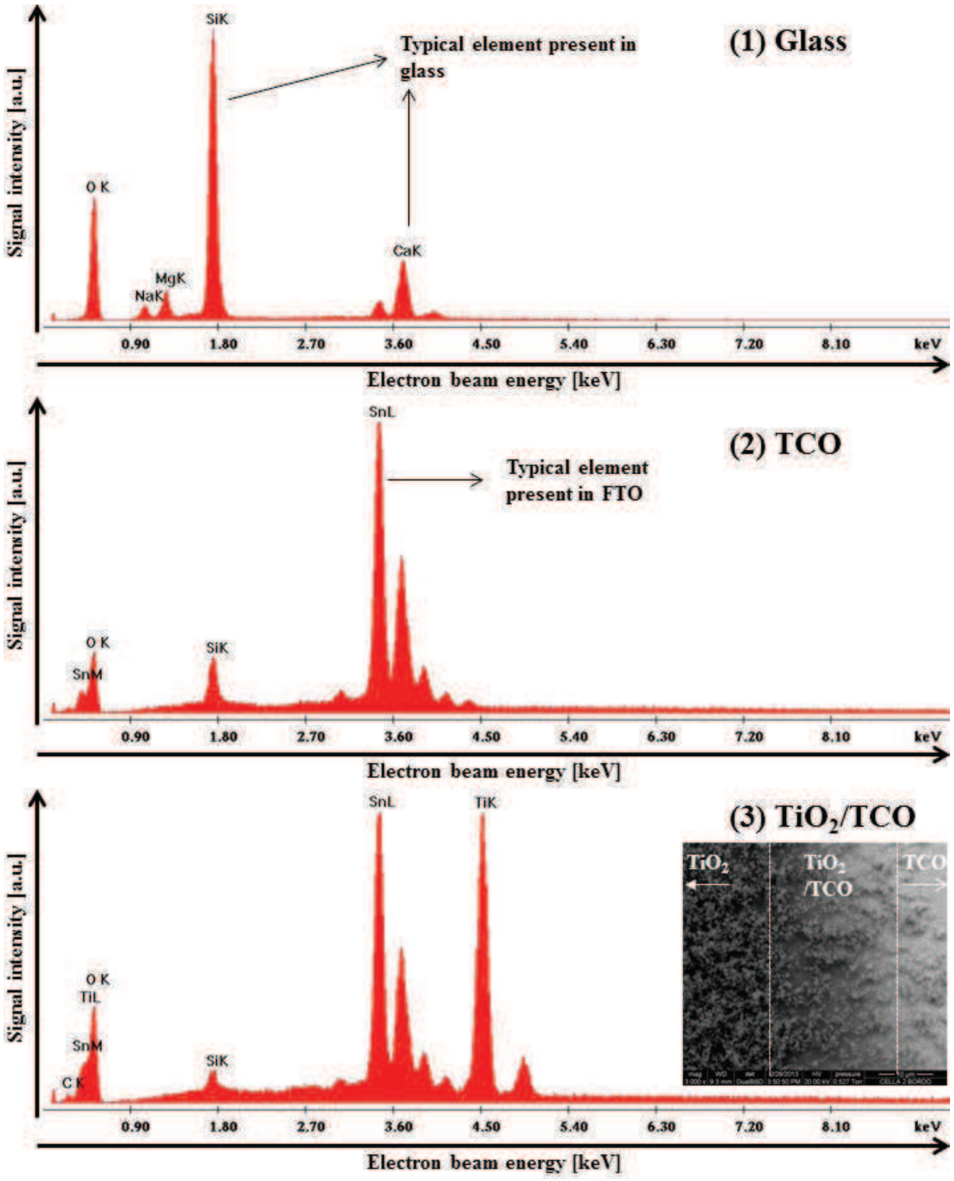

FIGURE 4.5: ESEM plots of: 1) glass substrate, 2) TCO and in particular fluorine doped, and 3) transition region from TCO and titanium dioxide.

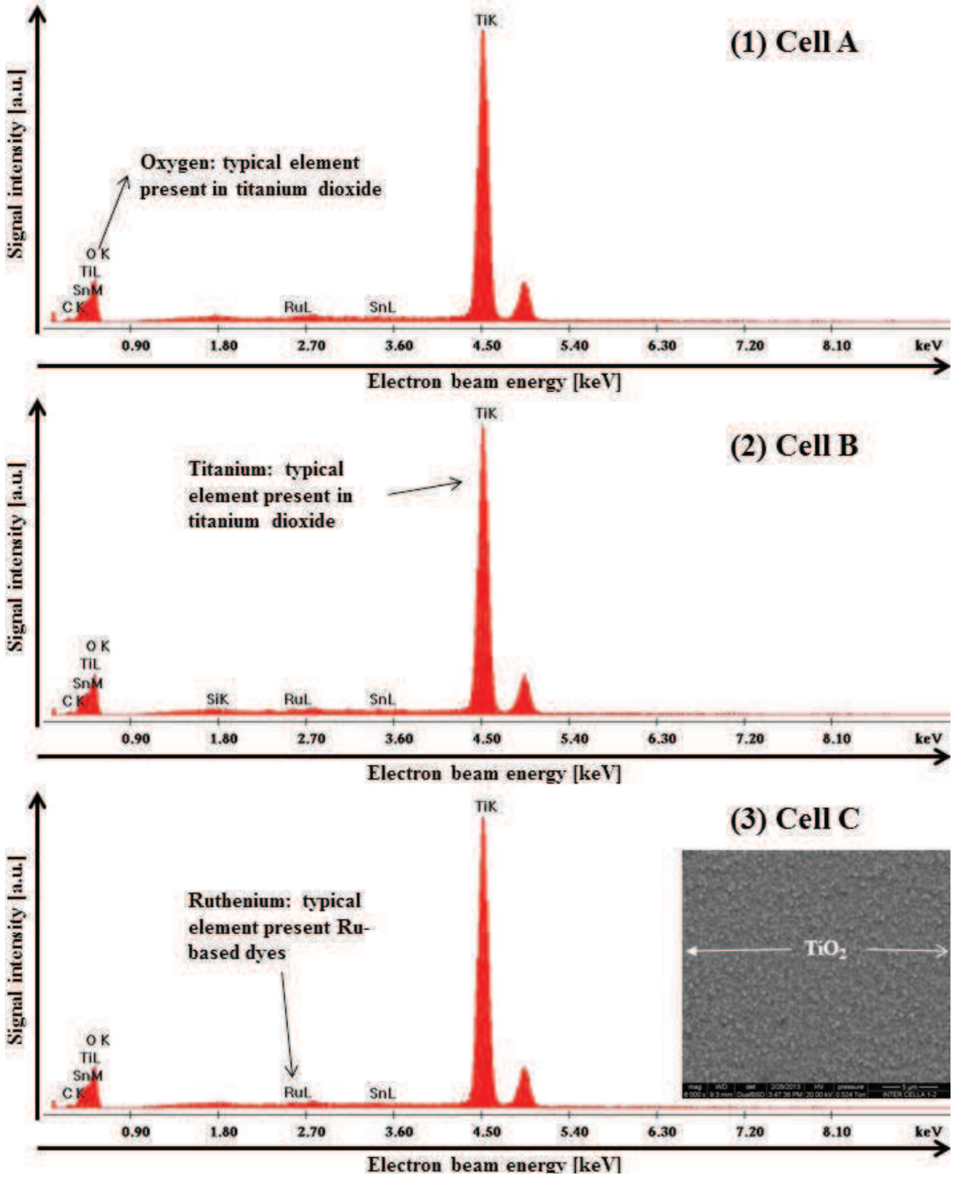

FIGURE 4.6: As described previously, a substrate contains three solar cells. The ESEM plots of show the composition of the center of the active area of the three solar cells.

typical element present in glass, that is: silicon oxide (SiO_2, the most present in the glass), lime (CaO), and sodium oxide (Na_2O). Graph number 2 shows the composition of the TCO, in particular fluorine doped indium-tin-oxide (ITO), which contains a large amount of tin oxide (SnO_2). The TCO is present all over in the glass substrate and the titanium dioxide is deposited only in a small portion of it. In particular, as discussed above, the area of the $TiO_2$is 25mm^2. Graph number 3 shows the transition region from the TCO to the TiO_2. As shown in the inset of graph TCO and $TiO_2$are simultaneously present in this region and in fact in graph 3 the intensities of the titanium dioxide and tin oxide are almost equal.

Fig. 4.6 shows the ESEM measurements taken in the center of the active area, that is where elements such as $TiO_2$and ruthenium are expected. There measurements are useful in order to analyzed the composition uniformity of the active area of the DSC in the substrate. The cells in the substrate are marked as A, B, and C. Basically, the signal intensities show that the TiO_2composition is uniform in all the three cell. Since the Ru-based dye is present as a monolayer onto the titanium dioxide surface, the Ru intensity signals (marked as RuL) are very weak respect to the one of the TiO_2. Since the a very large amount of DSC studied in this work and the very time consuming of ESEM measurements, not all devices were characterized by means of this technique; we chose a sample of devices to characterize for each DSC batch provided from CHOSE.

4.3.2 DC and impedance characterization

The reliability study begins with the preliminary characterization of the fresh device. The characterization is performed inside a metallic box, which ensures the electrostatic shielding and it prevents any disturbs from the environmental illumination and at room temperature. The DSC characterization consists of DC and impedance measurements usually performed under an optical intensity of 1 Sun (100mW/cm^2), provided by a xenon lamp solar simulator.
In the followings DC and impedance measurements are explained separately.

4.3.2.1 DSC DC Figures

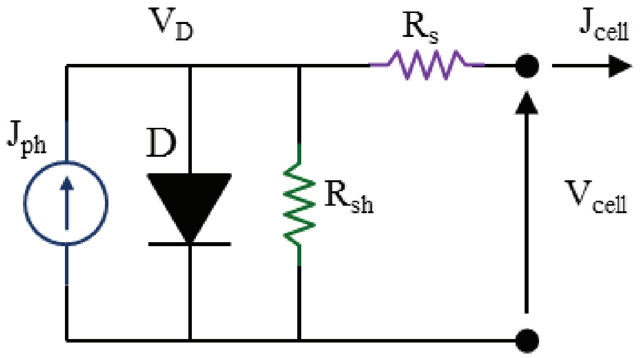

FIGURE 4.7: Basic DSC DC model.

Concerning DC measurements, the DC model of a DSC is reported in Fig. 4.7, and it consists of:

- an ideal current generator, which supplies current (J_{ph}) according to the illumination intensity shining on the cell;
- an ideal diode (D), which accounts for the drift current when V_{cell} >0;

- R_{Sh}, shunt resistance, which takes into account the internal charge recombination. This resistance affects the V_{OC} ;
- R_S, series resistance, which is the sum of all the series resistances introduced by each material present in DSC, for instance the contact resistances. This resistance affects the I_{SC} .

The DC measurements performed are: open-circuit voltage (V_{OC}), short-circuit current (I_{SC}), and the current density-voltage curves (J-V). According to the DC model the V_{OC} and I_{SC} are define as follows:

- V_{OC} is the difference of electrical potential between the anode and the cathode of the solar cell when the cell is not driving any load, in other words when $I_{cell} = 0$;
- J_{SC} is the current that the cell supplies when the anode and the cathode of the cell are short circuited, that is when $V_{cell} = 0$.

$$V_{OC} = V_{cell}\left(I_{cell} = 0\right) \tag{4.1}$$

$$J_{SC} = J_{cell}\left(V_{cell} = 0\right) \tag{4.2}$$

Eq. 4.1 and 4.2 summarize the definition of V_{OC} and J_{SC} . Concerning the current-voltage characteristic and according to solar cell characterization standards, the J-V is measured sweeping V_{cell} from V_{OC} to 0, back and forth. Fig. 4.8 shows an example of a J-V characteristic of DSC and multiplying V_{cell} by I_{cell} we obtain the P_{out}-V characteristic which shows the electrical power that the cell can supply regarding to the load voltage. Besides V_{OC} and J_{SC} , there are other solar cell figures: the efficiency (η) and the fill factor (FF) which are calculated from the J-V and P_{out}-V characteristics. The efficiency is the ratio of the maximum power supplied to the solar cell and the illumination intensity shining on the cell. The fill-factor is define as the ration of the maximum power supplied to the cell and the V_{OC} x I_{SC} product.

$$\eta = \frac{P_{max}}{I_{Sun}} = \frac{V_{max} I_{max}}{I_{Sun}}, usually I_{Sun} = 100 mW/cm^2 \tag{4.3}$$

$$FF = \frac{P_{max}}{V_{OC} J_{SC}} \tag{4.4}$$

Eq. 4.3 and 4.4 summarize the definitions of efficiency and fill-factor.

4.3.2.2 Impedance measurements: EIS basic concepts

In order to characterize DSC and to better analyze the degradation of DSC subjected to accelerated stresses, we performed Electrochemical Impedance Spectroscopy (EIS). Such

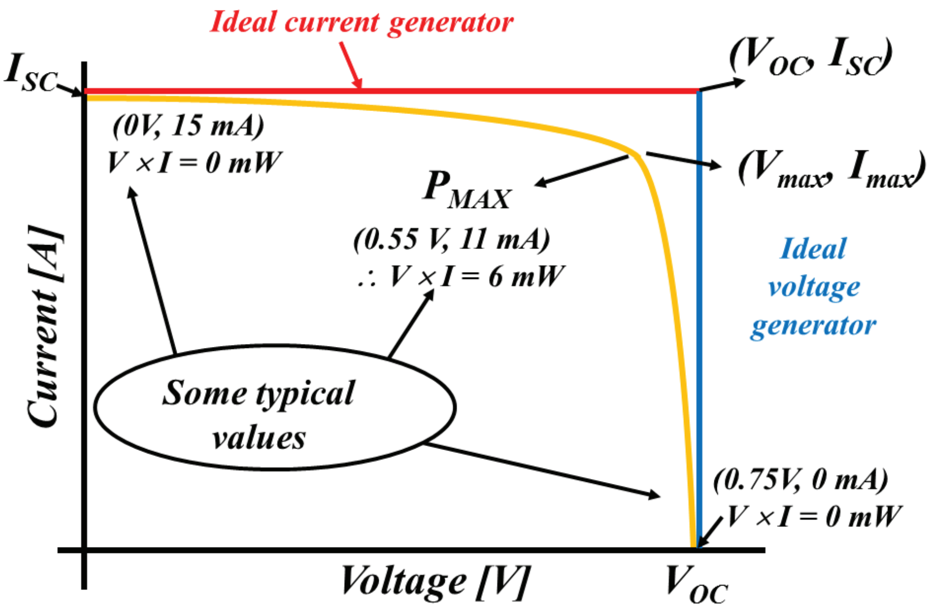

Figure 4.8: Typical J-V characteristic of DSC with some examples of typical values.

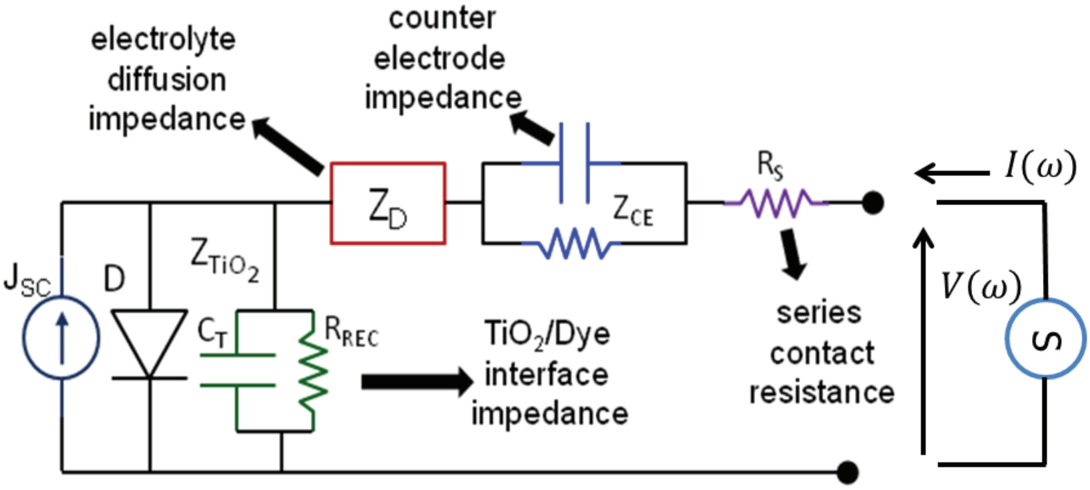

Figure 4.9: Basic DSC impedance model.

technique is widely applied to the characterization of electrode processes and complex interfaces, such as in a DSC device, where several layers and interfaces are involved in charge transport. Fig. 4.9, shows the simplified impedance model of a DSC [69]. The ideal current source simulates the photo-current generation at the TiO_2/Dye/Electrolyte interface; the impedance Z_P refers to the TiO_2/dye interface and to the inner recombination; Z_D is the Nernst diffusion impedance, which accounts for charge transport through the electrolyte; the impedance Z_{CE} refers to the charge exchange at the counter electrode interface; R_S accounts for the series contact resistance [70]. In order to measure the impedance of DSC a sinusoidal generator is applied to the device as shown in Fig.

4.9. The frequency of the voltage signal is usually swept from 500kHz to 50mHz and the corresponding current signal is recorded in order to calculated the device impedance. Fig.4.10 show the typical Nyquist plots of two DSC, where the real and the opposite of the imaginary parts of the impedance lay on the x-axis and the y-axis, respectively. The signal frequency increases from the right to the left side of the plot. The Nyquist diagram of a DSC typically features three semicircles that are attributed to: Nernst diffusion within the electrolyte, Z_D (right semicircle), the electron transfer at the TiO_2/Dye interface, Z_P (middle semicircle), and the red-ox reaction at the platinum counter electrode, Z_{CE} (left semicircle). See references [71] for additional details on DSC impedance model.

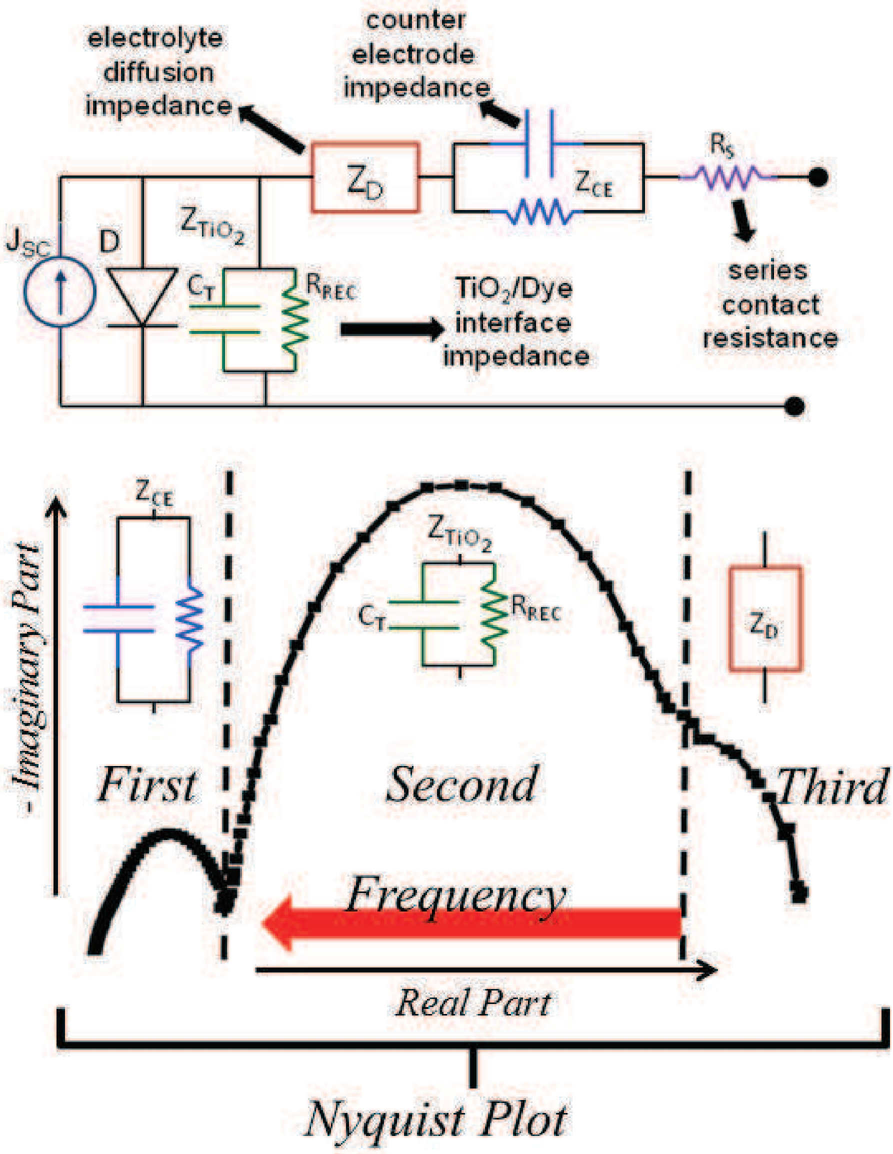

FIGURE 4.10: DSC impedance measurement by mean of electrochemical impedance spectroscopy.

4.3.3 Measurements setup

To obtain good and reproducible measurements we created an ”‘ad hoc”’ measurement setup. The importance to have repeatable measurements will be clear in the next section. We designed a measurement setup, Fig. 4.11, and exposure system, Fig. 4.12, which permit a fully-automated exposure and characterization with several light sources. Besides speeding up the measurements, this setup ensures: good and stable electrical contacts between the devices and the instruments; a reproducible and uniform exposure of all cells; and minimal experimental errors. The pictures do not show: a control board and the custom Matlab program written to drive all the whole measurement apparatus. The design and realization of all these facilities took a lot of time and are integral parts of the PhD course.

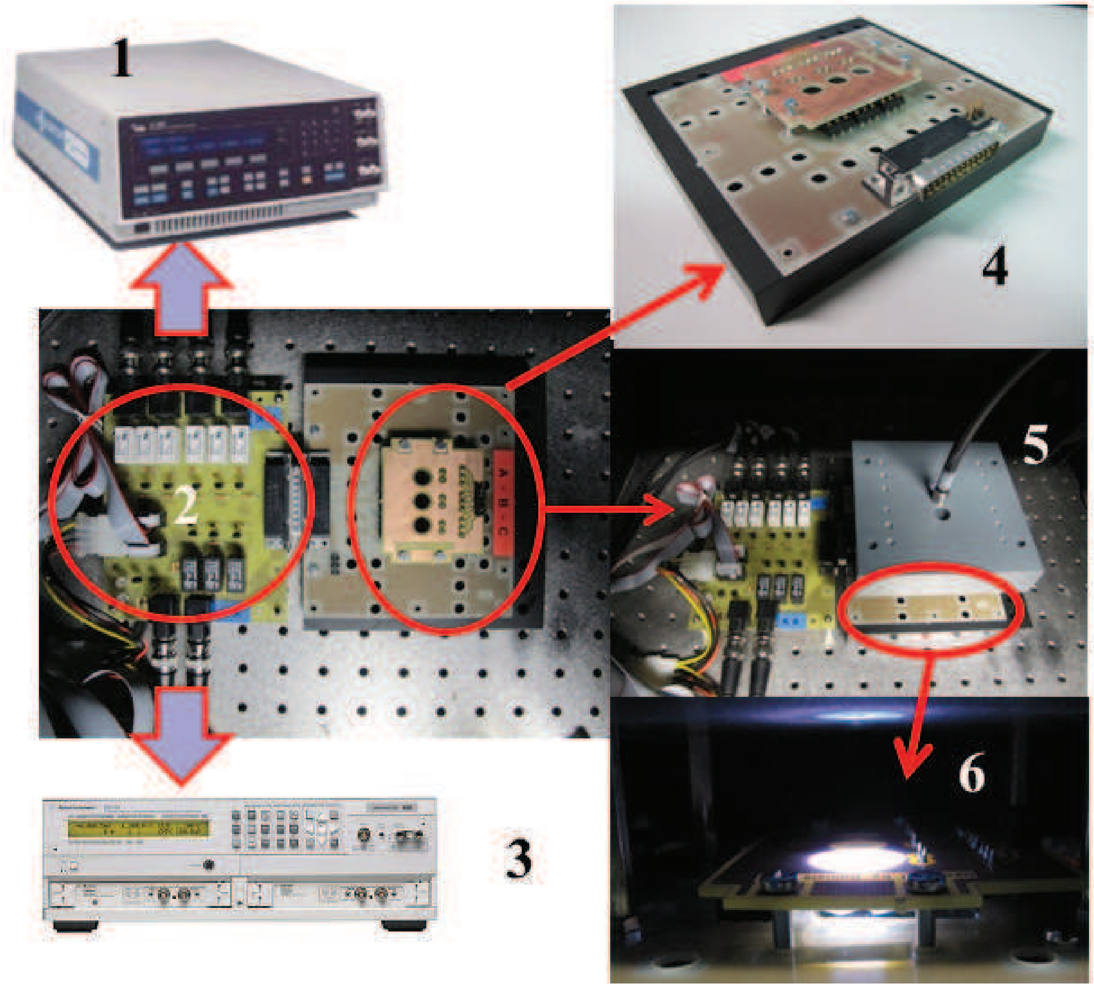

FIGURE 4.11: Measurements apparatus.

A list of all the instruments showed in Fig. 4.11 used to performed the measurements described above is presented here.

1. Impedance analyzer Schlumberger SI1260, marked as 1 in Fig. 4.11;

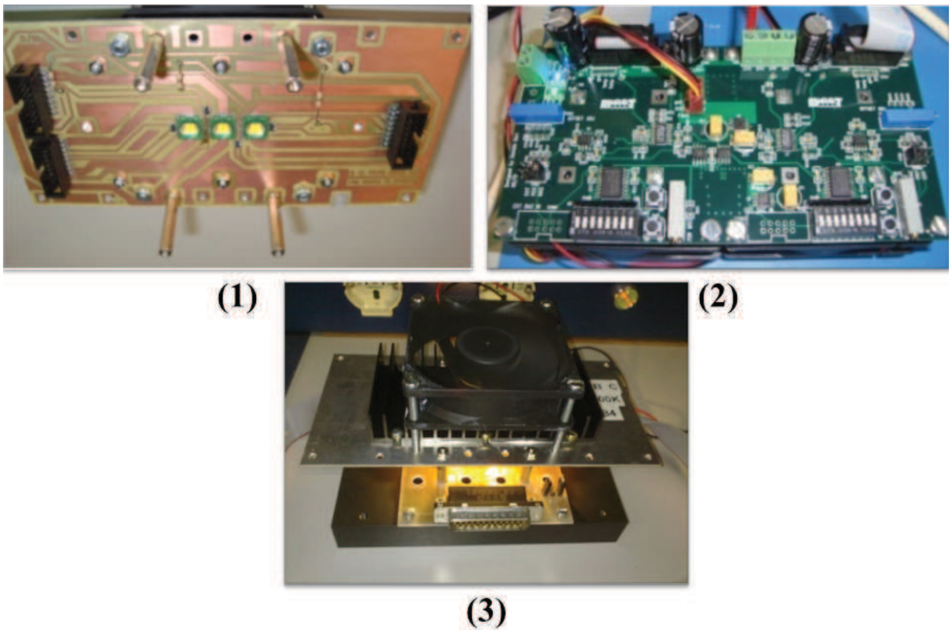

Figure 4.12: Illumination apparatus.

2. Instruments switch, marked as 2 in Fig. 4.11;
3. Parameter analyzer Agilent E5263A, marked as 3 in Fig. 4.11;
4. DSC sample holder, marked as 4 in Fig. 4.11;
5. Fiber optic sample holder, marked as 5 in Fig. 4.11;
6. Newport AM 1.5 solar simulator and fiber optics, not reported in Fig. 4.11 but it is showed in the next section.

In the followings, a brief description of all these items is reported.

We designed and implemented a custom sample-holder, as shown in Fig. 4.13. The design of the sample holder went through different stages. The sample holder depicted

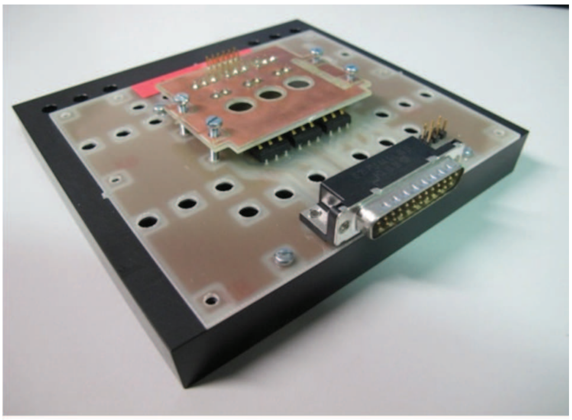

Figure 4.13: DSC substrate sample holder.

in Fig. 4.13 is the last version. The sample holder consists of: a PVC base, a main PCB, and a top PCB. The PVC base hosts the other sample holder parts and guarantees mechanical strength. It has on the top surface some holes (which are also present in the main PCB) with a specific depth and they are sockets for the illuminator system and/or for the fiber optics holder. The main PCB hosts: a parallel port DB25, a set of spring probes (alternatively planar contacts), and three couples of two-pins contacts. The DB25 parallel port connects the DSC to the instruments switch (marked as 2 in Fig. 4.11) and in turn to the instruments; the spring probes (alternatively planar contacts) connect the photo-anodes to the DB25 port; the three two-pins contacts allow the user to have direct access to the photo-anodes/cathodes of the DSC. The top PCB has a set of spring probes (alternatively planar contacts) and has a twofold purpose: firstly, it collects the photo-cathode contacts and it makes them connected with the main PCB; secondly, it acts as a clip. In fact, using four screws the top PCB is hold down and it pushes either the spring probes on itself and those in the main PCB against the substrate contacts. This method guarantees a repeatable measurement error between 1-2%. The data collected during the repeatable trials are not here reported due to lack of space. About 15-20 sample holders were created, that is 15 PVC bases, 15 main PCBs, 15 top PCBs. One of the first version of the sample holder used a conducting tape as a contact instead of the spring probes or the planar contacts. The contact between the tape and the contact pad on the substrate was made by sandwiching and pressing the substrate between the PVC base and the main PCB and a metallic clip. This method gives a repeatable measurements error worse than the newer sample holder.

The instruments switch, Fig. 4.14 and marked as 2 in Fig. 4.11, allows to connect the three solar cells hold in the sample holder, with the impedance and parameter analyzer. It consists of: a set of BNC, which connect the instruments with the switch, a DB25 port, which connects the sample holder with the switch, and a 9 relays (three for the parameter analyzer and 6 for the impedance analyzer), which allow to connect the a solar cell in the substrate in the sample holder with one of the instruments. Two instruments switches were assembled and realized (one is required for the apparatus, the other one is for backup). The instruments switch is controlled by a control board (not showed) and it is controlled by a Matlab program (not showed and described thoroughly). Briefly, the Matlab allows the user to: perform a single characterization measurements (V_{OC}, I_{SC}, J-V, and EIS); set all the measurement parameters; save the measurement as a text file; create a log file for each measurement session and allow to retrieve it to append new measurements; perform a plan of measurements with different illumination intensities for each measurement. This is just a subset of the features that the Matlab program allow to do.

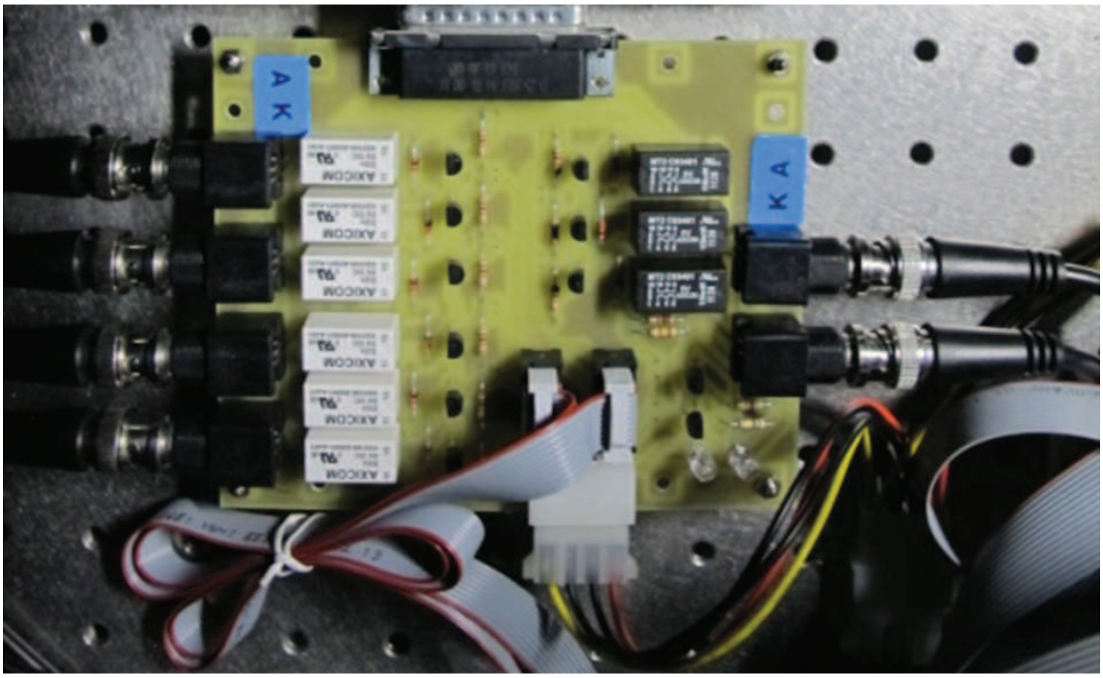

FIGURE 4.14: Instruments switch.

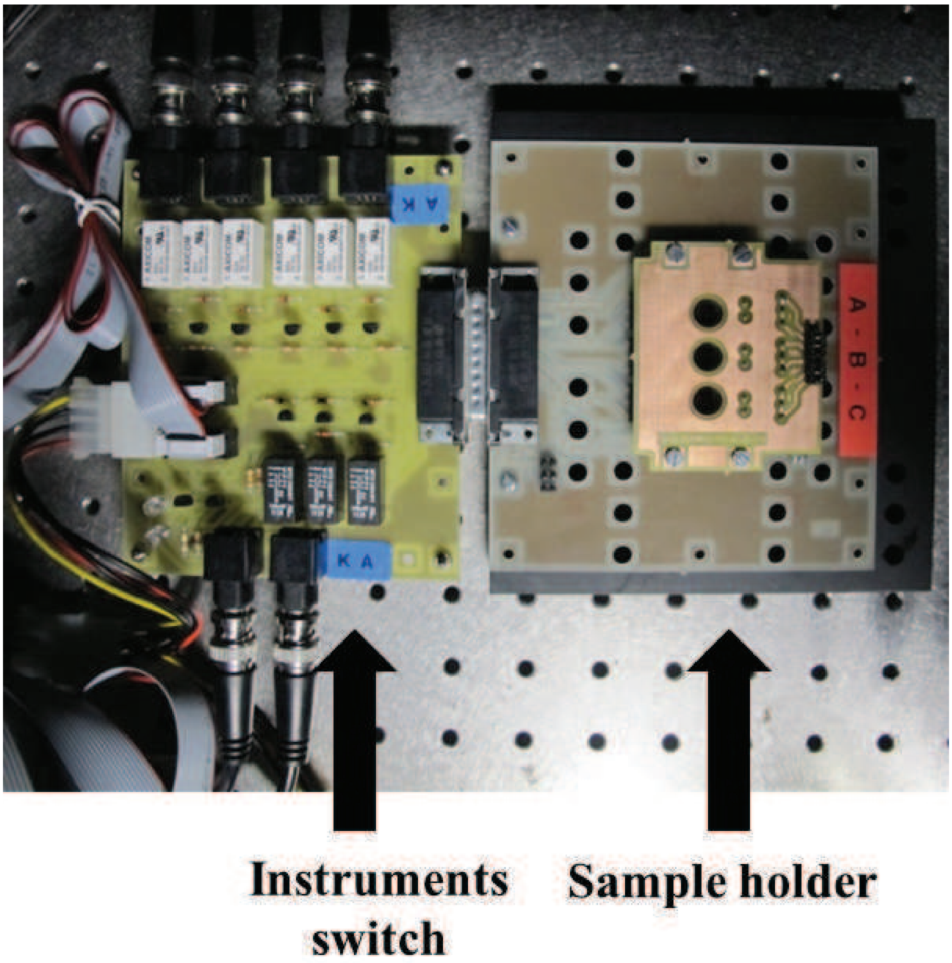

FIGURE 4.15: Instruments switch and sample holder connected.

The illumination apparatus showed in Fig. 4.12, consists of: an illuminator and a current driver, marked as 1 and 2 in Fig. 4.12. The illuminator consists of: a PCB metal core, three high power LEDs, three 16-pins headers, four screws, a heat sink with fan. The three LEDs have the same spectrum and they could have: UV, violet, blue, green, red, IR, or white spectrum. LEDs are soldered on a metal core PCB by means of a Pb-free tin solder paste and the soldering is made by a reflow system. The 16-pins header allows the connection of the board with the current driver. The metal core, heat sink, and the fan allow to dissipate the heat produced by the LEDs. The four screws allow to mount the illuminator on the DSC sample holder as illustrated in Fig. 4.12 (see picture number 3). Since the position of the four holes in the DSC sample holder are fixed as well as the postion of four screws in the illuminator is, the distance between the LEDs and the solar cells is always the same. This is crucial when performing accelerated stresses by means of LEDs: since we want to keep track of the cell degradation, accelerated stresses are periodically stopped to perform characterization measurements. When measurements are done, the accelerated stress will be resumed and it is important to place the illuminator in the same position as it was in the previous step stress. If this does not occur, the cell will be illuminated with a different illumination intensity respect to the one used in the previous step stress getting the next data useless for the comparison with the data collected till then.
In order to drive these LEDs properly, a high power current driver was designed and assembled. Each current drivers has one or two channel per board. About 10 illuminators were realized. About 10 current drivers were assembled, 6 dual channels and 6 one channel.

The fiber optic holder, marked as 5 in Fig. 4.11 is used when the characterization by means of AM1.5 solar simulator is performed. In Fig. 4.11, it is mounted on the sample holder. It consists of a PVC base and four screws. The PVC base has three holes (as three cells in a glass substrate) to host the fiber optic: moving the fiber optic from a hole to another, it illuminates one of the three cells in the substrate. Four screws are mounted on the PVC base and they allow to match those hole displayed on the PVC base in the sample holder. Since the beam that exit the fiber optic is not uniform, this system allows to illuminate the cell with the same illumination intensity since the end of the fiber optic is placed at same distance from the solar cell every time a measurements by means of solar simulator is performed.

4.4 Accelerated stresses

According to the standards, the lifetime of a solar cell is the elapsed time under 1 Sun exposure after that the efficiency of the cell is supposed to be the 80% of its initial value. However, when performing a reliability study, besides efficiency, it could be significant to observe the degradation kinetic of other cell figures, such as the open-circuit voltage, the short-circuit current, and the fill factor. Hereafter, in order to keep the concept as much general as possible, we will refer to these cells figures as cell performance.

A standard stress procedure is shown in Fig. 4.16. As describe in the previous section, all the accelerated stresses begin with a preliminary characterization of the fresh devices, *Step 1* in Fig. 4.16. After that, the devices are subjected to the stress factor (sunlight exposure, temperature, monochromatic light, current, etc.), *Step 2* in Fig. 4.16 and the accelerated stresses are periodically interrupted in order to perform devices characterization, *Step 3* in Fig. 4.16. This allows to keep track of the solar cells performance during the test. Basically, we followed a logarithmic scale for the step stresses, that is, the stress steps are: 1, 1, 2, 4, 8, 16, 32, and so on in order to record cell performance at these time: 0 (fresh), 1, 2, 4, 8, 16, 32, 64, and so on. This scheme is summarized in Tab. 4.1. The unit time measure of those points, could be: seconds (s), minutes (m), hours (h), or even days (d). In all our experiments we always referred to hours. Even though this is the most used procedure in the reliability study field, it does not always applies for all technologies. Especially when dealing with a new technology,

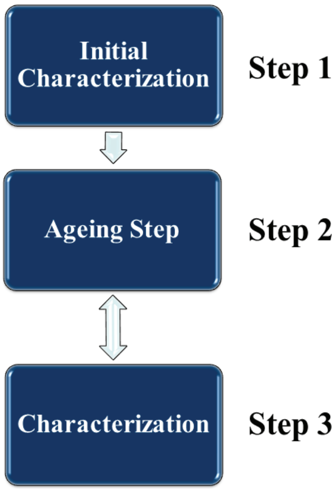

FIGURE 4.16: Standard accelerated stress procedure.

TABLE 4.1: Example of stress step

Step Stress	1	1	2	4	8	16
Stress Time	1	2	4	8	16	32

such as DSC, the stress procedure must be carefully evaluated in order to prevent data loss. In fact, some of the step stress described above, could be too long for the new technology (according to the magnitude of the stress factor) and then some data about the kinetic performance degradation can be lost. If the purpose of the reliability study is to gather the degradation kinetic of the cell performance, this must be taken into account
In order to understand the physics mechanism that lead to the degradation of DSC under sunlight exposure, we performed several accelerated stresses using different stress factors. The following subsections summarized all the accelerated stresses performed.

4.4.1 Accelerated stresses description

FIGURE 4.17: Low cost solar simulator. It implies a 150W Xenon lamp to reproduce the sunlight spectrum.

The first investigation concerned the optical stress and reliability study of DSC under sunlight exposure. The stress is performed by means of AM1.5 solar simulator (see Fig. 4.17) with illumination intensities ranging from 8 to 15 Sun: since 1 Sun = 100mW/cm^2 so they range from 800mW/cm^2 to 1500mW/cm^2. During illumination, each solar cell under stress is loaded with a 12-ohm resistor, which keeps the cell close to the short-circuit operating point. The choice of the load value is arbitrary, but it ensures that the cell works away from its point of maximum efficiency and in particular close to short circuit condition. Since each substrates contains three solar cells (see for reference Fig. 4.2), in order to avoid not stressed cells to light exposure we masked the neighboring cells. Nevertheless, those neighbors cell can be affected by passive thermal stress, since the substrate gains heat under sunlight exposure especially for high illumination intensities. Therefore, we decided to keep track also of the performance of these solar cells in order to assess the degradation (if any) due to passive thermal stress. The results of this accelerated stress are shown and discussed in Chapter 5 in section 5.1.

The sunlight exposure contains several stress factor for solar cells. First of all, as anticipated above, a solar cell exposed to sunlight gains heat and then its own temperature rises. Besides heat, the sunlight spectrum contains many components: UV, visible, and IR components. Finally, during solar cell operation, current flows inside the cell during light exposure. Therefore, it could be worth to investigate the effects (if any) on the performance of solar cells caused by all those factor separately. Then, the idea is to broke down the AM1.5 optical stress into smaller stresses in order to accomplish the purposes just described. The scheme reported in Fig. 4.18 shown the AM1.5 stress partitioning. It was split as listed below:

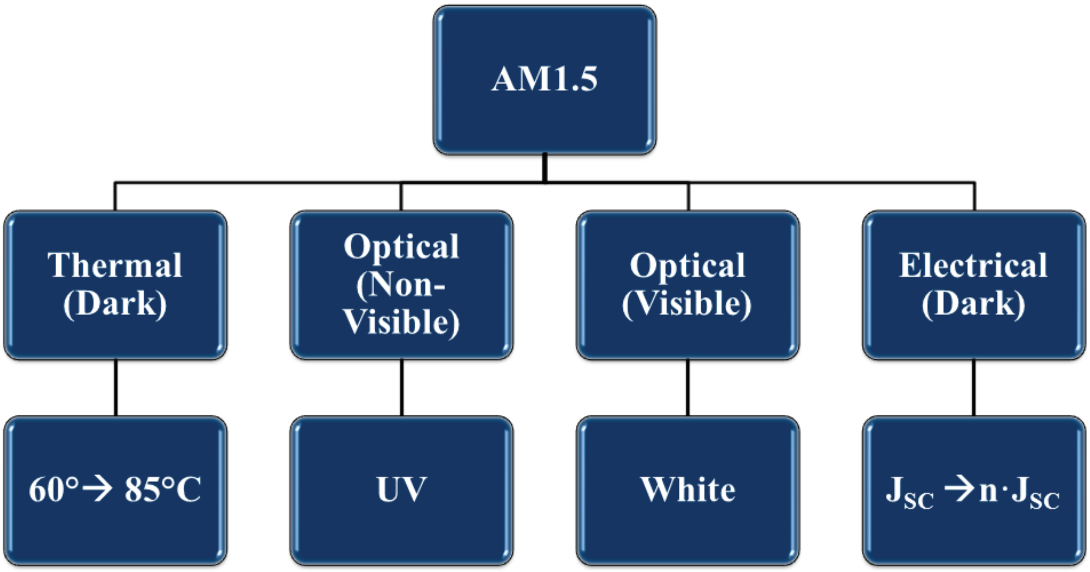

FIGURE 4.18: Stress plan.

- pure thermal stress;
- optical (non-visible) stress, stress performed with UV light;
- optical (visible) stress, stress performed with white light;
- electrical stress, in particular constant current stress (CCS).

The followings describe the procedure used for all the sub-stresses described above. As explained previously, all the accelerated stresses begin with a preliminary characterization of the fresh devices.

The pure thermal stresses were performing keeping the devices inside a climatic chamber (Fig. 4.19) in the dark at different constant temperatures ranging from 60°C to 85°C. These temperatures were chosen according to the temperature data gathered during AM1.5 solar simulator stress. In fact, during those accelerated stresses, we used either a

FIGURE 4.19: Climatic chamber.

thermocouple and a LM35 IC-based PCB[1] to measure the temperature of the glass substrate under artificial sunlight exposure. We found that the temperature under 15 Sun light exposure can reach temperature above 65°C. Besides, the chosen stress temperature of 85°C is the one used during solar cell panels characterization. Concerning the bias of the cells under test, all the devices were left in open-circuit condition. The stresses were periodically stopped in order to perform the characterization measurements and before that, the device were left to cool in order to prevent the effects of heat on measurements (it has to be reminded that all the measurements were carried out at room temperature).

Concerning the optical stresses with white light, this experiment has twofold purpose. On one hand, as indicated above, to assess the effects (if any) of visible light on the performance of DSC; on the other hand, we take into account a white LED-based light source as an alternative to AM1.5 solar simulator to perform the reliability study on dye-sensitized solar cells.

Conventional solar cells certification can be made by means of Xenon lamp-based solar simulators which easy achieve the IEC Standards [72]. Nevertheless, this kind of solar simulators are expensive, difficult to handle and optical intensity regulation could shorten the lamp lifetime. Many works in literature deal with the construction of LED-based solar simulators, which are cheap and easy to handle [73]. Several works show that I-V curves measured by using LED-based simulators can be converted to STC I-V characteristics by means of IEC Standard correction methods. In addition, many laboratory tests, like high power inverter for solar panels testing, are independent of illumination sources and LED-based solar simulators can be used instead of expensive

---

[1] (”‘ad hoc”’ to mimic the DSC substrate shape)

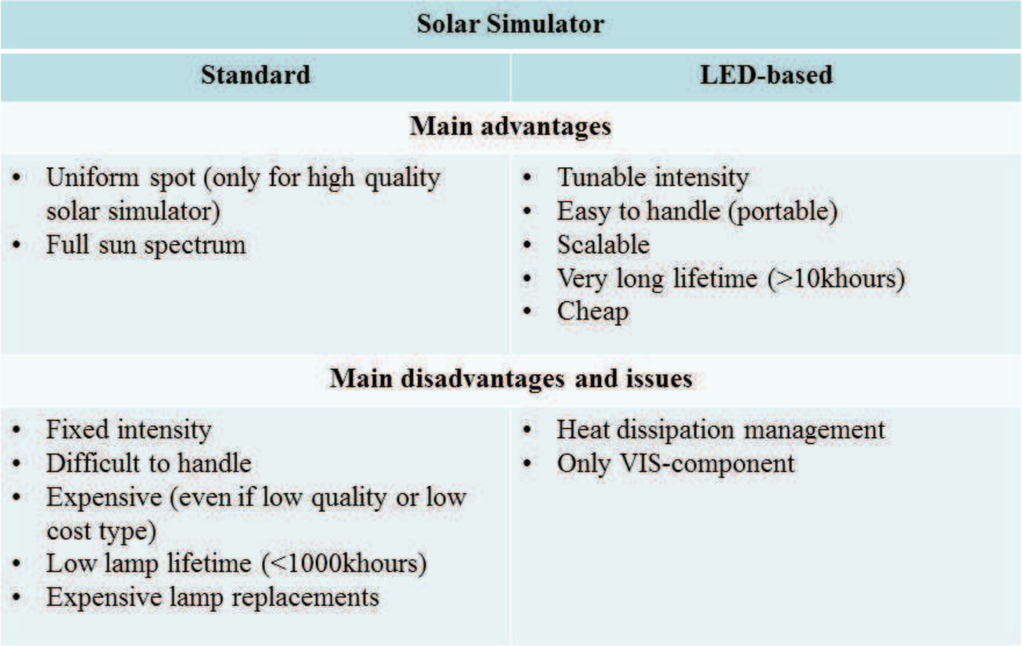

Solar Simulator	
Standard	**LED-based**
Main advantages	
• Uniform spot (only for high quality solar simulator) • Full sun spectrum	• Tunable intensity • Easy to handle (portable) • Scalable • Very long lifetime (>10khours) • Cheap
Main disadvantages and issues	
• Fixed intensity • Difficult to handle • Expensive (even if low quality or low cost type) • Low lamp lifetime (<1000khours) • Expensive lamp replacements	• Heat dissipation management • Only VIS-component

Figure 4.20: LED and standard solar simulator comparison.

AM1.5 solar simulators. Even if these new solar simulators are more and more used in many applications, few works deal with the suitability of LED-based solar simulators to perform characterization and reliability study of DSC. In Fig. 4.20 a comparison between standard AM1.5 solar simulator and LED-based solar simulator is reported.

We performed accelerated optical stresses by means of high power white LED (see Fig. 4.21) and during stress we performed the DC and EIS measurements with both white LED and AM1.5 solar simulator in order to find, if any, differences in kinetics degradation. In addition, during stress, we also performed characterization measurements using

Figure 4.21: High power white LED (100W).

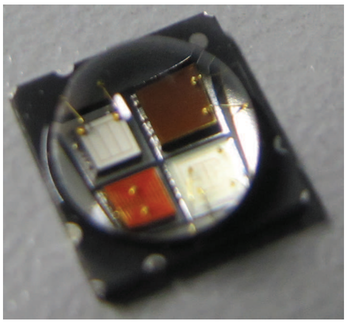

FIGURE 4.22: An example of RGBA LED soldered in a metal core shown in Fig. 4.12.

four monochromatic light sources, i.e. red, amber, blue, and green lights in order to understand if different light source characterizations could give additional information on the degradation mechanism involved on DSC. Fig. 4.22 shows an example of multicolor LED that was used. It has wavelengths of 630, 525, 460, and 590nm and hereafter, we will refer to these wavelengths with λ_i, where i can be: R (red), G (green), B (blue), and A (amber) respectively. Fig. 4.23 shows a comparison between: white-LED-based solar simulator, the multicolor LED spectra, and the absorption spectrum of the glass-DSC-glass stack.

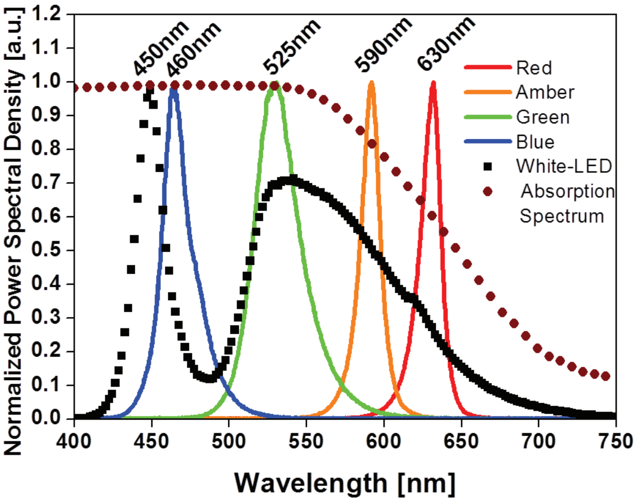

FIGURE 4.23: The emission spectrum density of the RGBA LEDs (continuous lines) and of White-LED (square dotted line) is shown. As comparison, it is reported the cell-stack absorption spectrum (point dot line).

In order to compare the characterization performed with the six different sources, we carried out the characterization at same optical intensity of 60mW/cm^2 for all sources, according to the maximum intensity that the less efficient LED can reach, in this case the amber LED. In addition, we also measured the external and internal quantum efficiencies (EQE and IQE) for all λ_i. EQE (λ_i) is the ratio of the I_{SC} measured under a monochromatic source (λ_i) divided by the number of incident photon per second. IQE (λ_i) was determined by dividing the EQE (λ_i) value by the absorption coefficient of the glass-DSC-glass stack at λ_i. After the characterization of the fresh devices, cells were illuminated at a constant optical intensity of 500mW/cm^2. During stress, the cells were loaded with a 12-ohm resistor, which keeps the cell close to short-circuit operating point and besides it is the same used during AM1.5 solar simulator accelerated stresses. In order to monitor cell performance, as usual, the stresses were periodically stopped to permit DC and impedance measurements.

We carried out UV illumination stresses by means of high power ultraviolet LEDs with 365-nm peak wavelength. For instance, Fig. 4.24 shows a UV LED soldered in one of those illuminator shown in Fig. 4.12. Fig. 4.25 reports a comparison between the spectrum of the Sun and and the spectrum of the ultraviolet LED used during this experiment. Since each substrate has three embedded cells, we decided to subject two of three cells to UV irradiation and the third cell was masked (not irradiated) and kept as reference device. Hereafter, we will refer to the masked cell as the reference device. We used six illumination intensities for irradiation stresses: 10mW/cm^2, 20mW/cm^2, 30mW/cm^2, 40mW/cm^2, 50mW/cm^2, and 100mW/cm^2, which are about 2, 4, 6, 8, 10, and 20 times the UV component of standard solar spectrum component respectively (see

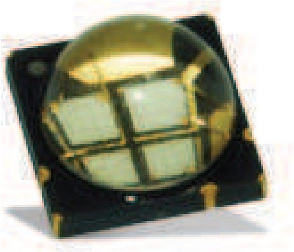

FIGURE 4.24: An example of UV LED soldered in a metal core shown in Fig. 4.12.

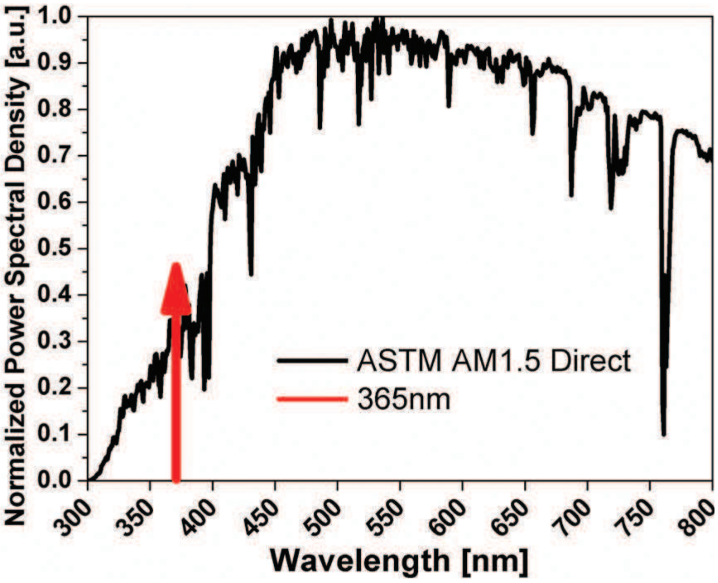

FIGURE 4.25: Stress UV spectra.

for instance standard table ASTM G173-03 [72]). During stress, each solar cell under stress is loaded with a 12-ohm resistor, which keeps the cell close to short-circuit operating point: as we did for the AM1.5 solar simulator stresses, the load value is chosen to ensure that the cell works close to short circuit condition during the entire stress. Still, in order to monitor cell performance, the stresses were periodically stopped to permit DC and impedance measurements.

Concerning the constant current stresses (CCS), we carried out two types of CCS: positive CCS, where the current flows inside the device from the counter electrode (CE), i.e. the cell acts like a load and it is the same direction that dark current flows; negative CCS, where the current flows inside the cells from the working-electrode (WE), i.e. the current flows in the same direction it should flow if the device works as a solar cell. Typically, these kinds of stress, positive and negative, are called forward and reverse current stresses respectively. Fig. 4.26 shows a schematic representation of the CCS carried out in this work. We arbitrarily chose two absolute current levels: J_{STRESS} = 30 and 40 mA/cm^2, for both positive and negative CCS. These current levels are about threefold and fourfold the J_{SC} of DSC under 1 Sun of illumination respectively. As for the other accelerated stresses, the stresses were periodically stopped to permit DC and impedance measurements in order to monitor cells performance.

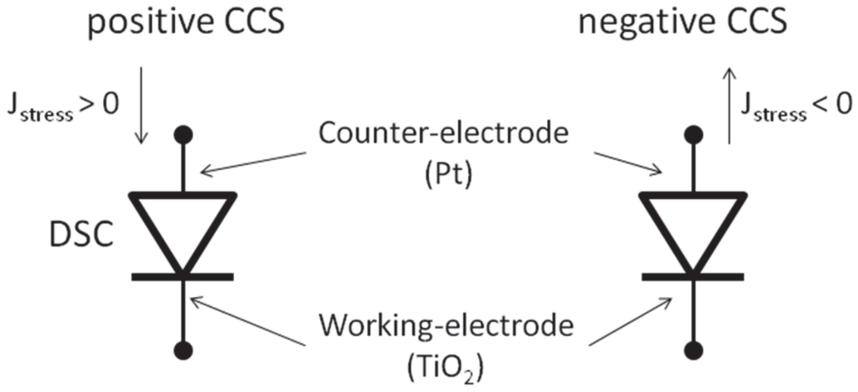

Figure 4.26: Constant current stress (CCS) scheme.

Chapter 5

Accelerated stresses: results and discussions

This chapter deals with the presentation and discussion of the results obtained from the accelerated stresses described in previous chapter. In particular, the chapter starts discussing the results obtained from the AM1.5 accelerated stresses and then, as described previously, it focuses on the discussion of the data collected during pure thermal, white light exposure and UV exposure, constant current stresses.

5.1 AM1.5 solar simulator accelerated stresses

5.1.1 Introduction

In this experiment, we studied the reliability of sensitized solar cells. The reliability study was carried out using accelerated optical stresses with the purpose to extract a degradation law as a function of accelerated parameter and to understand which is the mechanisms involved in the degradation. The responsible of the degradation during illumination stresses is the formation of defects and chemical species at TiO_2/sensitizer/electrolyte interface which reduces the charge transfer at interface and the ion migration across electrolyte.

5.1.2 Results

Figs. 5.1-5.11summarize the results of the illumination stress. Figs. 5.1 and 5.2 show the degradation of V_{OC} and J_{SC} of a cell stressed at 15 Sun. For comparison, we show the evolution of V_{OC} and J_{SC} of one of the two neighboring cells, which can be

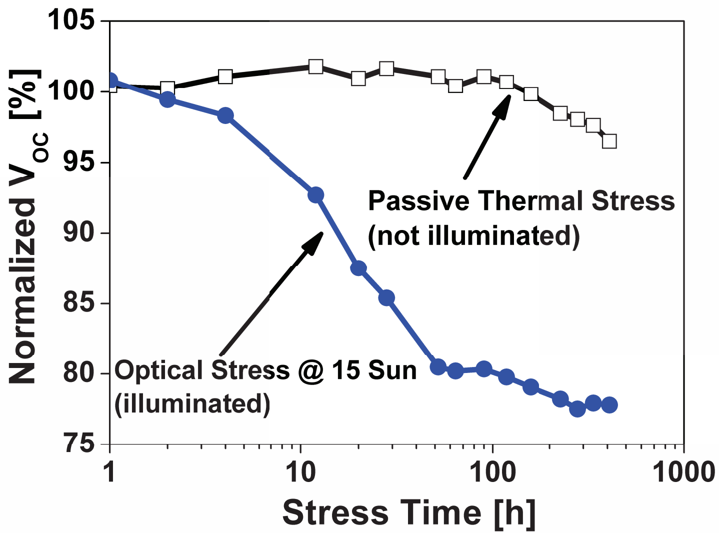

FIGURE 5.1: Trends of the open circuit voltage of two neighboring cells, one subjected to direct optical stress and the other subjected to passive optical and thermal stress. The graph of the open circuit voltage of the passive cell does not change abruptly during the optical stress of the other cell.

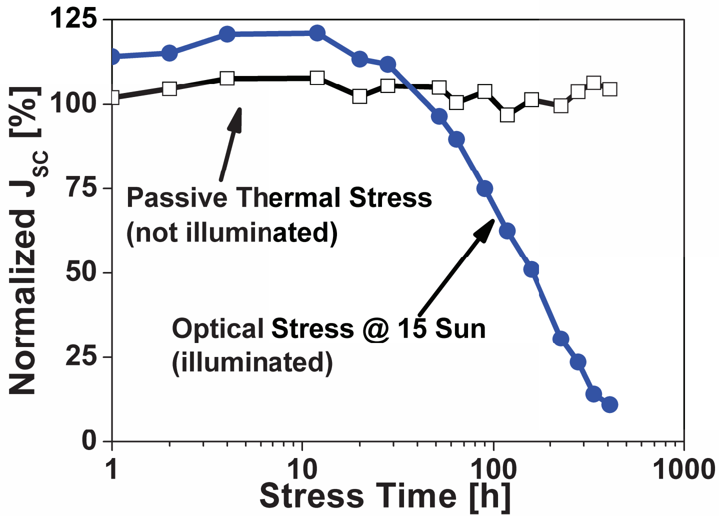

FIGURE 5.2: Trends of the the short circuit current of two neighboring cells, one subjected to direct optical stress and the other subjected to passive optical and thermal stress.

subjected to a parasitic thermal stress due to the glass heating (see curve marked as ”‘Parasitic Thermal Stress”’ in Figs. 5.1-5.2). The neighboring cells show very moderate degradation indicating that the evolution of the illuminated cell is dominated by the effects of light.

Figs. 5.3, 5.4, and 5.5 shows the current density-voltage (J-V), the power-voltage (P-V) and the EIS characteristics during stress. The reported characteristics refer to the device stressed at 15 Sun. The devices stressed at 8, 10, and 12 Sun feature a similar

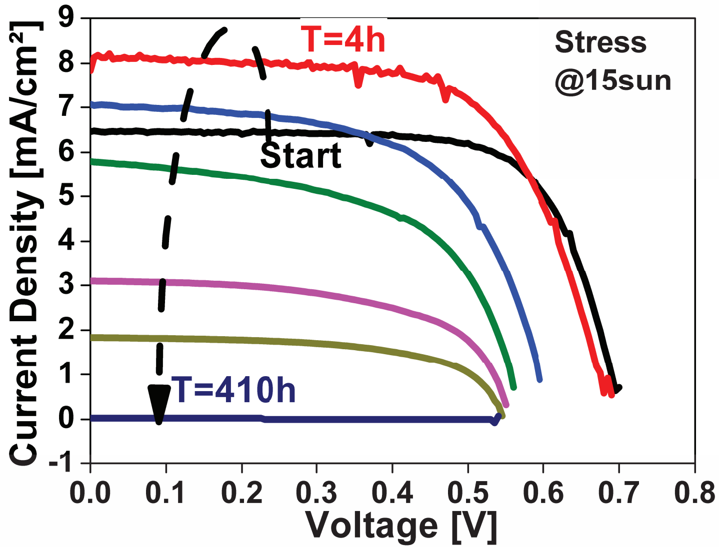

FIGURE 5.3: Degradation of the current density-voltage characteristic of a DSC illuminated at 15 Sun during stress. Measure have been taken under illumination at 1 Sun.

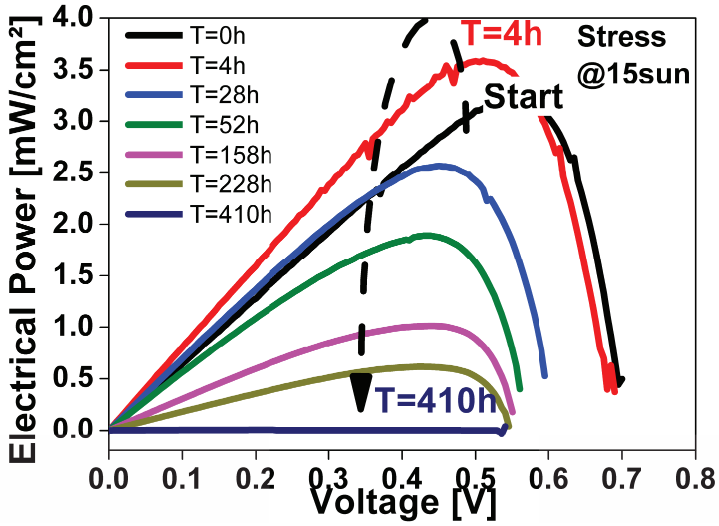

FIGURE 5.4: Degradation of the output power-voltage characteristics of a DSC illuminated at 15 Sun during stress. Measure have been taken under illumination at 1 Sun.

behavior.

Figs. 5.6, 5.7, and 5.8 show the evolution of V_{OC} , J_{SC} , and efficiency as function of the stress time for different illumination level (8, 10, 12, and 15 Sun, respectively). Similarly, Figs. 5.9, 5.10, and 5.11 show the same two parameters as a function of the cumulative irradiated energy.

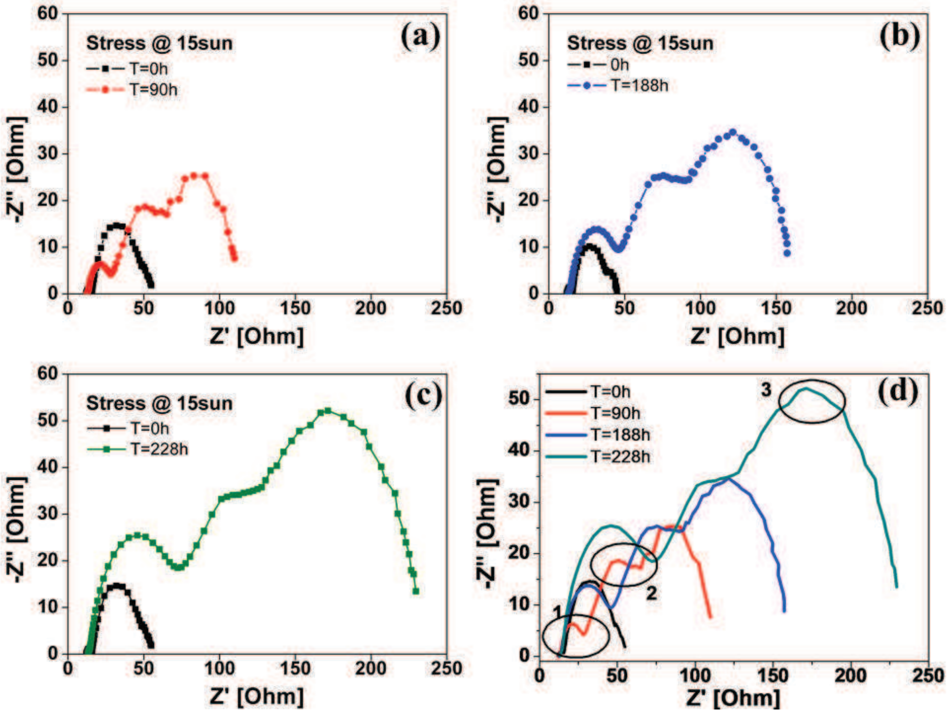

FIGURE 5.5: Degradation of the electrochemical impedance spectroscopic analysis (EIS) characteristics of a DSC illuminated at 15Sun during stress. Measure have been taken under illumination at 1 Sun.

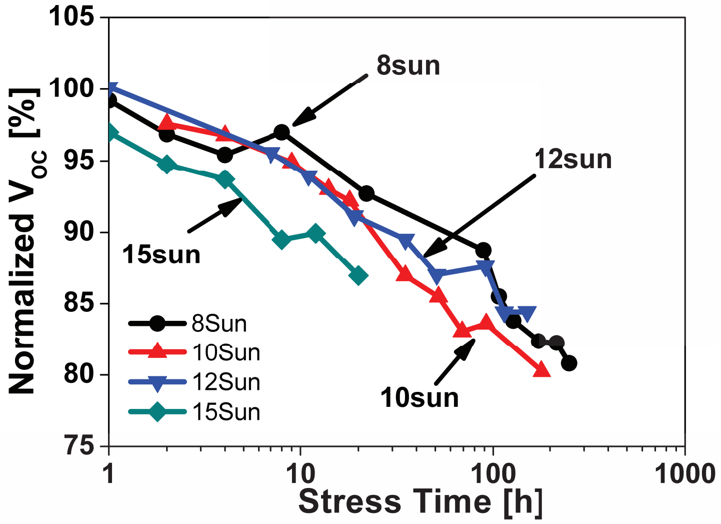

FIGURE 5.6: Evolution of V_{OC} as a function of stress time of four cells illuminated at 8, 10, 12, and 15 Sun.

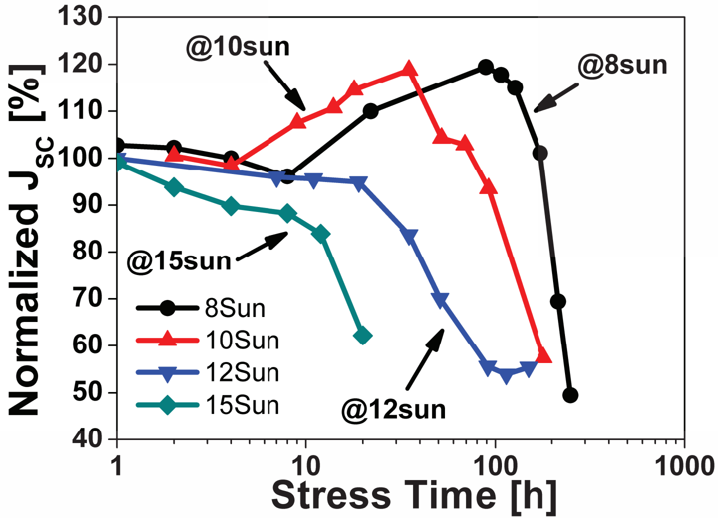

FIGURE 5.7: Evolution of J_{SC} as a function of stress time for four cells illuminated at 8, 10, 12, and 15 Sun.

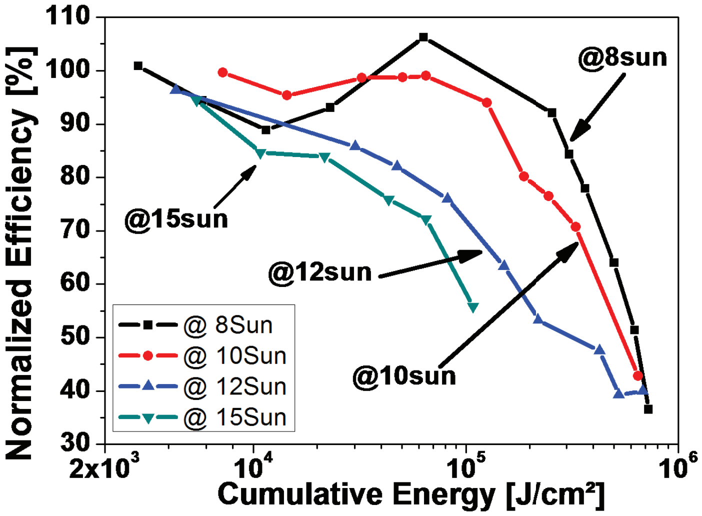

FIGURE 5.8: Evolution of efficiency as a function of stress time for four cells illuminated at 8, 10, 12, and 15 Sun.

5.1.3 Discussion

Our results clearly show that the cells subjected to direct illumination stresses feature: 1) a small decrease of the open-circuit voltage; 2) a very strong reduction of the short-circuit current; 3) a strong reduction of the maximum output power; and 4) an enlargement of the EIS curve.

First of all the strong degradation of the cell characteristics is a consequence of light exposure. In fact, by comparing the open and filled symbol in figures 5.1 and 5.2, we observe a 20% degradation of V_{OC} and almost complete collapse of J_{SC} after 400-hours stress at 15 Sun. In contrast the not illuminated devices show only the 4% variation of V_{OC} and only marginal variation of J_{SC} . This degradation may be due to either

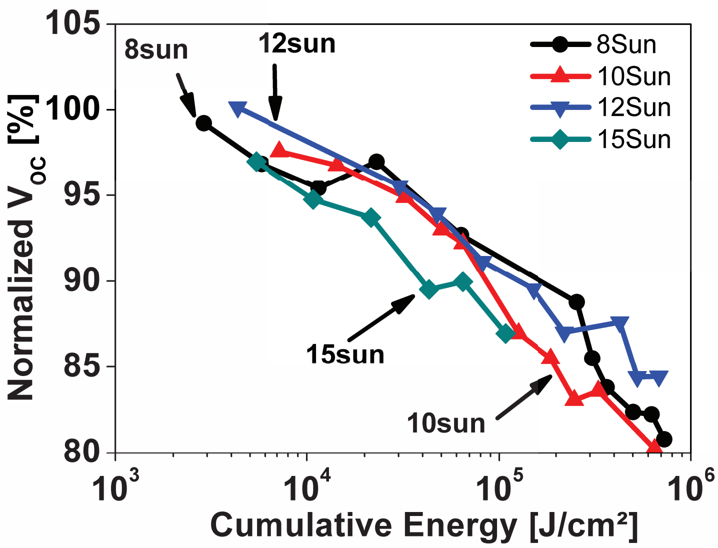

FIGURE 5.9: Evolution of V_{OC} as a function of the total cumulative energy irradiated during stress for four cells illuminated at 8, 10, 12, and 15 Sun.

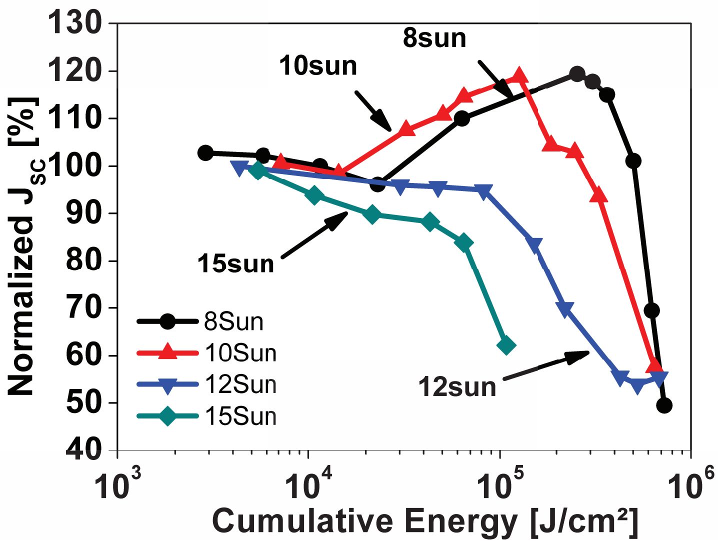

FIGURE 5.10: Evolution of J_{SC} as a function of the total cumulative energy irradiated during stress for four cells illuminated at 8, 10, 12, and 15 Sun.

parasitic illumination or thermal stress. As described above, the active area of the solar cell is sandwiched between two glasses. In principle, even if the not-illuminated solar cells are masked, the glass can act as light guide and some of the incident light can reach the masked cells. To quantify how much light travels inside the glass and reaches the active area, we have performed characterization measurements at 1 Sun, illuminating one cell and measuring the shaded ones. We have observed that the value of V_{OC} is about three times lower than the one measured illuminating directly the cell, while the value of J_{SC} is about one thousand time lower. Hence, we concluded that this parasitic optical stress only marginally impact on the degradation of the shaded cells. This is confirmed by the measurements performed on the shaded cells, as shown in Figs. 5.1-5.2. The

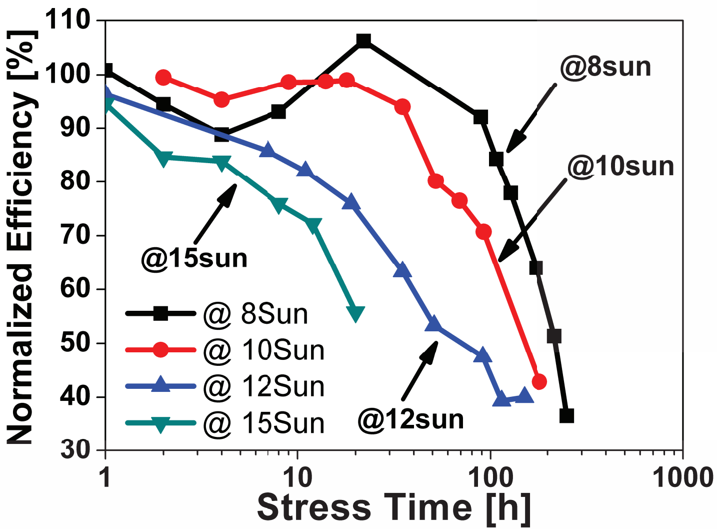

Figure 5.11: Evolution of efficiency as a function of the total cumulative energy irradiated during stress for four cells illuminated at 8, 10, 12, and 15 Sun.

following discussion is split in two parts. In the first part we discuss the degradation of DC parameters under illumination while in the second one we draw some hypotheses on the nature of damage by analyzing the shape of EIS during illumination stress.

Degradation of the cell characteristics

From the DC measurements we can draw some considerations. The V_{OC} and J_{SC} degradation kinetics are very different: V_{OC} is monotonically and almost linearly decreasing in the logarithmic-scale time of Fig. 5.6 independently by the optical intensity. Conversely, J_{SC} kinetics features a different behavior: at the beginning of the stress, J_{SC} has an almost constant or even increasing evolution, but after some hours it features a turn around and it starts quickly decreasing. The duration of the initial constant/increasing trend depends on the applied illumination intensity. In fact, the turn around is more pronounced at illumination intensities of 8-10 Sun than for 12-15 Sun as shown in Fig. 5.7. We can figure that the turn around is always present independent on the illumination intensity, but it runs out within the first steps of stresses at 12-15 Sun. From the V_{OC} -Time (Fig. 5.6), J_{SC} -Time (Fig. 5.7) and efficiency-time curves (Fig. 5.8), we note that the degradation rate increases as the optical power increases. For instance, the device illuminated at 8 Sun exhibits a 20% efficiency drop after 150-h illumination. Conversely, if the illumination level is increased at 15 Sun (i.e. almost the double), the 20% degradation is reached only after a 6-h stress, i.e., 25 times earlier. This acceleration of the efficiency degradation mainly derives from the reduction of the J_{SC} current. In fact, Fig. 5.6 shows that V_{OC} is much less affected by the illumination condition than J_{SC} .

If we plot the degradation of V_{OC} , J_{SC} , and efficiency as a function of the total cumulative irradiated energy, as shown in Figs. 5.9, 5.10, and 5.11, the large difference between the degradation kinetics at 8 Sun and 15 Sun reduces, but it is still present. We arbitrarily defined a critical value of the cumulative irradiated energy E_C as the energy required to achieve a 20% reduction of a given cell parameters (V_{OC} , J_{SC} , and efficiency). In Fig. 5.12 we reported the reference level of 80% for efficiency.

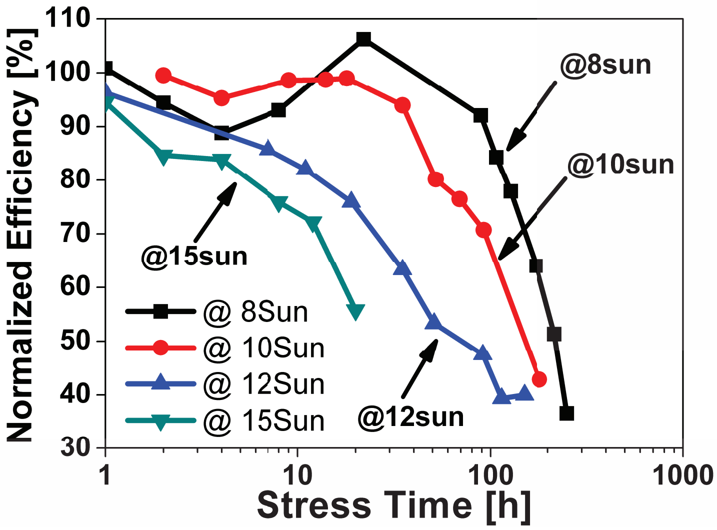

Figure 5.12: Evolution efficiency as a function of the total cumulative energy irradiated during stress for four cells illuminated at 8, 10, 12, and 15 Sun. In the picture is represented the reference at 80% of efficiency. Where the reference line cross the efficiency curve, it is exposure time required to have a 20% efficiency reduction under a specific magnitude of illumination intensity.

In Fig. 5.13 we plot E_C as a function of the optical irradiating power during stress. For

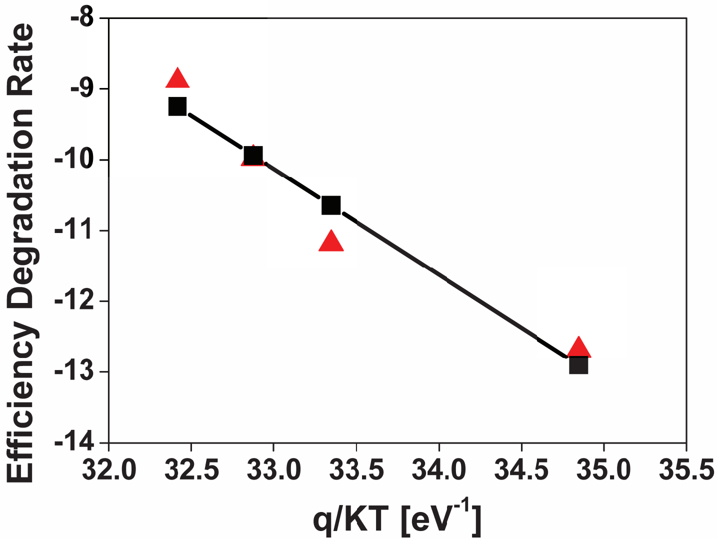

Figure 5.13: Evolution of E_C as a function of the illumination intensity.

all parameters, E_C strongly reduces with increasing irradiation intensity, from 8 Sun to 15 Sun. Assuming an exponential relation between E_C and the illumination intensity, we estimated $E_C = 4 \text{ x } 10^6$ J/cm^2 at 1 Sun, corresponding to 46 days. Such exponential relation suggests that at very high illumination levels some additional degradation phenomena occur. This accelerating factor might be strongly correlated to the increase of the interface temperature induced by the high illumination power. Of course this extrapolation has been done by assuming that the degradation rate maintains the same trend also at low illumination intensity.

Analysis of cell degradation by EIS measurements

In principle, the reduction of the J_{SC} could be a signature of an artificial sintering of the TiO_2during the illumination exposition, which is more effective at higher illumination intensities (i.e. 12-15 Sun). In fact, the artificial sintering of the TiO_2should reduce the effective surface area and, in turn, the short circuit current. However, the TiO_2sintering requires very high temperature around 500°C. At 15 Sun we measured the glass temperature of about 50°C. Taking in account the typical thermal resistance of glass, this temperature level is not enough to sinterize the TiO_2particles. Moreover, at such high temperature the sealing degradation the electrolyte evaporation are much more likely to occur.

Another hypothesis is the formation of defects at the TiO_2/sensitizer/electrolyte interface. Such defects may come from the incomplete regeneration of dye molecules by the electrolyte or the formation of weak/dangling/strained bonds between the sensitizer and the electrolyte. The formation of new species is likely activated by temperature, and then, by illumination intensity. In both cases the dye could not be able to generate electron/hole couple when hit by the sunlight and then reducing the short circuit current.

The EIS measurements in Fig. 5.5 give us further information on the most likely mechanism involved in the cell degradation. There is a clear enlargement of the EIS plot during stress, even though the Nyquist diagram keeps the same shape from the beginning to the end of the stress, featuring the three semicircles typical of DSC [71]. In fact, the three semicircles are always present, but they feature a very different evolution. The second semicircle, which is correlated to the electron transfer at the TiO_2/electrolyte interface [71], shows an appreciable variation. This confirms the presence of defects at the TiO_2/sensitizer/electrolyte, as discussed above. However, the third semicircle (see picture (d) in Fig. 5.5 marked with 3) shows the biggest enlargement. This is correlated with the Nernst diffusion in the electrolyte [71]. This indicates that any chemical reaction due to thermal or illumination stress generates not only defects at the TiO_2/electrolyte interface, but also some chemical species within the electrolyte, which may hamper the ion diffusion across the electrolyte.

5.2 Pure thermal accelerated stresses

5.2.1 Introduction

With pure thermal stresses, we have studied the role of temperature on the degradation of DSC. We performed pure thermal stresses keeping the devices at a constant temperature inside a climatic chamber and monitoring the electrical parameters during stress. We found that temperature alone strongly impacts on the DSC performances, enhancing the degradation of the sensitizer and then reducing the photo-generated current.

5.2.2 Results

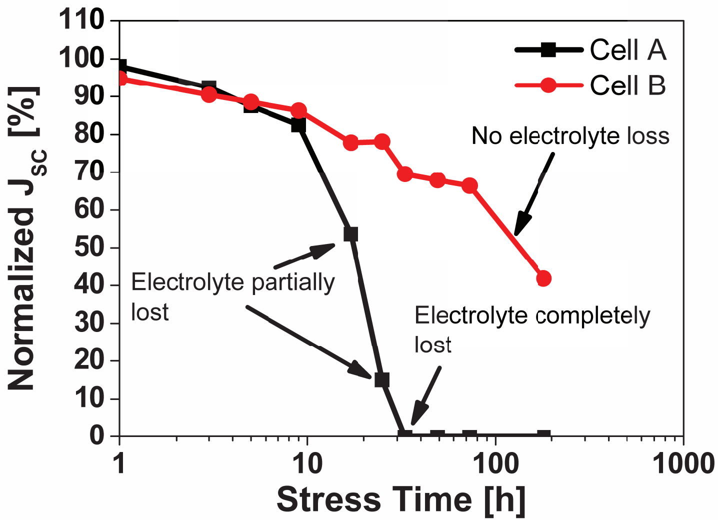

FIGURE 5.14: Evolution of the normalized J_{SC} of a device that has experienced a completely loss of the electrolyte (cell A) and a device with an intact electrolyte (cell B).

Figs. 5.14-5.23 show the data collected during thermal stress. Fig. 5.14 shows the kinetics degradation of J_{SC} for two cells, marked with A and B, thermally stressed at 70°C. The two cells exhibit two different behavior during thermal stresses. Cell B show a progressive and smooth degradation of the J_{SC} , while cell A feature a very sudden drop after some tens hours of thermal storage, due to the electrolyte loss, as will be discussed in the next section. Fig. 5.15 shows a couple of picture referring to the cell A before and after stress. Fig. 5.16 and 5.17 shows the current density-voltage (J-V) and the power density-voltage (P-V) characteristics of a device stored at a temperature

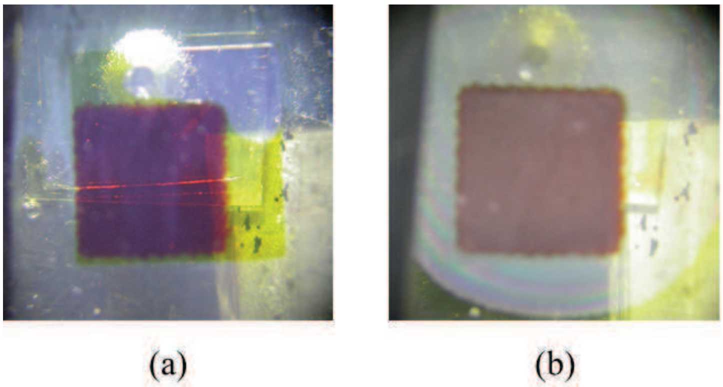

FIGURE 5.15: Two magnifications of the active area of a cell subjected to thermal storage: a) fresh; b) after 50-h stress.

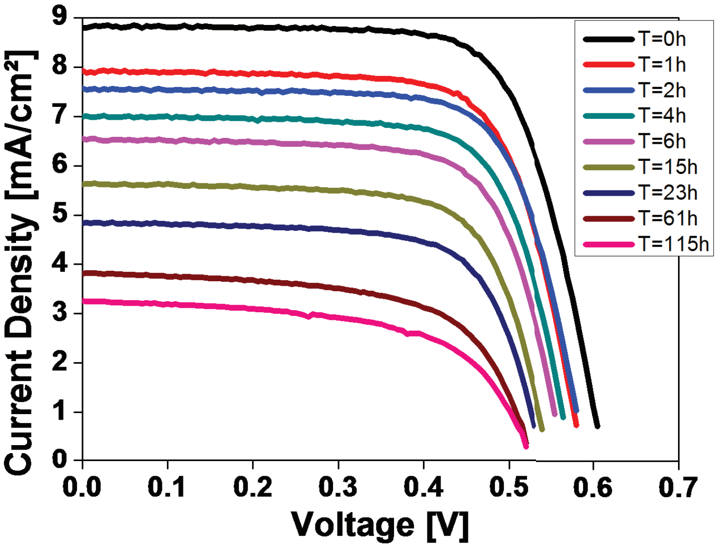

FIGURE 5.16: J-V curves for a cell stressed at 85°C storage temperature.

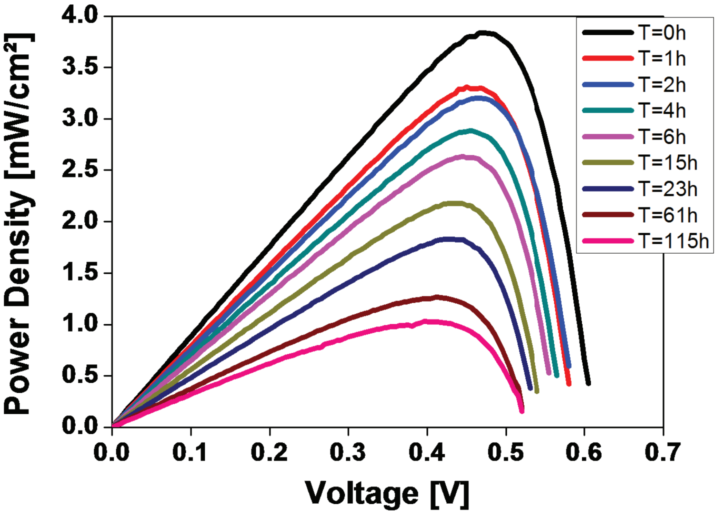

FIGURE 5.17: P-V curves for a cell stressed at 85°C storage temperature.

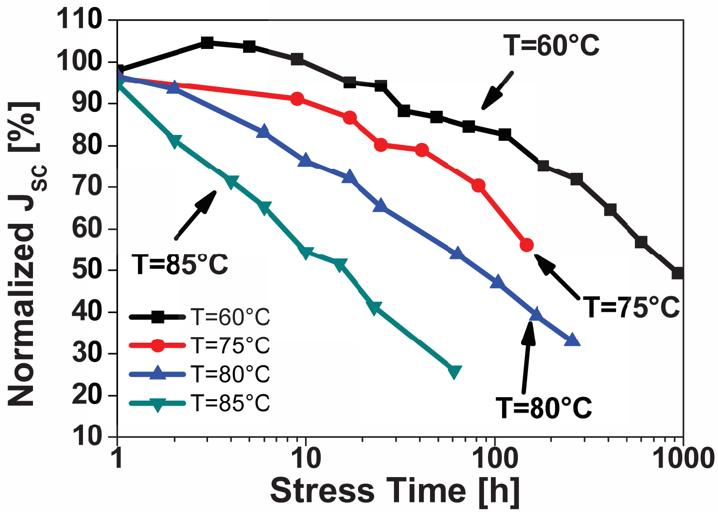

FIGURE 5.18: Evolution of short-circuit current vs. time.

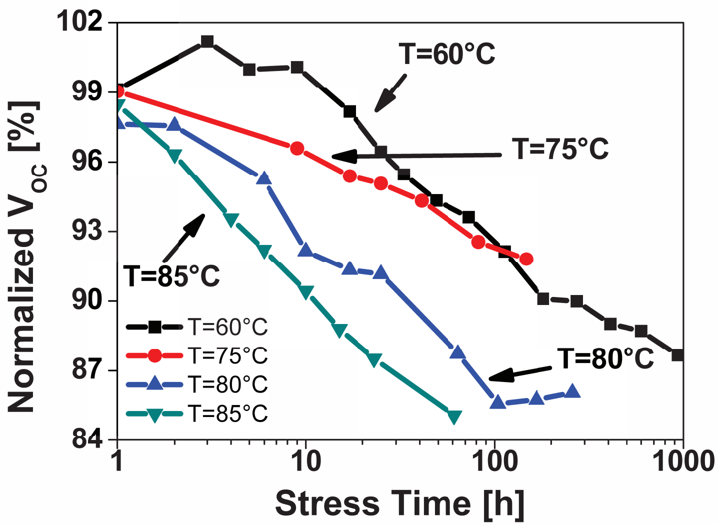

FIGURE 5.19: Evolution of open-circuit voltage vs. time.

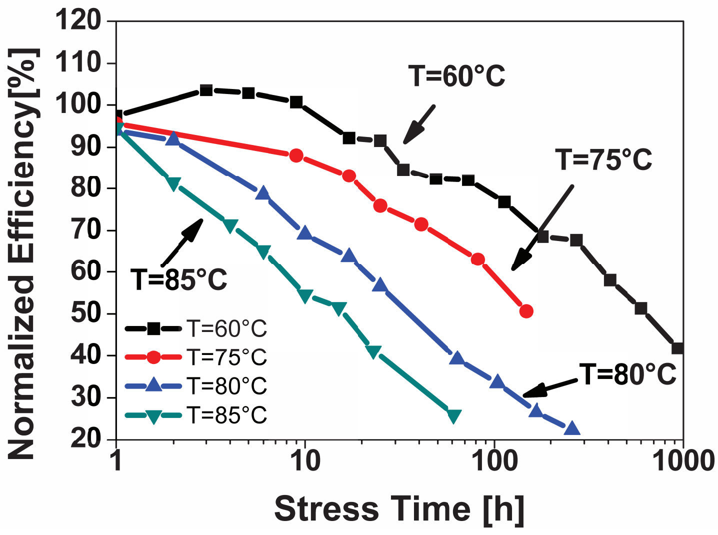

FIGURE 5.20: Evolution of the efficiency vs. time.

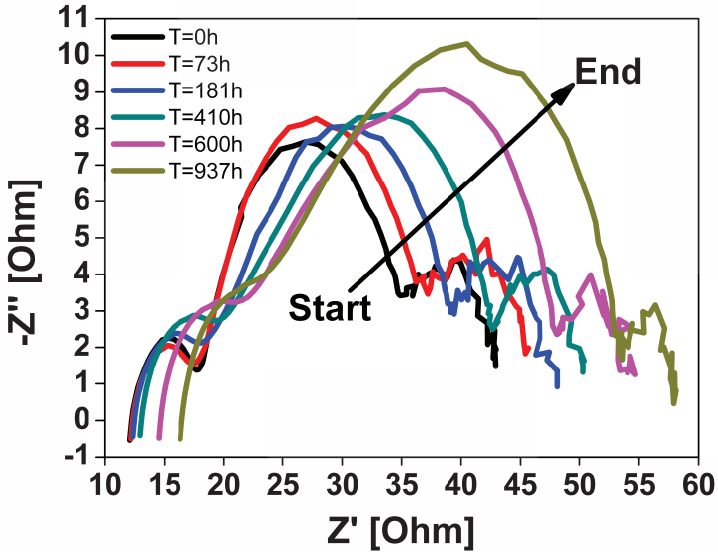

FIGURE 5.21: EIS diagram for three different devices subjected to a storage temperature of 60 C.

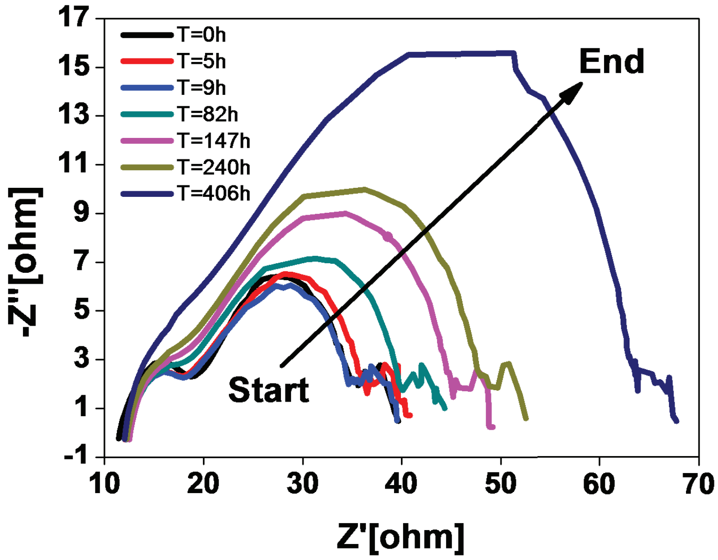

FIGURE 5.22: EIS diagram for three different devices subjected to a storage temperature of 75°C.

of 85°C. Fig.5.18-5.20 shows the degradation of the electrical parameters J_{SC} , V_{OC} , and efficiency as function of time of one of three cells contained on its substrates stored at four different temperatures. Fig. 5.21-5.23 shows the EIS characteristics: the three pictures (a-c) refer to three different storage temperature stresses, 60°C, 75°C, and 85 respectively. Fig. 5.24 shows the Arrhenius plot of the normalized efficiency degradation rate. In short, we observed that a leak of the electrolyte during stress strongly impact on the degradation kinetics of DC parameters and on the life-time of the cell. In fact, a fail of the cell can appear after a completely loss of the electrolyte. However, if the sealing preserves the electrolyte during stress, we observed:

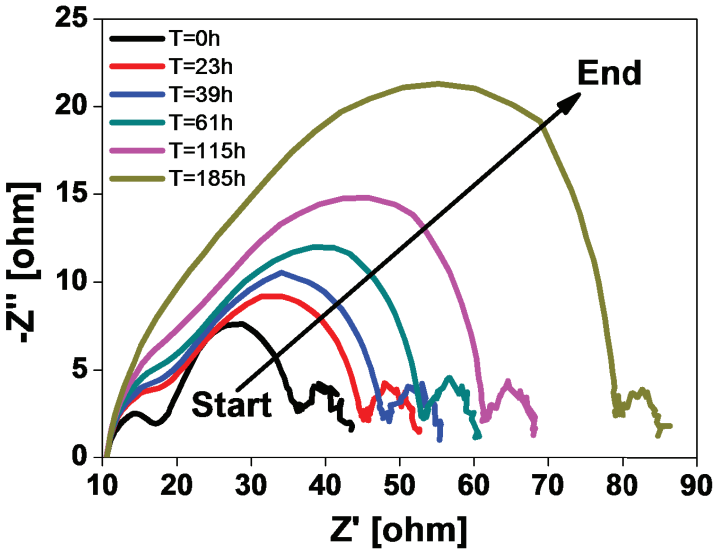

Figure 5.23: EIS diagram for three different devices subjected to a storage temperature of 85°C.

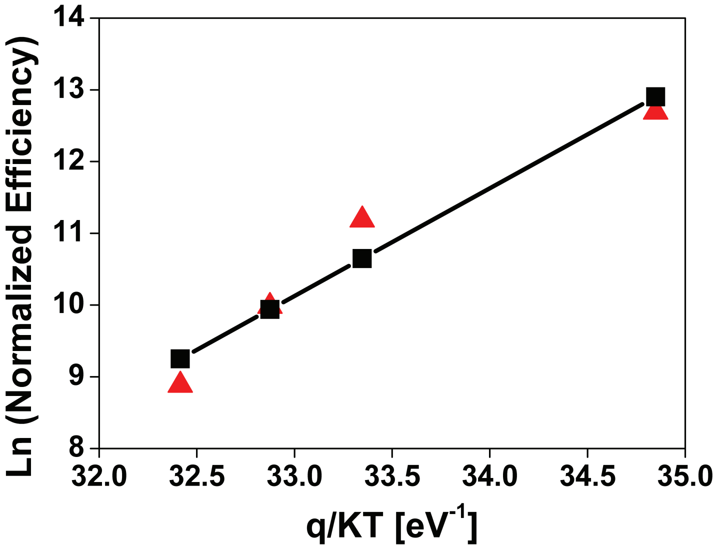

Figure 5.24: Temperature dependence of the efficiency degradation rate during storage at constant temperature.

1. a negligible variation of the DC parameters and the I-V curves of the reference devices at least for a time as long as the duration of the thermal stresses;
2. a small reduction of the open-circuit voltage V_{OC} , which drops below the 90% of its original value at the end of the thermal stress;
3. a decrease of the short-circuit current, which is much stronger than the V_{OC} . For instance, in Fig. 5.18, J_{SC} reduces to the 25% of its original value after less than 100-h storage at 85°C;

4. a strong reduction of the maximum output power, mostly ascribed to the degradation of the short-circuit current;
5. the enlargement of EIS with only marginal variation in shape.

5.2.3 Discussion

Fig. 5.14 shows that different degradation mechanism can occur during thermal stresses. After 20-h stress, cell A (squared-line in Fig. 5.14) shows an abrupt reduction of the short-circuit current and consequently a strong decrease of the efficiency while cell B (circle-line in Fig. 5.14) does not features the same abruptly variation. Figs. 5.15 (a and b) show two pictures of cell A taken performance in terms of V_{OC} , J_{SC} and efficiency. However, we cannot exclude that thermal storage could damage an intact sealing allowing the electrolyte to leak for much longer time, especially at high temperatures. In the following, we will focus our analysis only on those cells where the integrity of the sealing is not compromised by thermal stress and no appreciable electrolyte loss is clearly visible at the beginning of stress.

Observing the data collected in Fig. 5.16-5.20, some remarks are worth to be drawn. From the J-V curves shown in Fig. 5.16, we can point out a reduction of the short-circuit current and the open-circuit voltage as well, while the shape appears to be the same almost on the entire stress time. The electrical power decreases monotonically during stress, as we can observe from the P-V curves pictured in Fig. 5.17. From the three plots depicted in Fig. 5.18-5.20, we can draw some considerations. Firstly, as the time stress increases the V_{OC} , J_{SC} , and efficiency decrease monotonically as the storage time increases and this is more evident at higher temperature. At lower temperature, i.e. 60°C, open-circuit voltage and short-circuit current remain almost flat at the beginning of storage and this can explain the increase of efficiency within the first 10-h of stress. We suppose that the initial increase of efficiency can be ascribed to a thermal-induced annealing, which can improve the overall performance. This can occur, for instance, by recovering and/or rearranging some dangling or strained bonds between the dye and the TiO_2or within the dye molecules. We can exclude any annealing/sintering of the TiO_2nanoparticles at such low temperatures, in fact he TiO_2nanoparticles are sintered at 500°C. Secondly, V_{OC} , J_{SC} , and efficiency degradation rate increases as the storage temperature increases. For instance, the device storage at 60°C exhibits a 20%-degradation of its efficiency after 50-h while the devices stored at 80°C and 85°C exhibit the same degradation after about 10-h and 1-h respectively. This acceleration is mainly due to a strong degradation of the J_{SC} current: in fact, by comparing Figs. 5.18

and 5.19, J_{SC} decreases faster than V_{OC} as the storage temperature increases.

Figs. 5.21-5.23 show the Nyquist diagram of three devices stressed at three different temperatures. As the storage time increases the EIS plot becomes larger. Even though the plot enlarges during stress, the EIS curve always maintains its typical shape featuring the three semicircles, even though in some cases the first semicircle is not clearly visible, such as in the curve taken after 185-hour storage at 85°C (see Fig. 5.23) [71]. Despite the shape is preserved during stress, the three semicircles feature very different evolutions. The first semicircle, which is a measure of the reduction of the electrolyte at the counter-electrode, shows only marginal variation independent on the storage temperature. Similarly the third semicircle, correlated to the Nernst diffusion across the electrolyte, it does not change in size, but it just shift rightward. Instead, the second semicircle shows the most remarkable variations, becoming larger and larger as the storage time increases. This enlargement is faster as the storage temperature increases. For instance the growth of the second semicircle at 85°C is such that it overwhelms the first semicircle after 185-h storage. Referring to the peak of the semicircle, we may note that after approximately 180-h storage, the peak has marginally changed if the devices are stored at 60°C. Conversely, if the cells are stored at 75°C, the EIS peak almost doubles its original value. At 85°C the EIS exhibits a threefold increase in value (from 7Ω to 21Ω).

This variation can be ascribed to the degradation of the TiO_2/Dye/Electrolyte interface [74]. The temperature may enhance the formation of new species at the TiO_2interface or break bonds on the dye molecules and allow the dye to dissolve into the ionic solution.

This can also be correlated to the strong reduction of J_{SC} shown in Fig. 5.18a: in fact, if some molecules are damaged they are not able to generate charge when illuminated. From the Arrhenius plot of Fig. 5.24 we estimated a value of activation energy equal to 1.5eV. This value is compatible with the activation energy associated with the hydrogen and –OH groups.

5.2.4 Comparison between pure thermal and AM1.5 illumination stresses

It is worth to compare the degradation kinetics measured during thermal and illumination stresses (see Fig. 5.25). The sample illuminated at 15 Sun reaches a 20% degradation of J_{SC} after 10-hours stress. The same degradation is observed after 10-hours

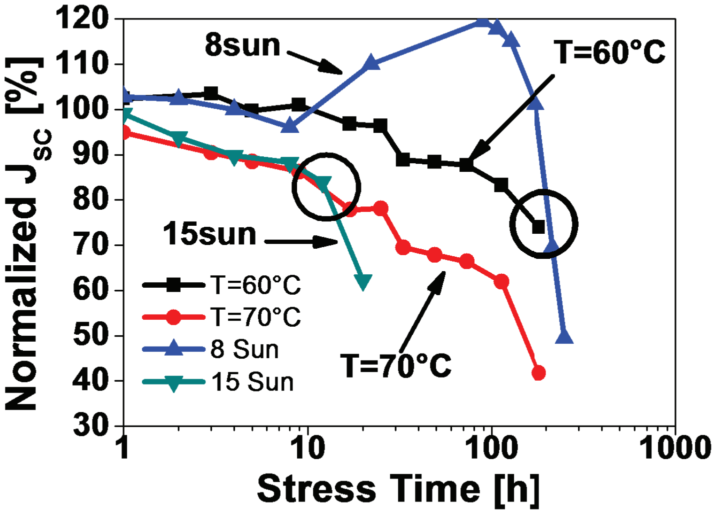

FIGURE 5.25: Comparison between the J_{SC} evolution as a function of stress time during two illumination stress at 8 and 15 Sun, and two thermal stress at 60°C and 70°C.

thermal stress at 70°C. Similarly, the device illuminated at 8 Sun exhibits a 20% drop after 200-hours which is almost the same drop observed after 200-hours at 60°C (see Fig. 5.25). These values are in agreement with the interface temperature during illumination stress. At first glance, we can argue that the self heating plays an important role during optical stress and that during illumination the interface temperature may range between 60-70°C, in agreement with the glass thermal resistance. However, the comparison of thermal and optical stress highlights a different shape of the curves plotted in Fig. 5.25, especially for the stress at 8 Sun. This indicates that besides heating, the degradation is driven by other mechanisms, which are worth of further investigations. Such mechanisms are likely correlated with the current flow. In fact, some preliminary illumination stresses performed at open circuit, i.e. with no current flow, have shown slower cell degradation.

5.3 Reliability Study of DSC by means of Solar Simulator and White LED

5.3.1 Introduction

A LED-based light source as an alternative to AM1.5 solar simulator to perform the reliability study on dye-sensitized solar cells. We performed accelerated optical stresses by means of high power white LED and during stress we performed DC and EIS measurements with both white LED and AM1.5 solar simulator in order to find, if any, differences in kinetics degradation. During stress we also performed characterization measurements using monochromatic LED sources in order to understand if it adds more information about the DSC degradation mechanism. We found that DC parameters feature different degradation rates depending on characterization source and differences also appear on degradation kinetics shape. The DSC characterization performed with monochromatic light sources show strong differences in degradation rate and in degradation kinetics shape as well depending on wavelength sources.

5.3.2 Results

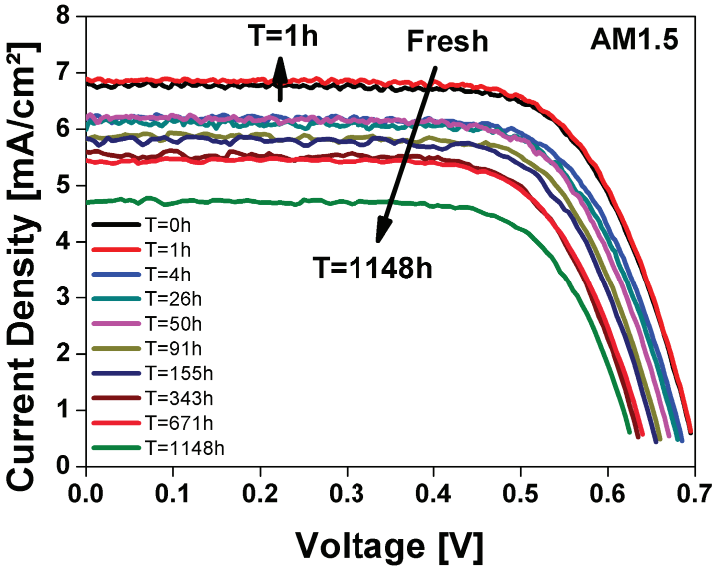

FIGURE 5.26: Evolution of: current-density vs. voltage measured by means of AM1.5 solar simulator.

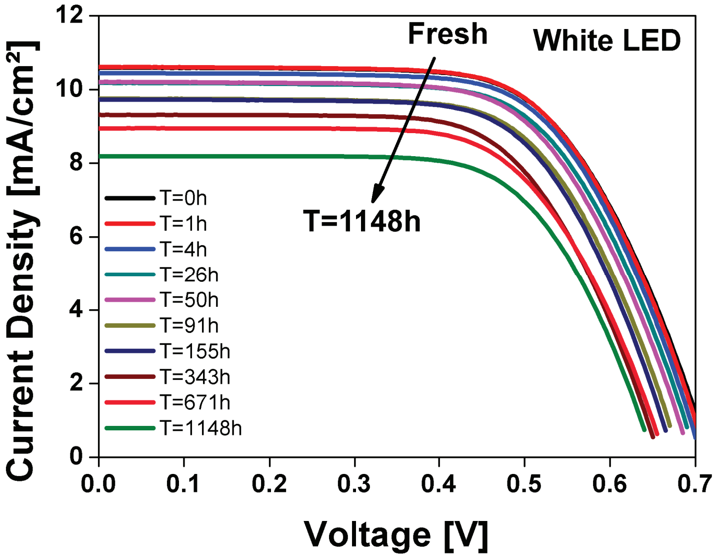

FIGURE 5.27: Evolution of: current-density vs. voltage measured by means of white-LED solar simulator.

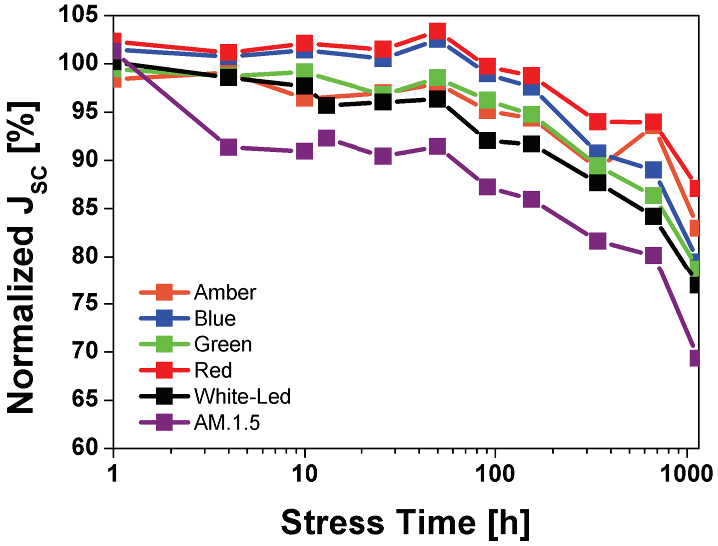

FIGURE 5.28: Evolution of: short-circuit current density vs. time.

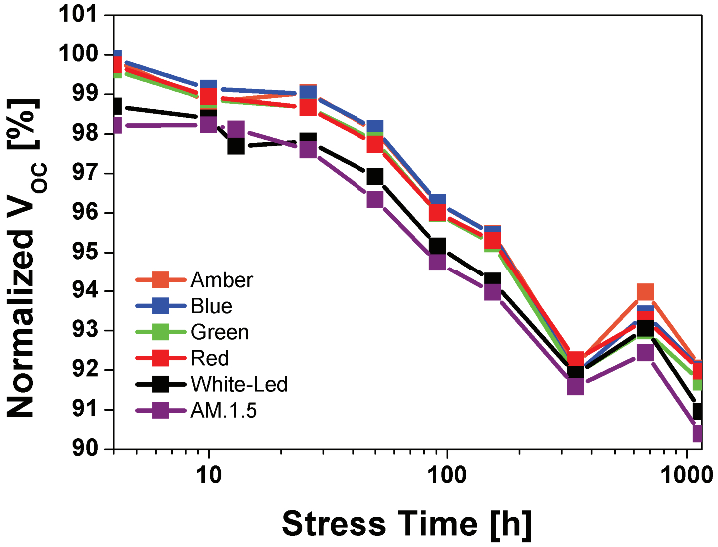

FIGURE 5.29: Evolution of: open-circuit voltage vs. time.

TABLE 5.1: DC parameters normalization table

Param	*AM1.5*	*White*	*R*	*G*	*B*	*A*
JSC (mA/cm^2)	6.8	10.6	9.1	9.2	8.9	8
VOC (mV)	708	720	718	715	712	711
Efficiency (%)	3.32	4.89	4.36	4.31	4.17	3.88

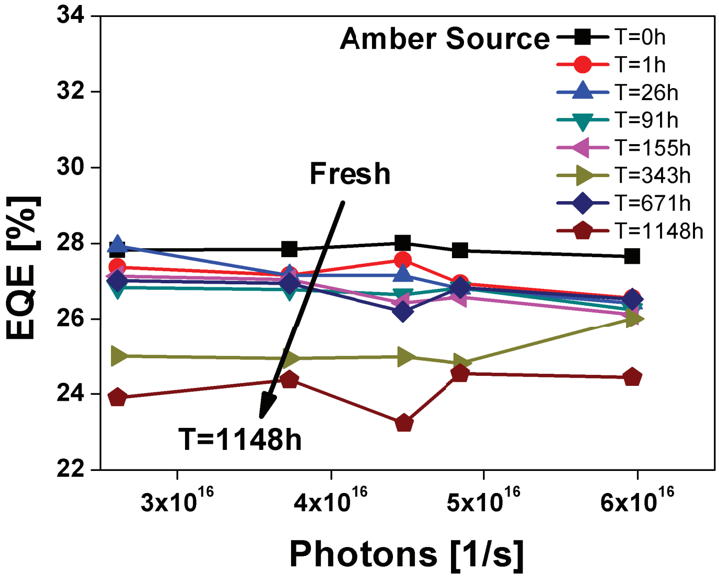

FIGURE 5.30: EQE evolution measured by amber light source.

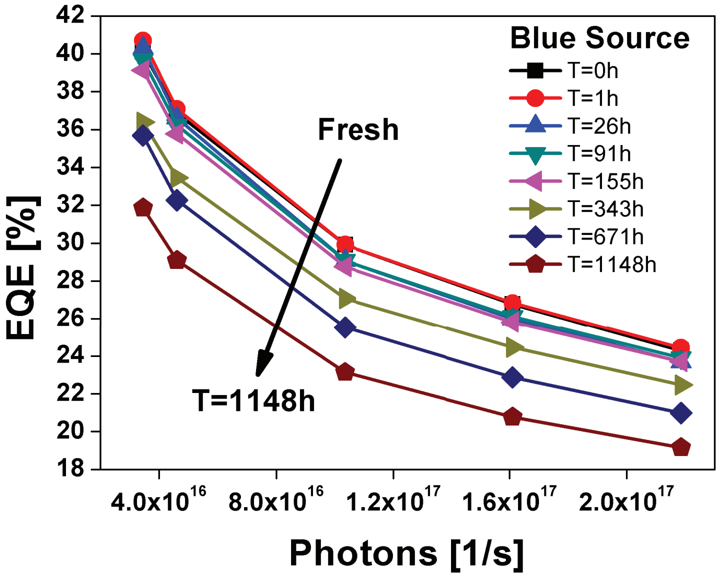

FIGURE 5.31: EQE evolution measured by blue light source.

Figs. 5.26-5.29 show the data collected during optical stresses. Figs. 5.26 and 5.27 show the current density-voltage (J-V) characteristic measured during stress by means of AM1.5 solar simulator and white LED respectively. Figs. 5.28-5.29 shows the degradation of the normalized electrical parameters J_{SC} , and V_{OC} as function of the stress time for all characterization light sources. The normalization has been done respected to the parameter values of the fresh device (see Tab. 5.1). As shown in Fig. 4.23 (in the previous chapter), the white-LED emission spectrum partially covers the absorption spectrum of the sensitizer, in fact the dye spectrum has a tail in the near-IR and it has an absorption coefficient which still roughly one in the near-UV (up to 350nm). Concerning the RGBA LED, the figure shows that dye material almost

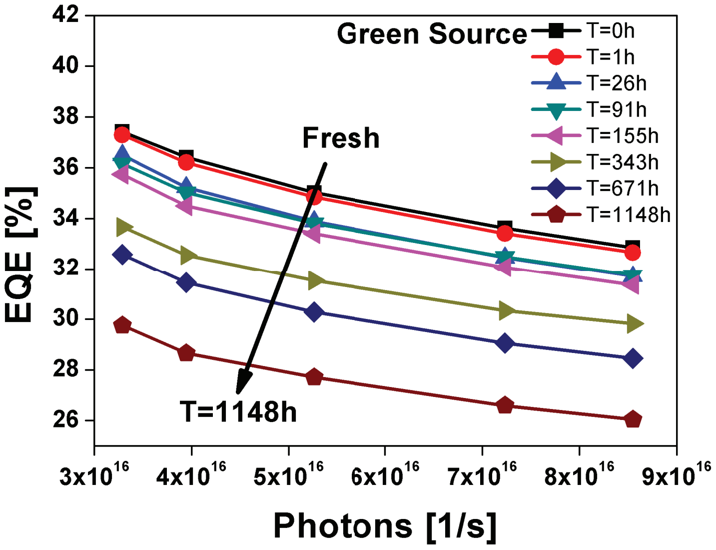

FIGURE 5.32: EQE evolution measured by green light source.

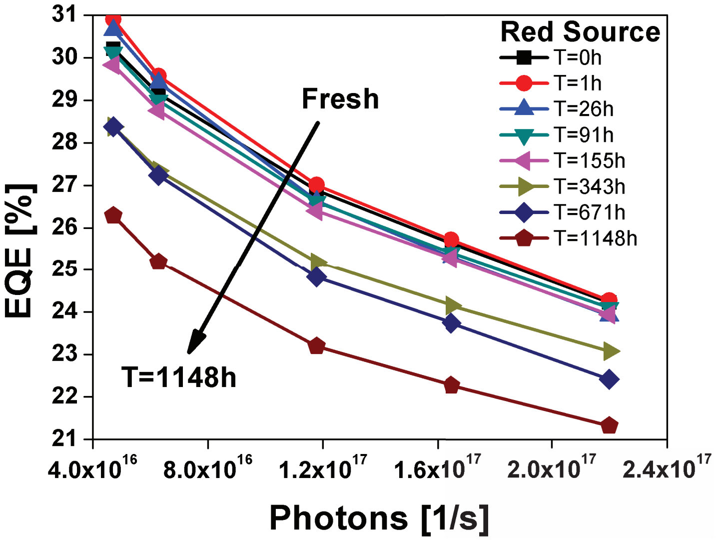

FIGURE 5.33: EQE evolution measured by red light source.

completely absorbs blue and green components (absorption coefficients are 0.989 for both sources), while it partially absorbs amber and red light (absorption coefficients are 0.823 and 0.609 respectively). Figs. 5.30-5.37 show the evolution during stress of the EQE and IQE respectively. Figs. 5.38 and 5.39 shows the EIS characteristics: Figs. 5.38-5.39 show the evolution of EIS plot measured by means of AM1.5 solar simulator and white LED respectively. In the next session the data collected during stress are discussed.

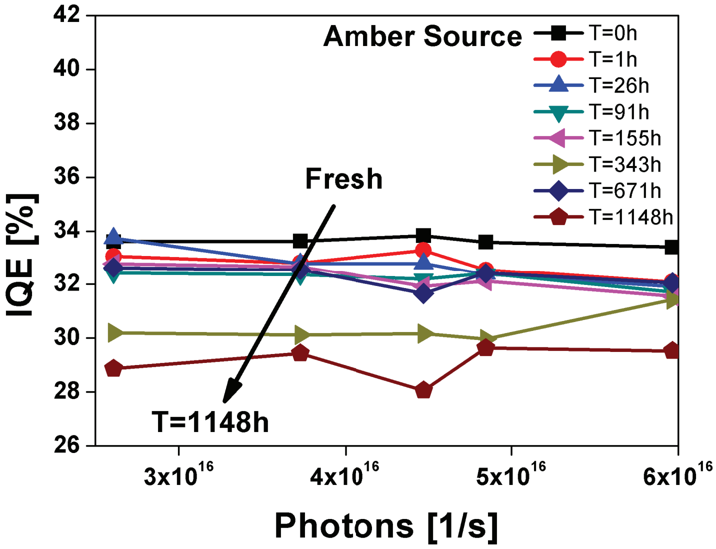

Figure 5.34: IQE evolution measured by amber light source.

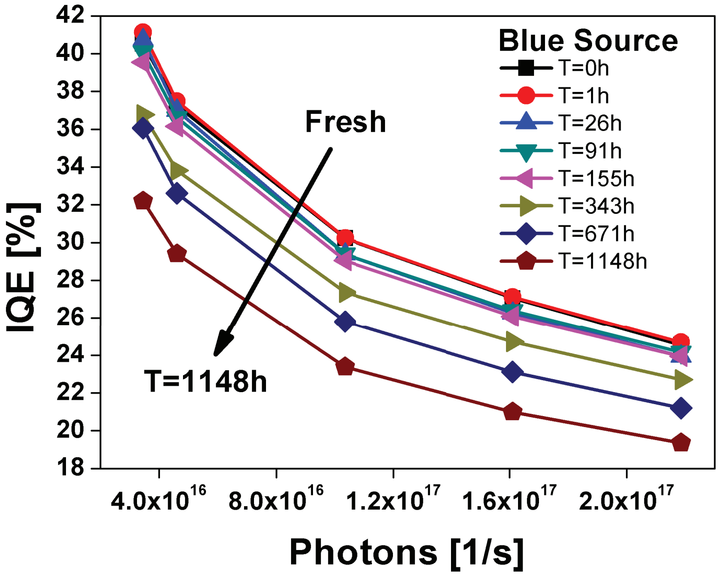

Figure 5.35: IQE evolution measured by blue light source.

5.3.3 Discussion

Observing the data collected in Figs. 5.26 and 5.29 we can draw some considerations. The J-V characteristics measured by means of white LED and AM 1.5 solar simulator show slightly different evolutions. They feature a global decrease of the performance of the cell, i.e. a J_{SC} decrease and a V_{OC} reduction. Both measurements do not feature a variation in shape during stress. In particular, the curves appear parallel near the short-circuit and the open-circuit regions. This indicates that no remarkable variation of the series resistance (R_S) and the shunt resistance (R_P) occurs during the entire stress at least with an optical stress intensity of 5 Sun. At the same cell bias condition, some

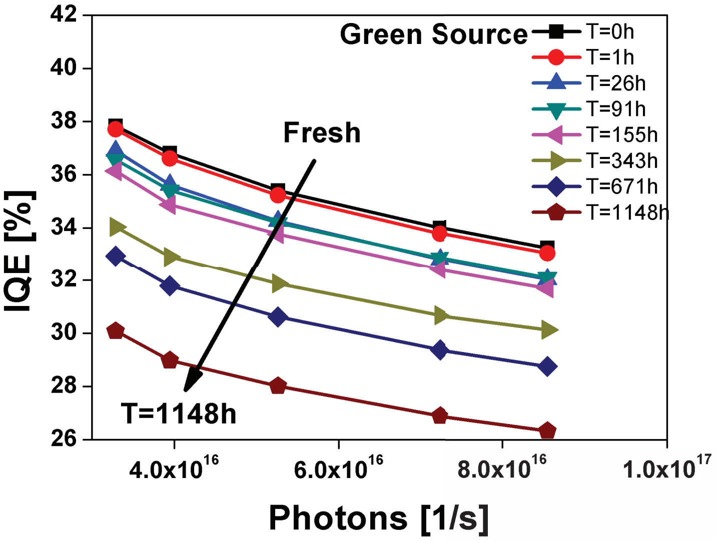

Figure 5.36: IQE evolution measured by green light source.

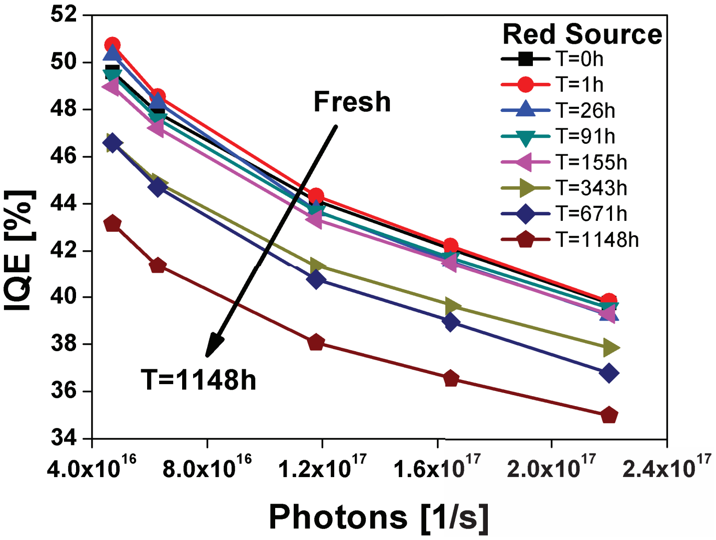

Figure 5.37: IQE evolution measured by red light source.

previous accelerated stresses carried out by means of AM 1.5 solar simulator have shown an increase of the J_{SC} at the beginning of stress, in particular for optical intensities ranging from 500mW/cm^2 and 1000mW/cm^2 (see section 5.1). During white LED stress, the J-V characteristics measured by means of AM 1.5 solar simulator show a slight increment of the J_{SC} within 1-h stress, while the J-V measured by means of white LED does not show the same initial increment. Two considerations are worth to be drawn. Firstly, the J_{SC} increment observed during AM 1.5 solar simulator stresses can be ascribed to an annealing phase, likely due to the wide presence of near-IR component in the solar simulator spectra, which might induce a moderate heating of cell materials. Since the IR component is not present in white LED spectrum (see Fig. 4.23 (in the

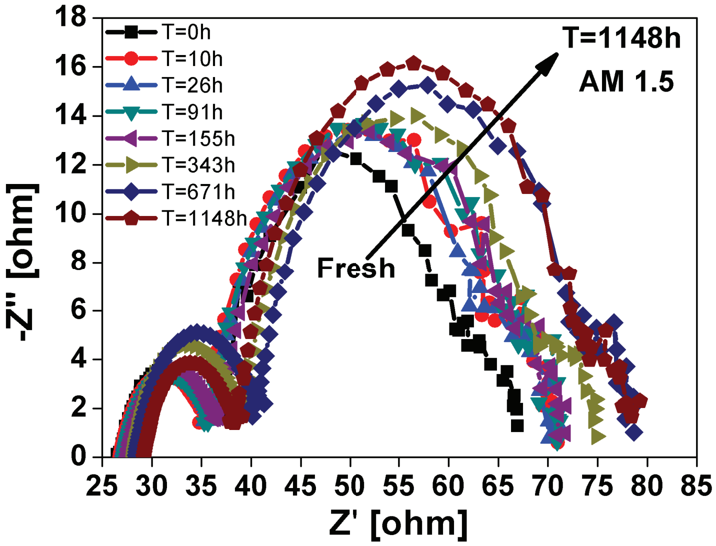

FIGURE 5.38: Evolution of EIS characteristics measured by means of AM1.5 solar simulator.

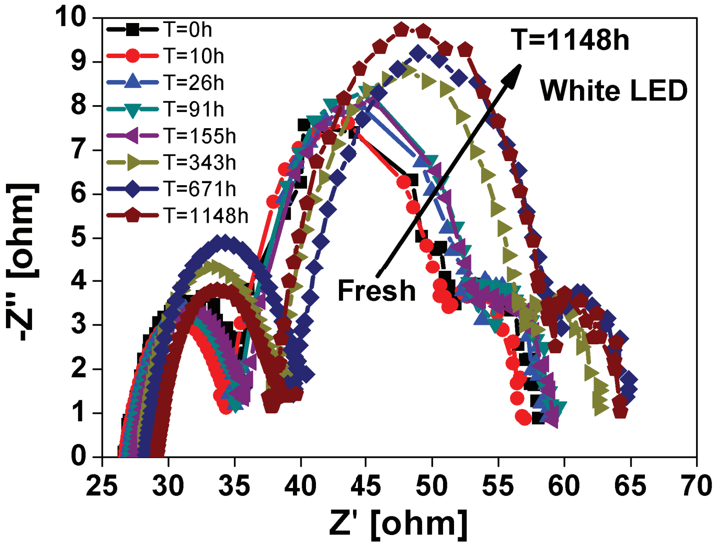

FIGURE 5.39: Evolution of EIS characteristics measured by means of White-LED solar simulator.

previous chapter)), no significant annealing can occur. The slight increase of J_{SC} observed during white LED stress, can be ascribed to self-heating due to a combination of light exposure and electrical conduction.

Secondly, even though the J_{SC} increment is marginal, the capability of AM 1.5 solar simulator to detect it, points out that white LED could not be able to show the complete kinetic degradation J-V characteristics, regardless of the stress source. From the J-V and Efficiency-V curves measured by means of RGBA LED, only green LED show J-V evolution similar to white LED. In fact, green light is a main component in white LEDs besides blue light. Efficiency-V curves show the same evolution of the J-V curves. Figs. 5.28-5.29 show the evolution of J_{SC} and V_{OC} for the six light sources employed.

Fig. 5.29 shows a monotonic decrease of V_{OC} as stress time increases, regardless of the characterization sources. White LED and AM 1.5 solar simulator light sources show similar degradation rate giving the same information on the degradation kinetic of V_{OC} during stress, at least with an optical stress intensity of 5 Sun. The degradation kinetic features almost the same shape for all light sources, but with different degradation rates. In fact, the characterization RGBA LED show a minor reduction of V_{OC} compared with the reduction observed with solar simulator and white led light sources. Fig. 5.28 shows the evolution of the J_{SC} during stress for all six characterization light sources. The J_{SC} kinetic measured by means of AM 1.5 solar simulator and white LED show a 10% and 2% drop of the J_{SC} respectively within 10 hours of stress. Ruthenium-based dyes absorb radiation ranging from 300-700nm and standard AM 1.5 solar simulator spectrum widely covers this wavelength range. Tentatively, we suppose that white light exposure combined with electrical conduction induces dye degradation and, in particular, making the dye no longer able to absorb wavelength in the near-UV (300-400nm). Since white LED partially covers the absorption spectrum of the dye (the range spectra of a white led ranges from 400 to 700nm, see Fig. 4.23 (in the previous chapter)), characterization by means of white LED cannot detect degradation that occurs outside of the white spectrum. J_{SC} kinetics measured by means of RGBA LED show different evolutions. Characterization with red and blue light sources show an initial increase J_{SC} within 50-h stress and then J_{SC} monotonically decreases; amber and green light characterization show a monotonic decrease of J_{SC} since the beginning of the stress. After about 1100-h of stress, J_{SC} measured with red, amber, blue, and green lights shows a drop 19%, 23%, 26%, and 27% respectively. We can conclude that different wavelength light sources give different information on the degradation kinetics of DC parameters (i.e. V_{OC} , J_{SC}) of a solar cell. We also found that degradation kinetics of fill factor and efficiency follows the same kinetics of J_{SC} .

Figs. 5.30-5.35 show the evolution during stress of the EQE and IQE of the cell measured by different wavelength of the light source, in particular amber, blues, green, and red colors. As shown in Fig. 4.23 (in the previous chapter), the dye material well absorbs light with a wavelength ranging from 400-550nm, while it partially absorbs wavelength greater than 550nm. Referring to the fresh curves in Figs. 5.30-5.33 (black line) and to a fixed photons rate, i.e. 5 x 10^{16} photons/s, EQE is higher for blue and green light (about 36% for both light) than for amber and red light (28% and 30% respectively). As comparison, in Figs. 5.34-5.37is reported the IQE of the cell measured with all colors. Even if the dye absorption coefficient for red light is lower than green and blue light, the IQE is higher for red light than blue and green light. This fact allows us to suppose that the extraction mechanism is more efficient for electron/hole pair photo-generated by red light than by blue or green light. At present, we are still investigating these phenomena.

The evolutions during stress of the quantum efficiencies vs. incident photon rates characteristics depend on the characterization wavelength source. In fact, the efficiency reductions are different for the four colors. Referring to a constant incident photon rate of 5 x 10^{16} photons/s, we observed a reduction of 12%, 13%, 20%, and 22% of quantum efficiencies for amber, red, green, and blue characterization light sources at the end of stress. We suppose that during stress, the most degradation occurs for those binds of the dye, which are involved in the photo-generation of electron/hole pairs when green and blue light hit the sensitizer.

Figs. 5.38-5.39 show the typical DSC Nyquist plot measured during stress by means of AM 1.5 solar simulator and white LED. EIS characteristics show an enlargement of the second semicircle, which is correlated to the TiO_2/Dye/Electrolyte interface [71]. In agreement with J_{SC} degradation kinetics, the degradation of this interface can be ascribed to dye molecules degradation, which are no longer be able to photo generate electrical charge. The enlargement shown during stress is regardless of the characterization source, nevertheless it is more pronounced if the characterization is performed with AM 1.5 light source. At the end of stress, the third semicircles, which is correlated to the Nernst diffusion in the electrolyte, does not show appreciable variation. The first semicircle, which is related to the back reaction at the counter electrode, features an enlargement regardless of the characterization source. EIS measurements carried out with monochromatic light sources also show an enlargement of the second semicircle, nevertheless they feature different enlargement variations.

5.4 UV exposure accelerated stresses

5.4.1 Introduction

We studied the effects of UV irradiation on DSC by means of accelerated UV radiation stresses. A progressive degradation of open-circuit voltage occurs, while the short-circuit current suddenly drops during stress. The sudden degradation can easily be detected from DC measurements and it occurs when series resistance starts to increase. Electrolyte bleaching is the main effect for cell failure and it induces the degradation of TiO_2/Dye/Electrolyte interface as side effect. At the end of the irradiation a complete loss of electrolyte was observed.

5.4.2 Results

Figs. 5.40-5.49 summarize the data collected during NUV irradiation stresses. Fig. 5.40 shows the evolution of J-V characteristics during irradiation of a device illuminated

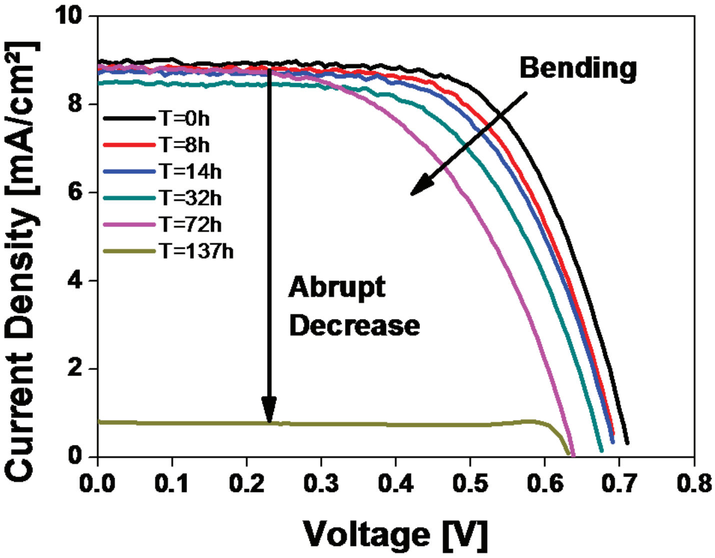

FIGURE 5.40: J-V characteristic of a DSC subjected to NUV exposure with an optical intensity I=100mW/cm^2.

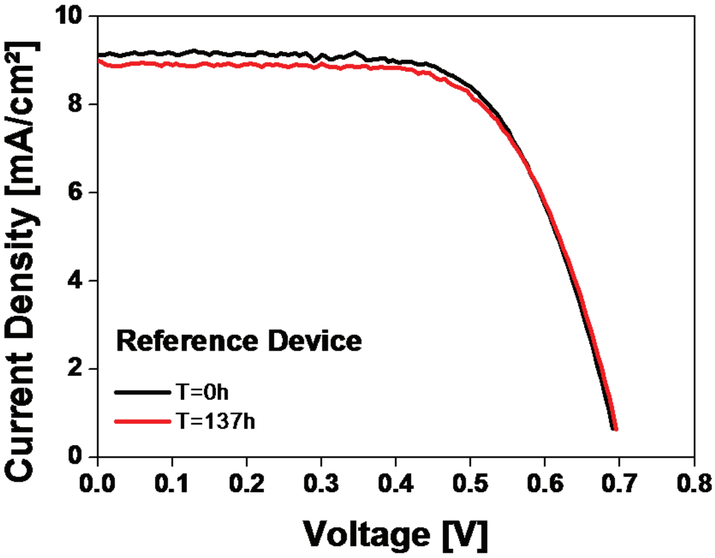

FIGURE 5.41: J-V characteristics of the reference (not irradiated) device taken at the beginning and at the end of the experiment.

with an optical intensity of 100mW/cm^2 . For comparison, we show in Fig. 5.41 the J-V characteristics of the reference device taken at the beginning and at the end of the experiment. Figs. 5.42-5.44 show the evolution of DC parameters, i.e. open-circuit voltage, short-circuit current, and efficiency, for devices subjected to different NUV intensity irradiation ranging from 10mW/cm^2 and 100mW/cm^2 . All the parameter values are normalized respect to the values of the fresh devices. Concerning those cells subjected to irradiation intensities of 50mW/cm^2 and 100mW/cm^2, V_{OC} and J_{SC} feature very different behavior: the former show a progressive degradation down to the 85% of its initial value; the latter is almost constant and it suddenly drops after 72-hours

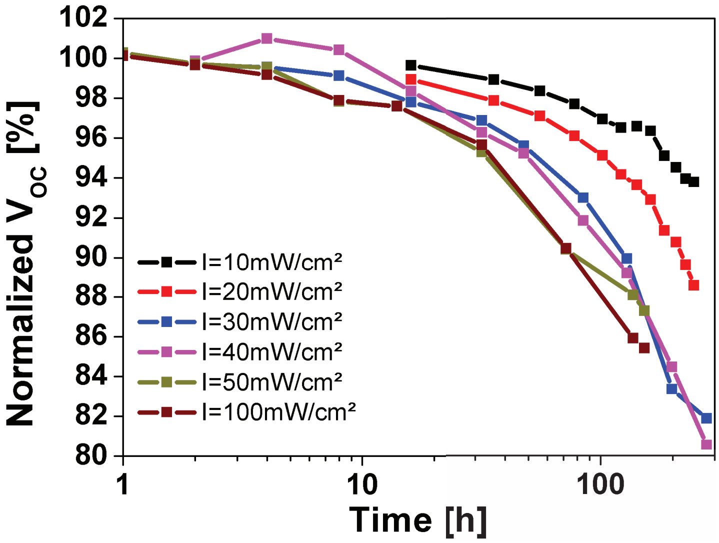

FIGURE 5.42: Evolution during stress of the open-circuit voltage as a function of irradiation time of cells subjected to different illumination intensities from 10mW/cm^2 to 100mW/cm^2.

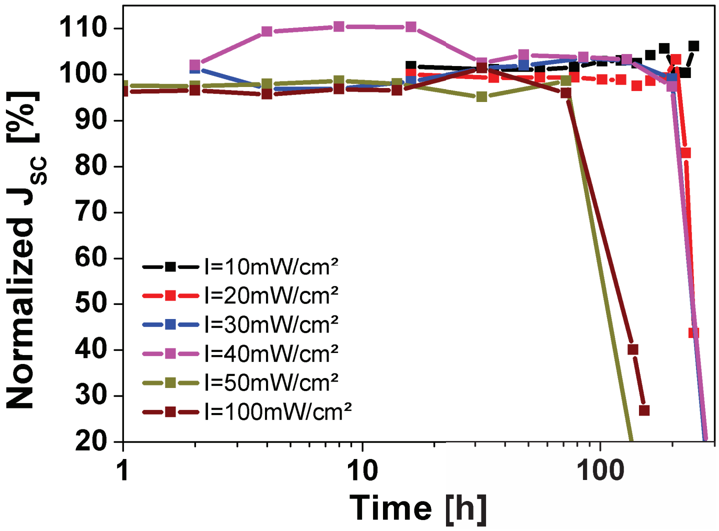

FIGURE 5.43: Evolution during stress of the short-circuit current as a function of irradiation time of cells subjected to different illumination intensities from 10mW/cm^2 to 100mW/cm^2.

irradiation.

Fig. 5.45 show the magnification of the active area of a DSC subjected to ultraviolet exposure (left) and of the reference device (right), highlighting the bleaching of the electrolyte. Fig. 5.46 shows the evolution of the series resistance of solar cell subjected to stress. The series resistance was evaluated as the slope of the J-V near the open-circuit condition. It shows an increasing behavior, featuring a large and sudden increase corresponding to the large drop of the J_{SC} , showed in Fig. 5.43. Figs. 5.47-5.49 show the evolution of the Nyquist diagram for cell subjected to 50mW/cm^2 and 100mW/cm^2 NUV irradiation.

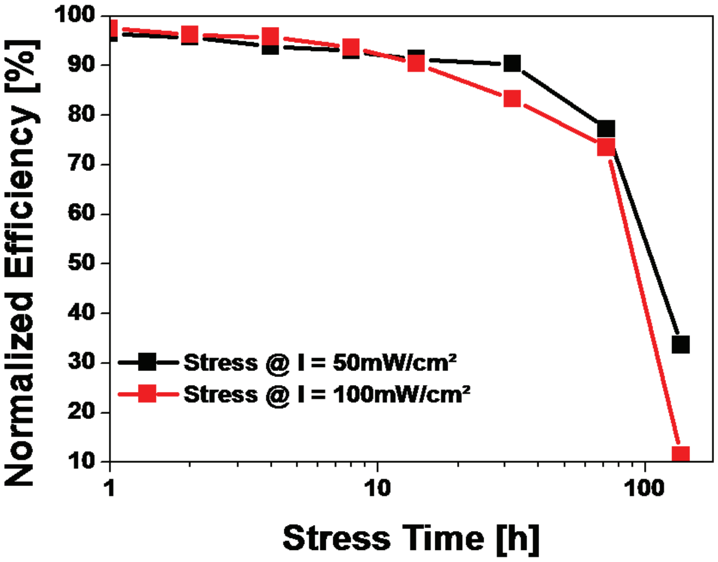

FIGURE 5.44: Evolution during stress of the cell efficiency as a function of irradiation time of cells subjected to different illumination intensities, 50mW/cm^2 and 100mW/cm^2 respectively.

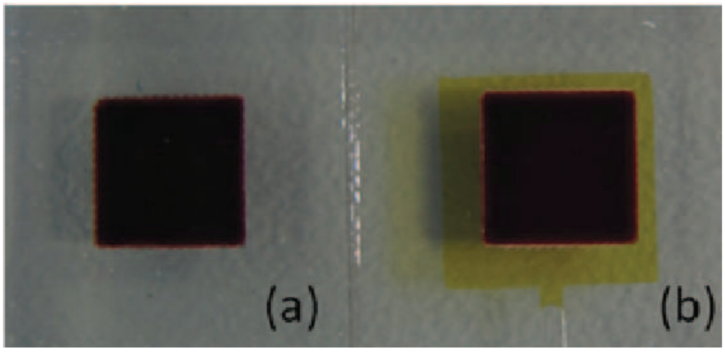

FIGURE 5.45: Two magnifications of the active area of cell subjected to NUV exposure (a) and of the reference device at end of stress (b). Cell subjected to ultraviolet irradiation shows electrolyte bleaching.

5.4.3 Discussion

As shown in Figs. 5.40 and 5.41, we observed that the J-V characteristics of the reference and irradiated cell feature different evolutions. The irradiated cell (Fig. 5.40) shows a variation of the shape of the characteristic and a reduction of the open-circuit voltage. Nevertheless, while the open-circuit voltage decreases, the short-circuit current does not features a noticeable variation at least within the 100-h exposure. After a cumulative irradiation time as large as about 140-h, the J_{SC} abruptly drops. Still, the shape of J-V characteristics changes during NUV exposure: it is noticeable a stretch out of the curves in particular near the open-circuit region. This can be ascribed to an increase of the series resistance of the solar cell which, in addition, reduces the overall efficiency as well as fill factor of the DSC. The reference cell does not show a noticeable variation of V_{OC} ,

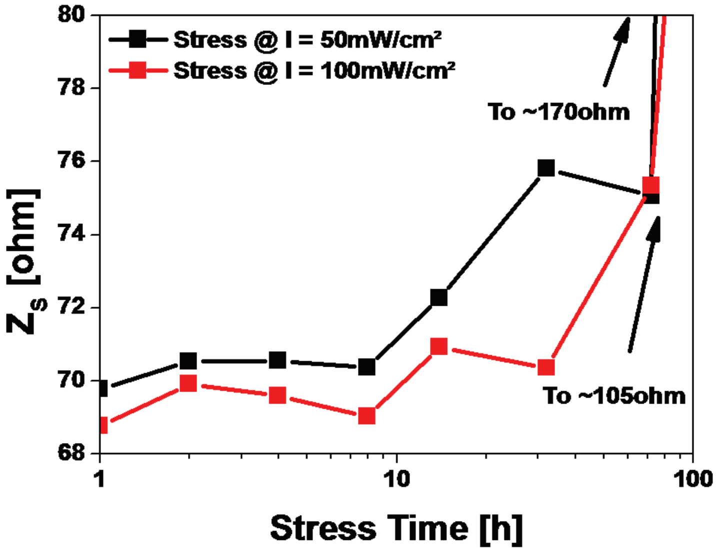

FIGURE 5.46: Evolutions of the DSC series resistance during NUV exposure for illumination intensities of 50mW/cm^2 to 100mW/cm^2.

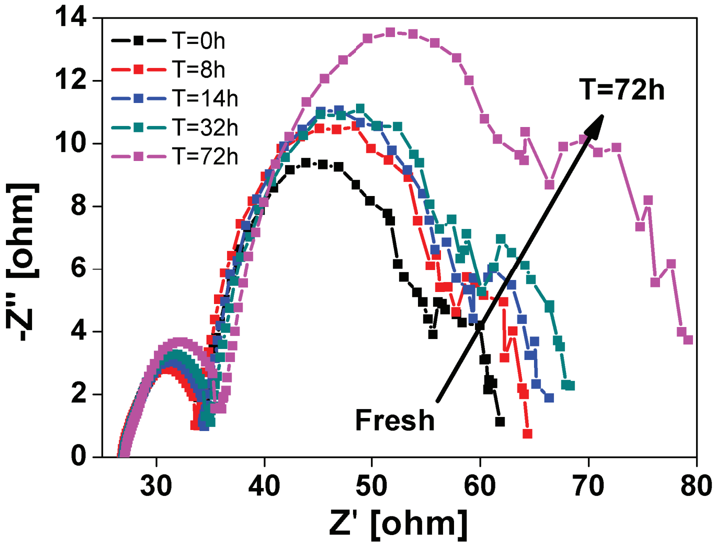

FIGURE 5.47: Evolution of the Nyquist plot of cell subjected to NUV exposure for illumination intensities of 50mW/cm^2 up to 72-hours exposure.

J_{SC} , or modifications of J-V shape during stress, except that a very marginal reduction of the short-circuit current at the end of the stress. This indicates that the evolutions changes in of the performances of the irradiated cell are dominated by the effects of UV exposure and/or by the electrical conduction. The following discussion is split into two parts. In the first part, *Effects of UV exposure upon DC Parameters*, we will discuss the degradation of DC parameters under NUV illumination. In the second part, *Analysis Degradation by means of EIS measurements*, we will discuss the degradation of NUV exposed DSC by analyzing the shape of EIS during illumination stress.

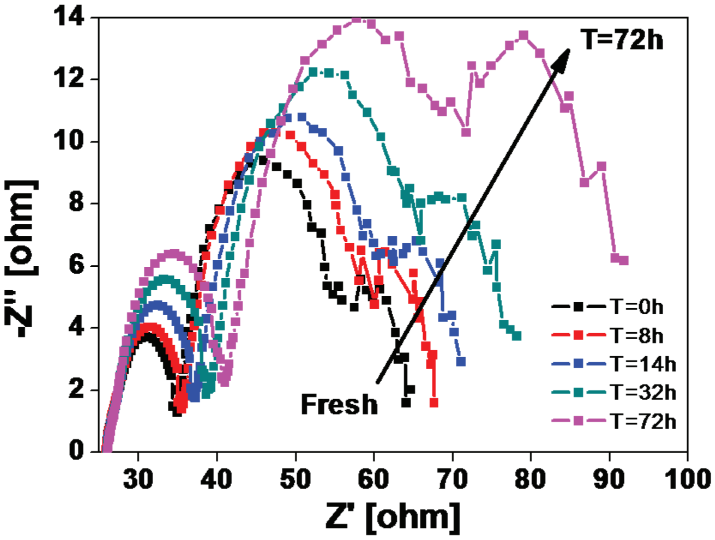

FIGURE 5.48: Evolution of the Nyquist plot of cell subjected to NUV exposure for illumination intensities of 100mW/cm^2 up to 72-hours exposure.

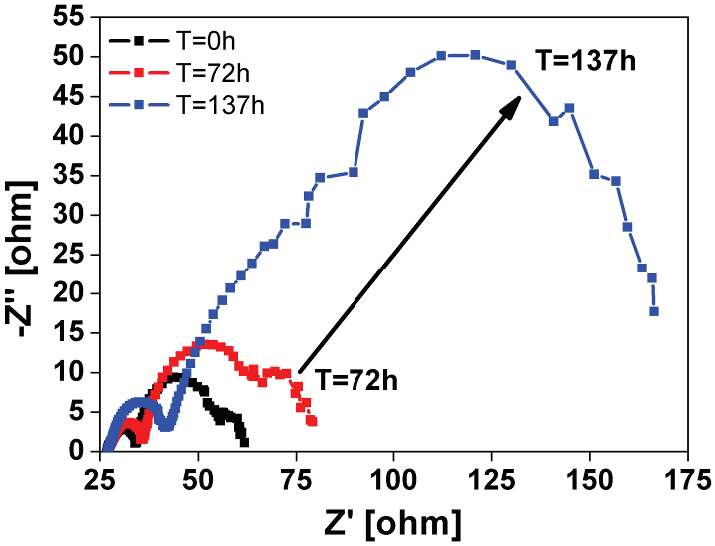

FIGURE 5.49: Evolution of the Nyquist plot of cell subjected to NUV exposure and effect of the sudden drop of J_{SC} in the EIS curves in a device illuminated at 100mW/cm^2.

Effects of UV exposure upon DC Parameters

From the DC characteristic measured by means of AM1.5 solar simulator as shown in Figs. 5.42-5.44, we can draw some considerations. In agreement with Fig. 5.40, Fig. 5.42 shows a remarkable decrease of the open-circuit voltage as the stress time increases. Since the open-circuit voltage is equal to the difference between the TiO_2quasi-Fermi level and the red-ox potential of the couple TiO_2in the electrolyte, we can tentatively suppose that NUV exposure changes the TiO_2quasi-Fermi level and/or the red-ox potential the electrolyte. Since it was asserted that TiO_2stability is unquestionable [75], we suppose that the main change occurs on the red-ox potential of the couple TiO_2. However, some recent works in literature argued that a positive shift in the conduction band of TiO_2after UV exposure could occur, see for instance [76], [77].

We observed that the degradation rate of the open-circuit voltage does not increase, by rising the optical intensities from 50mw/cm^2 to 100mW/cm^2. We suppose that this saturation could be due to the very high intensities at which the cells are exposed. A possible reason for this saturating behavior may be due to the time needed by the excited dye to exchange electrons with the electrolyte. In fact, once a dye molecule has absorbed an UV photon it takes time to exchange electrons with $TiO_2$and electrolyte: since the electron injection process into the $TiO_2$is faster than the dye reduction by the electrolyte, the limiting process is the charge exchange between dye and electrolyte. We argue that during this time, the excited molecule is unable to absorb further photons and we can figure that at high intensities irradiation the time needed for all chemical reactions eventually limits the actual degradation rate. Instead, at low illumination intensities, i.e. 10mW/cm^2, 20mW/cm^2, and 30mW/cm^2 we can extrapolate the V_{OC} degradation rate as a function of the irradiation intensities. Incidentally, by increasing the illumination intensity from 10mW/cm^2 to 50mW/cm^2 the degradation kinetics accelerates by a factor 5.

The short-circuit current features different kinetics with respect to the open-circuit voltage. Despite the progressive decrease of V_{OC} , J_{SC} remains almost unchanged, regardless the stress optical intensity, until it suddenly drop to less than 40% of their initial values. This occurs after 100-h, depending on the optical intensities. We suppose that no noticeable dye degradation occurs due to NUV exposure, at least within 100-h stress. We argue that the investigation on the sudden failure of DSC has to be mainly focused on the electrolyte rather than the sensitizer at least for DSC based on N719 dye. We suggest that UV exposure causes electrolyte bleaching through sublimation of iodine or the formation of iodate, which is in agreement with the variation of red-ox potential and then the V_{OC} reduction [78], [79]. As a consequence of the red-ox couple depletion, photo-generated hole quenching (i.e. dye reduction) by iodide ions is no longer ensured. Since the red-ox couple strongly impacts on the maximum current available for the cell, till the concentration of the red-ox couple is enough to reduce oxidized dye, no modification in the J_{SC} occurs, i.e. within 100-h stress. However, when a large amount of iodine/tri-iodide is consumed by NUV exposure, not properly reduced dye could react with other electrolyte elements (i.e. additives) which lead to the formation of new chemical species unable to photo-generate charge. As a consequence the J_{SC} dramatically drops (i.e. after 140-h stress). A visual inspection of the cell after stress shows a complete loss of color from the electrolyte, as shown in Fig. 5.45. Referring to irradiation intensities of 50mW/cm^2 and 100mW/cm^2 and according to the J-V stretch-out, the degradation of the electrolyte causes the increase of the solar cell series resistance and the sudden degradation of J_{SC} can be found between 70-h and 100-h, i.e. where the series resistance begins to increase quickly, as shown in Fig. 5.46. After stress, the series resistance values doubled with respect to their values at the beginning of stress. For low irradiation intensities, for instance $10mW/cm^2$ and $20mW/cm^2$, the sudden drop of J_{SC} occurs later than 200 hours as described above. Accordingly with the previous assumption, the UV exposure causes electrolyte bleaching, lowering the irradiation intensity more exposure time is needed to deplete the electrolyte.

Unlike what observed in our previous work 5.1, efficiency degradation kinetics do not follow the degradation kinetics of the short-circuit current. Within 100-h stress, the DSC efficiency smoothly decreases following the same trend of V_{OC} and only at the end of stress it suddenly drops in the same way as the short-circuit current. The initial smooth and progressive decrease can be ascribed to the increase of the DSC series resistance, while the suddenly drop is due to the strong reduction of the short-circuit current at the end of stress.

Analysis Degradation by means of EIS measurements

Concerning EIS measurements, both Figs. 5.47-5.48 show a general enlargement of the Nyquist plot, which is more pronounced for the cell exposed at the higher optical intensity. The three-semicircle shape is preserved till about 72-h stress, while at the end of stress the second semicircle is not longer observable, because it is mostly overwhelmed by the third one. For clarity, we have reported in Figs. 5.47 and 5.48 data till 72-h stress at illumination intensity of $50mW/cm^2$ and $100mW/cm^2$, respectively. In Fig. 5.49, we show the EIS characteristics taken in the fresh cell, after 72 hours and 140 hours. Before the sudden degradation the three semicircles feature different enlargement increments as shown in Figs. 5.47-5.49. The third semicircle shows an increment of 2.5 times, while first and second semicircles feature an increment of 1.5 times with respect to semicircle peaks of fresh device. In agreement with the discussion of the previous section, the electrolyte degradation is the main mechanism in cell failures during NUV exposure. Nernst diffusion impedance increases during stress suggesting that composition of the electrolyte (i.e. iodide/tri-iodide couple reduction) is changing. Accordingly to the depletion of the red-ox couple, reaction at counter electrode is no longer efficient and this causes the first semicircle to enlarge. Modifications in the electrolyte composition, as discussed in the previous section, impact on the reduction of oxidized dyes after photogeneration leading to a degradation of this interface, i.e. the formation of new chemical species. In fact, at the end of irradiation, i.e. after 140 hours, the third semicircle peak increases 25 times with respect to fresh value, while the first and the second semicircles increase only 7 and 4 times respect to peak values of fresh device.

5.5 Constant current stress accelerated stresses

5.5.1 Introduction

We performed positive and negative constant current stresses (CCS) on DSC in the dark with different polarization levels. We found that positive and negative CCS have different effects on DC parameters, featuring different degradation rates, depending on intensity of the stress current. In particular, positive CCS leads to the reduction of tri-iodide concentration in the electrolyte, lowering the dark current of the cell. In addition, from impedance measurements, we found that positive CCS induce the degradation of the TiO_2/Dye/electrolyte interface and negative CCS induce the degradation of Pt counter-electrode surface.

5.5.2 Results

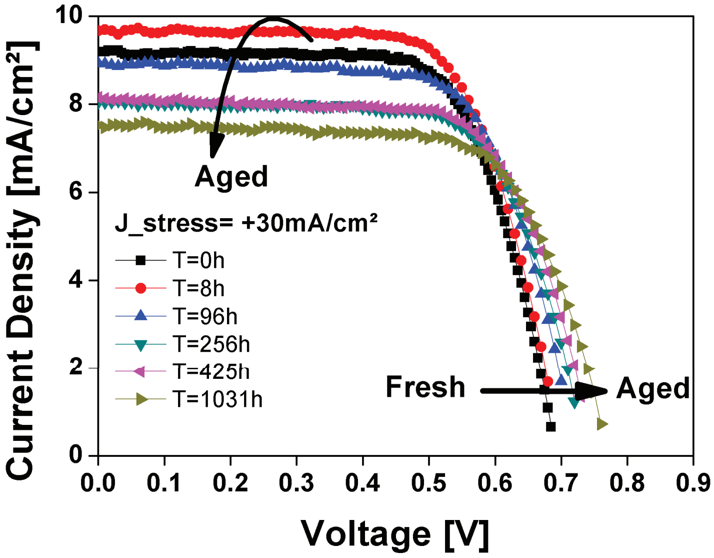

FIGURE 5.50: Evolutions of J-V characteristics of cell stressed by means of positive CCS.

Figs. 5.50-5.56 summarize the data collected during the electrical stresses. Fig. 5.50 shows the typical evolution of J-V characteristics of a selected device stressed with positive CCS at $30mA/cm^2$. For comparison, we show in Fig. 5.51 the evolution of J-V characteristics of a device subjected to negative CCS at $-30mA/cm^2$. Figs. 5.52-5.53 show the evolution of V_{OC} and J_{SC} of devices subjected to positive and negative CCS.

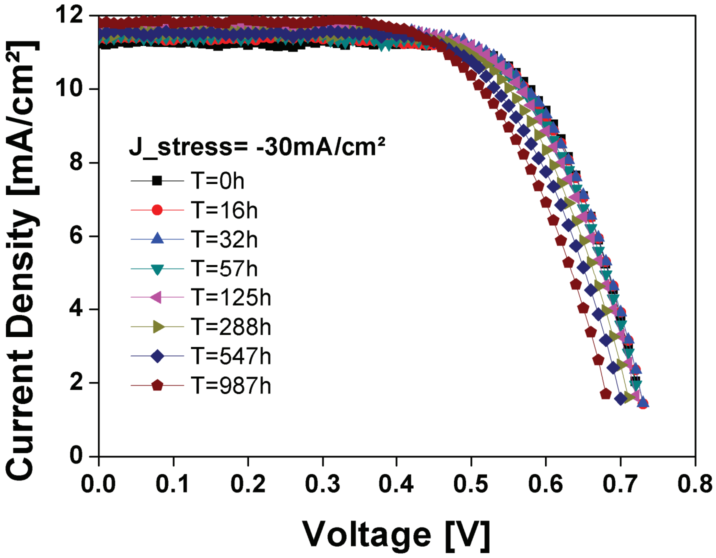

FIGURE 5.51: Evolutions of J-V characteristics of cell stressed by means of negative CCS.

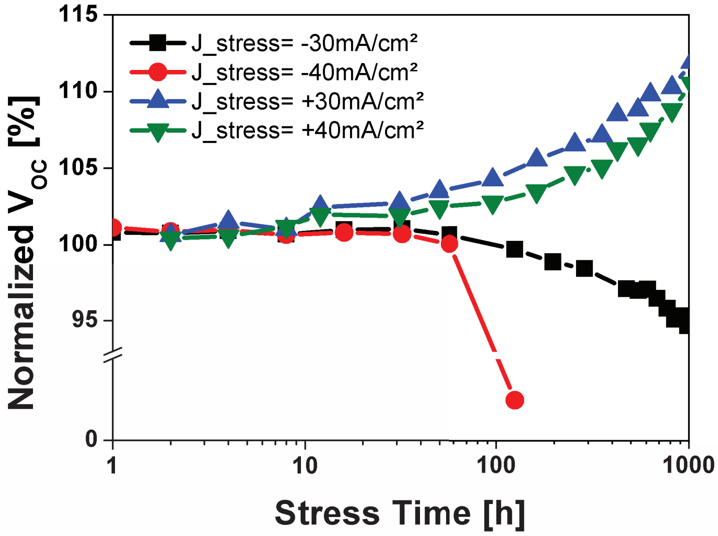

FIGURE 5.52: Evolutions of the DC parameters V_{OC} of cells subjected to positive and negative CCS.

All the parameter values are normalized respect to their respective values before stress. Regarding positive CCS, V_{OC} and J_{SC} feature very different behaviors: V_{OC} shows a smooth increase, while J_{SC} , besides a slight increment at the beginning of stress, features a progressive decrease. The V_{OC} and J_{SC} of a device stressed by means of negative CCS features a very different kinetic respect what observed for positive CCS. In fact, referring to a current density of -30mA/cm^2, V_{OC} and J_{SC} remain almost constant during stress at least till 125-h stress. Some devices, such as that reported with the red circles in Fig. 5.53 (stressed at -40mA/cm^2), exhibited a sudden failure during negative CCS with a remarkable and abrupt drop of both J_{SC} and V_{OC} . After failure, a visual inspection of

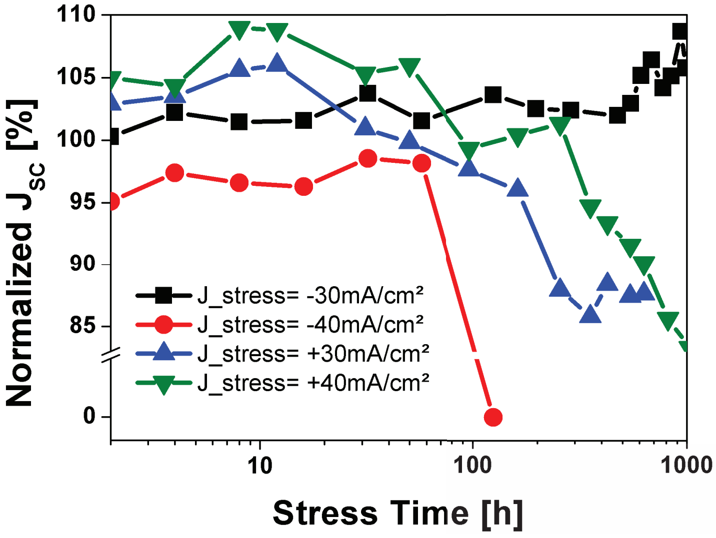

FIGURE 5.53: Evolutions of the DC parameter J_{SC} of cells subjected to positive and negative CCS.

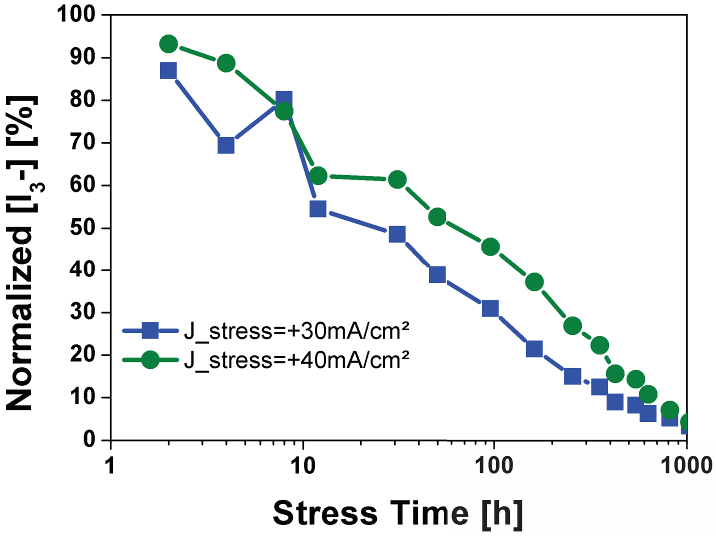

FIGURE 5.54: Evolutions of dark current of cell stressed by means of positive CCS at 30 and 40 mA/cm^2.

the device shows bleaching of the electrolyte. Fig. 5.54 shows the evolution of the concentration of tri-iodide in the electrolyte of devices stressed by means of positive CCS. The data reported in Fig. 5.54 are normalized to the respective I_3^- concentration value of fresh devices. From Fig. 5.55, we observe a progressive enlargement of the second semicircle if the cells are stressed with positive CCS. Conversely, if the cells are stressed with negative CCS, Fig. 5.56, the first semicircle is enlarged, whereas the second and the third remain almost unchanged.

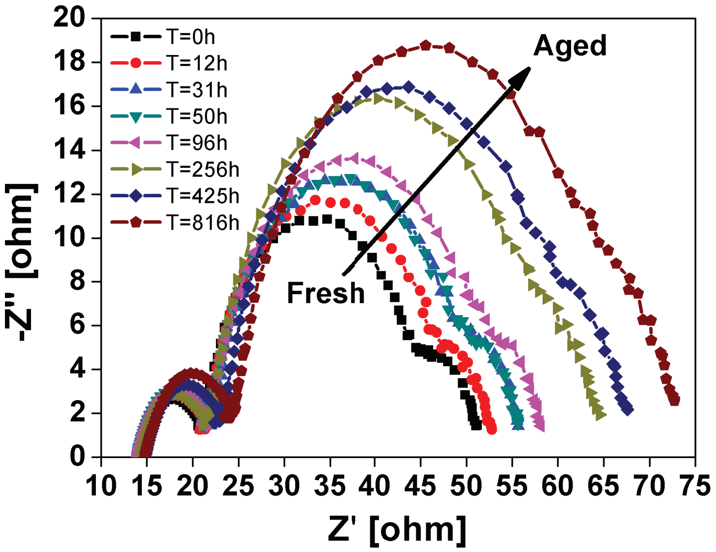

FIGURE 5.55: Evolutions of EIS characteristics of cell stressed by means of positive CCS with an absolute stress density current of $30mA/cm^2$.

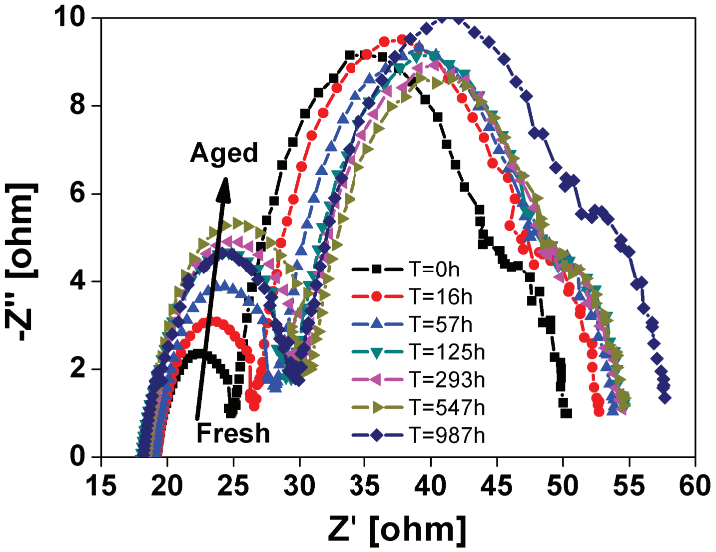

FIGURE 5.56: Evolutions of EIS characteristics of cell stressed by means of negative CCS, with an absolute stress density current of $30mA/cm^2$.

5.5.3 Discussion

Taking into account data collected in Figs. 5.50 and 5.51, we observe that the J-V characteristics of cells stressed with positive and negative CCS feature different evolutions. During positive CCS (see Fig. 5.50), we observe a progressive increment of V_{OC} , while J_{SC} features a completely different behavior. We observed an initial increase of the short-circuit current up to approximately 100-h of stress. Later on, J_{SC} monotonically decreases. Still, the shape of J-V characteristics changes during positive CCS: it is noticeable a stretch out of the curves, in particular near the open-circuit region. This can be ascribed to an increase of the series resistance of the solar cell (R_S) which, in addition, reduces the overall efficiency as well as fill factor of the DSC. During negative CCS (Fig. 5.51), the cell does not show an appreciable variation of V_{OC} or modifications of J-V shape during stress, except that a very marginal reduction of the J_{SC} at least after 125-h stress. This indicates that both CCS change the J-V characteristics of the cell, and therefore its performances, in different ways.

Observing the data shown in Figs. 5.52-5.53 two considerations are worth to be drawn. First, referring to positive CCS, V_{OC} of a DSC is equal to the difference between the conduction band energy level in $TiO_2$and the red-ox potential of the red-ox couple in the electrolyte (tri-iodide and iodide). Since it was reported that TiO_2stability is unquestionable [75], we suppose that the main change occurs on the red-ox potential of the couple I_3^-/I^-. Since, the red-ox potential depends on the molar concentration of tri-iodide in the electrolyte, a reduction of this ion specie leads to a reduction of red-ox potential and, in turn, to a reduction of V_{OC} . The small increment of the V_{OC} appears to be incoherent with the progressive reduction of the J_{SC} . In fact, V_{OC} and J_{SC} are approximately correlated by the equation:

$$V_{OC} \approx \frac{kT}{q} \ln \frac{I_{SC}}{I_O} \tag{5.1}$$

where k is the Boltzmann constant, q is the elementary charge, T is the absolute temperature, and I_0 is the dark current, and I_{SC} is the short-circuit current of the cell. At a decrease of the J_{SC} , should correspond a decrease of the V_{OC} and this is not in agreement with what observed during positive CCS. Nevertheless, I_0 is related with the molar concentration of tri-iodide in the electrolyte by the following equation:

$$I_0 \approx A\left[I_3^-\right] \tag{5.2}$$

where A is a constant reaction and $[I_3^-/I^-]$ is the concentration of oxidized red-ox mediator, I_3^-/I^-, in the solution. We suggest that the reduction rate of I_0 is greater than the reduction rate of I_{SC} therefore, the ratio between I_{SC} and I_0 increases during stress, leading to a progressive increment of the V_{OC} . From Eq5.2 we calculated the concentration of I_3^-/I^-during stress, which is reported in Fig. 5.54.

As a second remark, referring to the negative CCS at -30mA/cm^2 and to data reported in Fig. 5.51, we observed neither changes of J_{SC} , nor appreciable variation of V_{OC} , besides a very marginal J_{SC} increase and V_{OC} reduction after about 1000-h stress, which is clearer in data reported in Fig. 5.52. Most of devices subjected to negative CCS showed small variations in shape of the J-V characteristics (at least up to 1000-h stress), like the sample shown in Fig. 5.51. An example is that one stressed at -40mA/cm^2 in Figs. 5.52 and 5.53. In this device V_{OC} remains almost constant till about 50-h, then it abruptly drops. Beside the initial decrease, which is in trend with all the other devices stressed at various current densities, J_{SC} remains almost constant during stress and then it suddenly drops after 50-h stress. During negative CCS, we observed this sudden failure within 1000 hours of stress in the 85% of the stressed device. Instead, only the 15% of device subjected to positive CCS exhibited the sudden drop of J_{SC} and V_{OC} , suggesting that positive CCS require a much longer stress time to produce the device failure.

Concerning EIS measurements, data reported in the diagrams of Figs. 5.55 and 5.56 are measured by means of white LED and they refer to positive and negative CCS carried out at the same current density (in absolute value), i.e. $+30\text{mA/cm}^2$ and -30mA/cm^2, respectively. Concerning positive CCS (Fig. 5.55), the EIS curves show an enlargement of the second and third semicircles. In agreement with the reduction of tri-iodide concentration discussed above, the degradation of the TiO_2/Dye/electrolyte interface can be ascribed to the reduction of charge transfer capability between TiO_2/Dye and electrolyte. In conventional I_3^-/I^-based electrolyte, iodide concentration is much larger than that of tri-iodide and the former diffuses faster than the latter. Therefore tri-iodide contribution to the overall diffusion impedance Z_D is stronger than iodide [71]. Still, according to the variation of tri-iodide concentration, a reduction of tri-iodide concentration causes the growth of the Nernst impedance. We did not observe any significant variation of the first semicircle which means that the platinum interface is preserved at least after up to 1000-h stress. During negative CCS (Fig. 5.56), we did not observe any variation in shape of the second or third semicircle, which means that no noticeable degradation occurred at the TiO_2/Dye/electrolyte interface and no noticeable variation of the electrolyte properties occurred at least after 1000-h stress. The third semicircle, which is correlated with the red-ox reaction at the counter-electrode, features a progressive enlargement during stress, which could be ascribed to the degradation of the counter electrode. It has been proved that iodide and tri-iodide lead to the corrosion of the platinum layer during long-term test [80]. We suggest that the bias applied during stress may provide the driving force needed to activate or to accelerate some red-ox reactions between the platinum and the species dissolved into the electrolyte (i.e. red-ox couple, additives, solvents, etc), accelerating the corrosion of the platinum layer and in turn the reduction of the counter-electrode surface. A comparison between EIS measured during positive and negative CCS permits us to assert that the most of degradation occurs at those interfaces where the electrons are emitted during stress, that is, at the TiO_2/Dye/Electrolyte and the counter electrode interfaces, respectively.

Chapter 6

Conclusions

6.1 Dye-sensitized solar cells reliability results summary

In this work we explored the dye-sensitized solar cells technology as an alternative to conventional PV. We performed and investigated the characterization and the reliability of DSC respectively. Focusing on the latter purpose, in order to study the effects of sunlight exposure on DSC, the reliability study was carried out by means of accelerated stresses, that is: AM1.5 solar simulator stress, which allowed us to mimic the sunlight exposure, UV illumination and white light exposures, pure thermal and constant current stresses. This final chapter presents a summary of the results described and discussed in the previous Chapter 5 and addresses some comments and remarks about this work. From the accelerated stresses by means of AM1.5 solar simulator, we found that the degradation kinetics (as a function of time) is different for the open circuit voltage (V_{OC}) and for the short circuit current (J_{SC}): the former monotonically decreases while the latter increases at the beginning of the stress and then decreases for longer stress times. The duration of the turn around phase is strongly dependent on the illumination intensity used for the accelerated stress: the higher the illumination level, the shorter the turn around phase. The cells, which are not illuminated, do not show appreciable degradation of open-circuit voltage and short-circuit current at room temperature as well. The illuminated device features faster degradation kinetics with higher illumination levels likely due increase of the interface temperature, as also confirmed by pure thermal stress. The responsible of the degradation during thermal or illumination stress is the formation of defects and chemical species at TiO_2/sensitizer/electrolyte interface which reduces the charge transfer at interface and the ion migration across electrolyte. More in details, concerning thermal stresses, temperature has a twofold impact on cell performance. A moderate temperature around 60°C initially improves the cell efficiency in few hours: in fact, a thermal-induced annealing can recover and rearrange some dangling or weak bonds at the TiO_2interface or among the dye molecules enhancing the photo-generation efficiency of the dye material. At higher temperatures or for longer storage times, the temperature strongly reduces the efficiency and the short-circuit current. From the EIS evolution we ascribed this degradation to the TiO_2/Dye/Electrolyte interface degradation, which is likely due to some permanent reaction between the dye and the electrolyte or with hydrogenoid species.

Concerning the suitability of white LED as stress and characterization light source, we found that exposure to white light leads to the degradation of DSC performances. In particular, we found that, even though white LED spectrum has not near-UV component, dye molecules are not longer be able to absorb wavelength ranging from 300-400nm. On the other hand, among the six characterization light sources, only AM 1.5 solar simulator pointed out the degradation of the dye absorption spectrum in the near-UV. Since variation in dye absorption spectrum is not uniform during optical and electrical stress, monochromatic light sources can be used to detect variation in tight absorption spectrum region giving more information on DSC degradation mechanism.

Regarding UV exposure, data shown in this work clearly suggest that NUV has detrimental effects on DSC performance, in a time as short as few hundred hours of exposure in the NUV range between 300 and 400nm wavelength. We found that the main mechanism for the cell failure during NUV exposure is the electrolyte bleaching, which occurs within a few hours of UV exposure. It is worth to remark that the sensitizer seems to have a minor role in cell degradation until the sudden J_{SC} drop occurs. Further investigations on several open issues are worthy to be undertaken, for instance to assess the role of the irradiation intensity on the device degradation rate. In fact we found a saturating dependence on the cell degradation kinetics. On one hand, this suggests that, operation in environments with higher UV intensities (such as operation in high atmosphere) is not much more critical than ground level. On the other hand, this points out that even very small UV intensities can lead to strong degradation in a limited time. These findings point out that DSC are very sensitive to near-UV rays. Good shielding and encapsulation bring benefits for a reliable operation over time, even though it potentially compromises the good transparency of the substrate and encapsulation which is mandatory for good power conversion efficiency. Furthermore, a good UV filtering might be unpractical in a device in which a primary goal is the low cost.

The reported data also suggest that efforts must be done for improving the electrolyte reliability. The iodide/tri-iodide should be substituted or additives have to be added to the red-ox couple in order to prevent electrolyte bleaching by NUV exposure. The use of solid or semisolid electrolyte, such as polymer gel electrolyte can be another interesting solution to improve the cell stability and lifetime. In fact, they were found to result in remarkably stable devices, under thermal and illumination stress. However, some issues still regarding about the lower performance of the conversion and transport process with this type of electrolyte [75].

Constant current stress carried out at dark on dye-sensitized solar cells could be the case when some cells of solar module are shaded or not working. We found that both CCS induce the degradation of DSC performance. In particular we found that, positive CCS reduces the tri-iodide concentration in the electrolyte reducing the electron transfer capability of the TiO$_2$/Dye/electrolyte interface and the red-ox properties of the electrolyte. On the other hand, negative CCS leads the degradation of counter-electrode, accelerating the corrosion of the Pt electrode by the electrolyte. Our achievements pointed out both positive and negative CCS have a detrimental effect on the performance of DSC. The data reported suggest that some electrical solutions have to be taken when DSC are used in a solar module, in order to prevent electrical stress when some solar cells are shaded or not working.

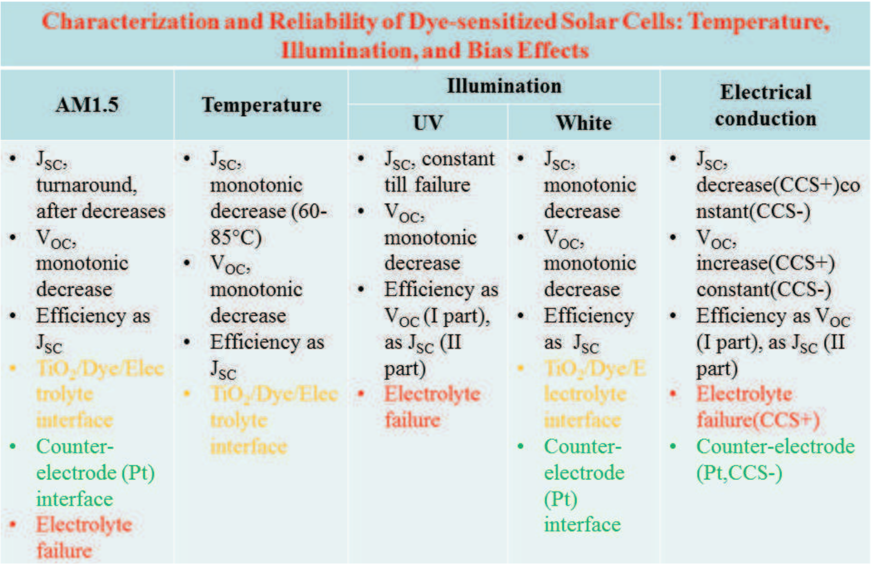

Characterization and Reliability of Dye-sensitized Solar Cells: Temperature, Illumination, and Bias Effects

AM1.5	Temperature	Illumination		Electrical conduction
		UV	White	
• J_{SC}, turnaround, after decreases • V_{OC}, monotonic decrease • Efficiency as J_{SC} • TiO$_2$/Dye/Electrolyte interface • Counter-electrode (Pt) interface • Electrolyte failure	• J_{SC}, monotonic decrease (60-85°C) • V_{OC}, monotonic decrease • Efficiency as J_{SC} • TiO$_2$/Dye/Electrolyte interface	• J_{SC}, constant till failure • V_{OC}, monotonic decrease • Efficiency as V_{OC} (I part), as J_{SC} (II part) • Electrolyte failure	• J_{SC}, monotonic decrease • V_{OC}, monotonic decrease • Efficiency as J_{SC} • TiO$_2$/Dye/Electrolyte interface • Counter-electrode (Pt) interface	• J_{SC}, decrease(CCS+)constant(CCS-) • V_{OC}, increase(CCS+) constant(CCS-) • Efficiency as V_{OC} (I part), as J_{SC} (II part) • Electrolyte failure(CCS+) • Counter-electrode (Pt,CCS-)

FIGURE 6.1: The table summarizes all the most significant results obtained from the accelerated stresses carried out during this work.

The table reported in Fig. 6.1 summarizes the main results obtained from all the accelerated stresses carried out during this work and in particular compares the AM1.5 accelerated stress (which is the closest to normal operation) with the other sub-stresses. Moreover, the summary reported in Fig. 6.1 allows to figure out who is responsible of solar cells degradation under sunlight exposure. As widely described above, we found that sunlight exposure affects all the interfaces and almost all the materials that form a DSC, that is the TiO$_2$/Dye/electrolyte and the Pt interface as well as the electrolyte. Among the interfaces cited previously, we found that the TiO$_2$/Dye/electrolyte interface is mostly affected by temperature when exposed to sunlight as pointed out by the pure thermal stresses, while temperatures does not affect the other DSC materials and interfaces. The counter-electrode interface, which is made of Pt in these devices, degrades under sunlight exposure due to the current flowing during normal operation as observed from the CCS. Electrolyte is mostly affected by the UV component present in the sunlight spectrum which is significant even at ground level. In fact, accelerated stresses by means of UV illumination affected only the electrolyte leading to the bleaching. Nevertheless, the TiO_2/Dye/electrolyte interface is also subjected to degradation under UV exposure, but it is preserved at least until the failure of the electrolyte. Finally, remarkable is the comparison between AM1.5 and white-LED illumination effects. These accelerated stresses are very similar, in fact they both involve the illumination of the cell (and in turn the increase of cell temperature, especially at high illumination intensities) and the flow of current through the cell. Consequently they degraded the TiO_2/Dye/electrolyte and Pt interfaces as gathered above. However, fundamental is the difference between the AM1.5 and the white-LED spectra: in fact, since the latter does not have UV component, illumination by means of white light does not affect the electrolyte.

These are just preliminary results on the DSC reliability and many issues are still open. For instance, some of the accelerated stresses performed pointed out the formation of defects at the TiO_2/Dye/Electrolyte interface. The nature of these defects as well as the most suitable degradation model are worth to be addressed and investigated. In addition, we found that DSC can recover from degradation by means of cell bias or annealing phase. Therefore more study on the understanding of the transient or permanent cell degradation should be carried out. All the illumination stresses performed during this work took into account two cell biases during stresses: one was the open-circuit condition and the other was near the short-circuit region. It could be worth to study cells degradation when they work at their MPP (maximum power point) in order to have a picture of DSC degradation at this significant working point. Concerns for electrolyte under UV exposure must be taken. $TiO_2$is a powerful catalyst under UV exposure and it promotes reactions which involve the electrolyte. Investigation on the use of different electrolyte composition should be done in order to evaluate the reliability improvements that a different electrolyte can give to DSC.
All these issues are worth of further investigations in order to promote dye-sensitized solar cells as a new photovoltaics technology.

List of Publications

Journals

- D. Bari, N. Wrachien, R. Tagliaferro, T.M. Brown, A. Reale, A. Di Carlo, G. Meneghesso, A. Cester, *Comparison between positive and negative constant current stress on dye-sensitized solar cells*, Microelectronics Reliability, Volume 53, Issues 9-11, September-November 2013, Pages 1804-1808;
- N. Wrachien, A. Cester, D. Bari, R. Capelli, R. D'Alpaos, M. Muccini, A. Stefani, G. Turatti, G. Meneghesso, *Effects of constant voltage stress on p- and n-type organic thin film transistors with poly(methyl methacrylate) gate dielectric*, Microelectronics Reliability, Volume 53, Issues 9-11, September-November 2013, Pages 1798-1803;
- D. Bari, N. Wrachien, R. Tagliaferro, T. M. Brown, A. Reale, A. Di Carlo, G. Meneghesso, and A. Cester. *Reliability study of dye-sensitized solar cells by means of solar simulator and white LED*, Microelectronics Reliability, Vol. 52, Issue 9-10, pp. 2495-2499, Sept-Oct. 2012;
- N. Wrachien, D. Bari, J. Kovac, J. Jakabovic, D. Donoval, G. Meneghesso, and A. Cester. *Enhanced permanent degradation of organic TFT under electrical stress and visible light exposure* Microelectronics Reliability, Vol. 52, Issue 9-10, pp. 2490-2494, Sept-Oct. 2012;
- N. Wrachien, A Cester, D. Bari, J. Kovac, J. Jakabovic, D. Donoval, G. Meneghesso *Visible Light and Low-Energy UV Effects on Organic Thin-Film Transistors*", IEEE Transaction on Electron Devices, Vol. 59, Issue 5, pp. 1501-1509, May 2012;
- D. Bari, A. Cester, N. Wrachien, G. Meneghesso, L. Ciammaruchi, Thomas M. Brown, Andrea Reale, A. Reale, Aldo Di Carlo *Reliability Study of Ruthenium-based Dye-Sensitized Solar Cells (DSSCs)*, IEEE - Journal of Photovoltaics, Vol. 2, Issue. 1, p. 27-34, Jan. 2012;
- N. Wrachien, A Cester, D. Bari, G. Meneghesso, J. Kovac, J. Jakabovic, D. Donoval, *Near-UV Irradiation Effects on Pentacene Based Organic Thin Film Transistors*, IEEE - Transaction on Nuclear Science, Vol. 58, Issue 6, pp. 2911-2917, Dec 2011;

- D. Bari, N. Wrachien, R. Tagliaferro, S. Penna, T.M. Brown, A. Reale, A. Di Carlo, G. Meneghesso, A. Cester, *Thermal stress effects on Dye-Sensitized Solar Cells (DSSCs)*, Microelectronics Reliability, Vol 51, Issues 9-11, Pages 1762-1766, September-November 2011.

Conferences

- D. Bari, N. Wrachien, R. Tagliaferro, T.M. Brown, A. Reale, A. Di Carlo, G. Meneghesso, A. Cester, *Comparison between positive and negative constant current stress on dye-sensitized solar cells*, 24th European Symposium on Reliability of Electron Devices, Failure Physics and Analysis - ESREF 2013, Arcachon, France, September 30th - October 4th 2013;
- N. Wrachien, A. Cester, D. Bari, R. Capelli, R. D'Alpaos, M. Muccini, A. Stefani, G. Turatti, G. Meneghesso, *Effects of constant voltage stress on p- and n-type organic thin film transistors with poly(methyl methacrylate) gate dielectric* 24th European Symposium on Reliability of Electron Devices, Failure Physics and Analysis - ESREF 2013, Arcachon, France, September 30th - October 4th 2013;
- D. Bari, N. Wrachien, R. Tagliaferro, T.M. Brown, A. Reale, A. Di Carlo, G. Meneghesso, A. Cester, *Study of the Effects of UV-Exposure on Dye-Sensitized Solar Cells*, 2013 IEEE International Reliability Physics Symposium - IRPS 2013, Monterey, CA, USA April 14th -18th, 2013;
- N. Wrachien, D. Bari, J. Kovac, J. Jakabovic, Martin Weis, D. Donoval, G. Meneghesso, and A. Cester, *Effects of Positive and Negative Constant Voltage Stress on Organic TFTs*, 2013 IEEE International Reliability Physics Symposium - IRPS 2013, Monterey, CA, USA April 14th -18th, 2013;
- N. Wrachien, A. Cester, D. Bari, G. Meneghesso, Y.Q. Wu and P.D. Ye, *Comparison between uniform and CHC stress on III-V MOSFETs*, 21st European Workshop on Heterostructure Technology - HETECH 2012, 5-7 November 2012, Barcelona, Spain;
- D. Bari, N. Wrachien, R. Tagliaferro, T. M. Brown, A. Reale, A. Di Carlo, G. Meneghesso, and A. Cester. *Reliability Study of Dye-Sensitized Solar Cells by means of Solar Simulator and White LED*, 23st European Symposium on Reliability of Electron Devices, Failure Physics and Analysis - ESREF 2012, Cagliari, Italy, October 1-5, 2012;

- N. Wrachien, D. Bari, J. Kovac, J. Jakabovic, D. Donoval, G. Meneghesso, and A. Cester, *Enhanced Permanent Degradation of Organic TFT under electrical stress and visible light exposure*, 23st European Symposium on Reliability of Electron Devices, Failure Physics and Analysis - ESREF 2012, Cagliari, Italy, October 1-5, 2012;

- D. Bari, A. Cester, N. Wrachien, G. Meneghesso, R. Tagliaferro, T. M. Brown, A. Reale, A. Di Carlo, *Study of the Effects of UV-Exposure on Dye-Sensitized Solar Cells*, 2012 IEEE Nuclear and Space Radiation Effects Conference - NSREC 2012, Miami, FL, USA, July 16-20, 2012;

- N. Wrachien, A. Cester, D. Bari, G. Meneghesso, J. Kovac, J. Jakabovic and D. Donoval, *Improved Tolerance against UV and Alpha Irradiation of Encapsulated Organic TFTs*, 2012 IEEE Nuclear and Space Radiation Effects Conference - NSREC 2012, Miami, FL, USA, July 16-20, 2012;

- N. Wrachien, A. Cester, D. Bari, J. Kovac, J. Jakabovic, D. Donoval, G. Meneghesso, *Visible Light and Low-Energy UV Effects on Organic Thin-Film Transistors*, IEEE Transaction on Electron Devices, Vol. 59, Issue 5, pp. 1501-1509, May 2012;

- N. Wrachien, A. Cester, D. Bari, G. Meneghesso, J. Kovac, J. Jakabovic, D. Donoval, *Organic Thin Film Transistor Degradation Under Sunlight Exposure*, 2012 IEEE International Reliability Physics Symposium - IRPS 2012, Anaheim, CA, USA April 15-19, 2012;

- A. Cester, D. Bari, N. Wrachien, G. Meneghesso, *Study of the effect of stress-induced trap levels on OLED characteristics by numerical model*, 2012 IEEE International Reliability Physics Symposium - IRPS 2012, Anaheim, CA, USA April 15-19, 2012;

- N. Wrachien, A. Cester, D. Bari, E. Zanoni, G. Meneghesso, Y.Q. Wu and P.D. Ye "*Effects of Channel Hot Carrier Stress on III-V Bulk Planar MOSFETs*, 2012 IEEE International Reliability Physics Symposium - IRPS 2012, , Anaheim, CA, USA April 15-19, 2012;

- D. Bari, N. Wrachien, A. Cester, G. Meneghesso, R. Tagliaferro, S. Penna, T. M. Brown, A. Reale, A. Di Carlo, *Thermal Stress Effects on Dye-Sensitized Solar Cells (DSSCs)*" 22nd European Symposium on Reliability of Electron Devices, Failure Physics and Analysis - ESREF 2011, Bordeaux - France, October 3rd-7th, 2011;

- N. Wrachien, A Cester, D. Bari, G. Meneghesso, J. Kovac, J. Jakabovic, D. Donoval, *Near-UV Irradiation Effects on Pentacene Based Organic Thin Film Transistors*, 48th IEEE - Nuclear and Space radiation Effects Conference - NSREC 2011, Las Vegas, NV, USA July 25-29, 2011;
- D. Bari, N. Wrachien, A. Cester, G. Meneghesso, R. Tagliaferro, S. Penna, T. M. Brown, A. Reale, A. Di Carlo, *Optical Stress and Reliability Study of Ruthenium-based Dye-Sensitized Solar Cells (DSSC)*, 2011 IEEE International Reliability Physics Symposium - IRPS 2011, Monterey, CA, USA April 10-14, 2011;
- N. Wrachien, A. Cester, D. Bari, G. Meneghesso, J. Kovac, J. Jakabovic, M. Sokolsky, D. Donoval, J.Cirak, *Low-Energy UV Effects on Organic Thin-Film-Transistors*, 2011 IEEE International Reliability Physics Symposium - IRPS 2011, Monterey, CA, USA April 10-14, 2011.

Appendix A

Appendix A: photovoltaics timeline

PV Timeline [8], [81]

Year	Event
1839	Alexandre Edmond Becquerel observes the photovoltaic effect via an electrode in a conductive solution exposed to light;
1873	Willoughby Smith finds that selenium shows photo-conductivity;
1877	W.G. Adams and R.E. Day observed the photovoltaic effect in solidified selenium, and published a paper on the selenium cell. 'The action of light on selenium', in "Proceedings of the Royal Society, A25, 113;
1883	Charles Fritts develops a solar cell using selenium on a thin layer of gold to form a device giving less than 1% efficiency;
1887	Heinrich Hertz investigates ultraviolet light photoconductivity and discovers the photoelectric effect;
1887	James Moser reports dye sensitised photoelectrochemical cell;
1888	Edward Weston receives patent US389124, "Solar cell," and US389125, "Solar cell";
1888-91	Aleksandr Stoletov creates the first solar cell based on the outer photoelectric effect;
1894	Melvin Severy receives patent US527377, "Solar cell" and US527379, "Solar cell";
1897	Harry Reagan receives patent US588177, "Solar cell";
1901	Philipp von Lenard observes the variation in electron, energy with light frequency;
1904	Wilhelm Hallwachs makes a semiconductor-junction solar cell (copper and copper oxide);

1905	Albert Einstein publishes a paper explaining the photoelectric effect on a quantum basis;
1913	William Coblentz receives US1077219, "Solar cell";
1914	Sven Ason Berglund patents "methods of increasing the capacity of photosensitive cells";
1916	Robert Millikan conducts experiments and proves the photoelectric effect;
1918	Jan Czochralski, a Polish scientist, produces a method to grow single crystals of metal. Decades later, the method is adapted to produce single-crystal silicon;
1920s	Solar water-heating systems, utilizing "flat collectors" (or "flat-plate collectors"), relied upon in homes and apartment buildings in Florida and southern California;
1932	Audobert and Stora discover the photovoltaic effect in Cadmium selenide (CdSe), a photovoltaic material still used today;
1935	Anthony H. Lamb ("Tony" Lamb) receives patent US2000642, "Photoelectric device";
1941	Russell Ohl files patent US2402662, "Light sensitive device";
1948	Gordon Teal and John Little adapt the Czochralski method of crystal growth to produce single-crystalline germanium and, later, silicon;
1950s	Bell Labs produce solar cells for space activities;
1953	Gerald Pearson begins research into lithium-silicon photovoltaic cells;
1954	Bell Labs announces the invention of the first modern silicon solar cell. Shortly afterwards, they are shown at the National Academy of Science Meeting. These cells have about 6% efficiency. The New York Times forecasts that solar cells will eventually lead to a source of "limitless energy of the sun";
1955	Western Electric licences commercial solar cell technologies. Hoffman Electronics-Semiconductor Division creates a 2% efficient commercial solar cell for \$25/cell or \$1,785/Watt;
1957	AT&T assignors (Gerald L. Pearson, Daryl M. Chapin, and Calvin S. Fuller) receive patent US2780765, "Solar Energy Converting Apparatus". "They refer to it as the "solar battery". Hoffman Electronics creates an 8% efficient solar cell;
1958	T. Mandelkorn, U.S. Signal Coprs Laboratories, creates n-on-p silicon solar cells, which are more resistant to radiation damage and are better suited for space. Hoffman Electronics create 9% efficient solar cells. Vanguard I, the first solar powered satellite, was launched with a 0.1W, 100cm^2 solar panel;

1959	Hoffman Electronics creates a 10% efficient commercial solar cell, and introduces the use of a grid contact, reducing the cell's resistance;
1960	Hoffman Electronics creates a 14% efficient solar cell;
1961	"Solar Energy in the Developing World" conference is held by the United Nations;
1962	The Telstar communications satellite is powered by solar cells;
1963	Sharp Corporation produces a viable photovoltaic module of silicon solar cells;
1964	Farrington Daniels' landmark book, Direct Use of the Sun's Energy, published by Yale University Press;
1966	NASA Orbiting Astronomical Observatory launched with 1 kW array;
1967	Soyuz 1 is the first manned spacecraft to be powered by solar cells;
1967	Akira Fujishima discovers the Honda-Fujishima effect which is used for hydrolysis in the photo-electrochemical cell;
1968	Roger Riehl introduces the first solar powered wristwatch;
1970	First highly effective GaAs heterostructure solar cells are created by Zhores Alferov and his team in the USSR;
1971	Salyut 1 is powered by solar cells;
1972	First PV conference to include a session on terrestrial applications (IEEE);
1973	A big year in photovoltaics: Worldwide oil crisis spurs many nations to consider renewable energy including photovoltaics; Cherry Hill Conference in USA (established photovoltaics' potential and legitimacy for government research funding); World's first solar powered residence (University of Delaware, USA) built with Cu2S (not c-Si) solar modules;
1973	Skylab is powered by solar cells;
1974	Florida Solar Energy Center begins;
1974	Project Sunshine initiated in Japan to foster growth of PV industry and applications; Tyco (USA) grows 2.5 cm wide Si ribbon for photovoltaics, first alternative to Si wafers;
1974	J. Baldwin, at Integrated Living Systems, co-develops the world's first building (in New Mexico) heated and otherwise powered by solar and wind power exclusively;
1975	1975 First book dedicated to PV science and technology by Hovel (USA);
1976	David Carlson and Christopher Wronski of RCA Laboratories create first amorphous silicon PV cells, which have an efficiency of 1.1%;
1977	The Solar Energy Research Institute is established at Golden, Colorado;
1977	President Jimmy Carter installs solar panels on the White House and promotes incentives for solar energy systems;

1977	The world production of photovoltaics cells exceeded 500kW;
1978	First solar-powered calculators;
1970s	”Energy Crisis”; groundswell of public interest in solar energy use: photovoltaic and active and passive solar, including in architecture and off-grid buildings and home sites;
1980	John Perlin and Ken Butti’s landmark book A Golden Thread published, covering 2500 Years of Solar Technology from the Greeks and Romans until the modern day;
1980	The Institute of Energy Conversion at University of Delaware develops the first thin film solar cell exceeding 10% efficiency using Cu_2S/CdS technology;
1981	350 kW Concentrator array installed in Saudi Arabia;
1982	First 1 MW utility scale PV power plant (CA, USA) with Arco Si modules on 2-axis trackers;
1983	Worldwide photovoltaic production exceeds 21.3 megawatts, and sales exceed $250 million;
1984	30,000 SF Building-Integrated Photovoltaic [BI-PV] Roof completed for the Intercultural Center of Georgetown University. At the time of the 20th Anniversary Journey by Horseback for Peace and Photovoltaics in 2004 it was still generating an average of one MWh daily as it has for twenty years in the dense urban environment of Washington, DC.;
1984	6 MW array installed in Carrisa Plains CA, USA;
1985	A big year for high-efficiency Si solar cells: Si solar cell ¿20% under standard sunlight (UNSW, Australia) and ¿25% under 200X concentration (Stanford Univ. USA);
1985	20% efficient silicon cells are created by the Centre for Photovoltaic Engineering at the University of New South Wales;
1986	Solar-Voltaic Dome$^{\text{TM}}$’ patented by Lt. Colonel Richard T. Headrick of Irvine, CA as an efficient architectural configuration for building-integrated photovoltaics [BI-PV]; Hesperia, CA field array;
1986	President Ronald Reagan removes solar panels from the White House;
1986	First commercial thin-film power module, the a-Si G4000 from Arco Solar (USA);
1987	Fourteen solar powered cars complete the 3200 km World Solar Challenge race (Australia) with the winner averaging 70 kph;
1989	Reflective solar concentrators are first used with solar cells;
1990	The Cathedral of Magdeburg installs solar cells on the roof, marking the first installation on a church in East Germany.

1988-1991	AMOCO/Enron used Solarex patents to sue ARCO Solar out of the business of a-Si (see Solarex Corp.(Enron/Amoco) see Arco Solar, Inc.Dd);
1991	the Dye-sensitized solar cell is invented;
1991	President George H. W. Bush directs the U.S. Department of Energy to establish the National Renewable Energy Laboratory (transferring the existing Solar Energy Research Institute);
1992	University of South Florida fabricates a 15.89-percent efficient thin-film cell;
1993	The National Renewable Energy Laboratory's Solar Energy Research Facility is established;
1994	NREL develops a GaInP/GaAs two-terminal concentrator cell (180 suns) which becomes the first solar cell to exceed 30% conversion efficiency;
1995	"'1000 roofs" German demonstration project to install photovoltaics on houses, which triggered the present favorable PV legislation in Germany, Japan and other countries;
1996	The National Center for Photovoltaics is established. Graetzel, École Polytechnique Fédérale de Lausanne, Lausanne, Switzerland achieves 11% efficient energy conversion with dye-sensitized cells that use a photoelectrochemical effect.
1997	Worldwide PV production reaches 100 MW per year;
1998	Cu(InGa)Se2 thin-film solar cell reaches 19% efficiency (NREL, US) comparable with multicrystalline Si. First concentrating array for space launched on Deep Space 1 by US (5 kW using high efficiency GaInP/-GaAs/Ge triple junction cells)
1999	Total worldwide installed photovoltaic power reaches 1,000 megawatts;
2000	Olympics in Australia highlight wide range of PV applications, and the awarding of the first Bachelor of Engineering degrees in Photovoltaics and Solar Engineering (UNSW, Australia);
2002	Cumulative worldwide installed photovoltaics reaches 2000 MW;
2003	9 kW PV and a solar thermal systems installed on grounds keeping building at the White House;
2004	California Governor Arnold Schwarzenegger proposed Solar Roofs Initiative for one million solar roofs in California by 2017;
2004	Kansas Governor Kathleen Sebelius issued a mandate for 1,000 MWp renewable electricity in Kansas by 2015 per Executive Order 04-05;
2006	Polysilicon use in photovoltaics exceeds all other poly-silicon use for the first time;

2006	California Public Utilities Commission approved the California Solar Initiative (CSI), a comprehensive $2.8 billion program that provides incentives toward solar development over 11 years;
2006	New World Record Achieved in Solar Cell Technology - New Solar Cell Breaks the ”40 Percent Efficient” Sunlight-to-Electricity Barrier;
2007	Construction of Nellis Solar Power Plant, a 15 MW PPA installation;
2007	The Vatican announced that in order to conserve Earth’s resources they would be installing solar panels on some buildings, in ”a comprehensive energy project that will pay for itself in a few years”;
2007	Google solar panel project begins operation;
2007	University of Delaware claims to achieve new world record in Solar Cell Technology without independent confirmation - 42.8% efficiency;
2007	Nanosolar ships the first commercial printed CIGS, claiming that they will eventually ship for less than $1/Watt. However, the company does not publicly disclose the technical specifications or current selling price of the modules;
2008	New record achieved in solar cell efficiency. Scientists at the U.S. Department of Energy’s National Renewable Energy Laboratory (NREL) have set a world record in solar cell efficiency with a photovoltaic device that converts 40% of the light that hits it into electricity. However, it was only under the concentrated energy of 326 suns that this was achieved. The inverted metamorphic triple-junction solar cell was designed, fabricated and independently measured at NREL;
2010	BP announces the closing of their photovoltaic plant in Maryland, moving all of their manufacturing work to China;
2010	President Barack Obama orders installation of additional solar panels and a solar hot water heater at the White House;
2011	Fast-growing factories in China push manufacturing costs down to about $1.25 per watt for silicon photovoltaic modules. Installations double worldwide;
2012	3D PV-cell with 30% more energy efficiency;
2013	After three years, the solar panels ordered by President Barack Obama were installed on the White House.

Appendix B

Appendix B: European Regulations, Standards, and Qualifications Tests

Regulations and standards

The European Union, since the late '70s, has been promoting research and development in photovoltaics in order to make this option a real energy resource and an opportunity for socioeconomic growth. Given the remarkable results obtained over more than 20 years, the European Council in 2003 promoted the establishment of a European Technology Platform for the sector with the following valuable goals:

- contribute to a rapid development of the European PV worldwide for the sustainable production of electricity;
- involve stakeholders (in this case companies and potential investors) in the formulation of research programs;
- establish a connection and coordination between industry, research and market.

The role of this European Council board is to prepare, support, and define the implementation of a coherent strategic plan that provides:

- mobilize all the participants for a long-term commitment on photovoltaics;
- implement the Strategic Research Agenda (SRA) of the European Photovoltaic for the next decade and give recommendations for its fulfillment;

- ensure the leadership of the European PV industry.

Overall, the European commitment in terms of research and development funding is mainly represented by the sum of loans and assets that each government independently decides to invest. Therefore, it does not imply a coordinated action between the different Member States.

At European level, several legislative acts define the policy of the Union industry. In particular:

- the 1997 White Paper aims to install 3GW of PV capacity by the end of 2010;
- the Green Paper of 2000, the objective of doubling the contribution of renewable energy from 6% to 12% by the end of 2010;
- Directive on energy production from renewable sources has the goal of bringing the contribution of renewables for electricity generation from 14% to 22% by the end of 2010.

The objectives to be achieved are then obvious: the diversification of energy sources and to ensure supplies: to contribute to the sustainable growth of the global economy and the development of countries; to develop a strong European high-tech industry in the field of renewable energy resources and ensure a leading role in the world [82].

As widely mentioned the desire to achieve a good degree of diversification in energy supply results in an increasing importance of renewable energy, which today are already at around 7%. This transition phase towards a future with an ensemble of different energy sources is the way that Italy and the European Union have decided to pursue in 2003. Moreover, the interest increased in March 2007, when the European Council divulged an action plan, which is called ”‘An Energy Policy for Europe”’. This plan, also known as *20 20 20*, requires a lot of efforts in order to achieve some important objectives by 2020, which are:

- reduction of the greenhouse gas emission by 20% compared to the reference values of 1990:
- reduction of energy consumption by 20% compared with today;
- use of renewable sources for a value of 20% of total consumption of primary sources.

The so called "'Position Paper"' of the Italian Government sets the maximum theoretical potential for renewable energy by 2020 in 20.97Mtoe[1], of which 8.96Mtep for electricity. In addition, besides the aforementioned dependence on imported fossil fuels, Italy is characterized by a singular energy framework, which presents:

- low energy intensity due to the discrete level efficiency in the productive sectors already reached in 1990 compared to the rest of the European Union, and the scarcity of energy-intensive industries;
- an extensive use of natural gas, which is the fossil fuel with the lowest specific content of carbon (205 $kgCO_2/MWh$);
- Individual Consumption content;
- hydraulic and geothermal resources available already fully exploited;
- limited availability of suitable sites for wind turbines and extensive olive biomass.

All these conditions make it difficult and expensive any further reduction of greenhouse gas emissions though.

The Italian economic development cannot disregard from heavy investments in research and technological innovation in the field of renewable energy sources. Among these, photovoltaics stands out with a high strategic potential value, which is now recognized even at the highest political levels. The actions of the government, in fact, push to the direction to encourage the development of a domestic industry. Thanks to the reformulation of the "'Conto Energia"' in February 2007, the opportunities of the Italian market are emerging and becoming more attractive for the industrial sector: at the end of 2007, the growth of installed PV system is evaluated in the order of 100% respect to the one recorded in 2006 (from 51MW recorded at the end of 2006 to more than 100MW at the end of 2007). The "'Position Paper"' also estimates a potential of 8500MW by 2020, of which 7500MW coming from "'building-integrated PV"' and 1000MW from "'solar power plants"'.

These needs and objectives point to move towards different technologies, which are able to compensate the lack of raw materials availability and the high cost of the system. The "'Photovoltaic Technology Research Advisory Council"' agree to consider thin-film

---

[1] The tonne of oil equivalent (toe) is a unit of energy: the amount of energy released by burning one tonne of crude oil, approximately 42 GJ (as different crude oils have different calorific values, the exact value of the toe is defined by convention; unfortunately there are several slightly different definitions).The toe is sometimes used for large amounts of energy, as it can be more intuitive to figure, the energy released by burning 1000 tonnes of oil than 42,000 billion joules (the SI unit of energy). Multiples of the toe are used, in particular the megatoe (Mtoe, one million toe) and the gigatoe (Gtoe, one billion toe). A smaller unit of kilogram of oil equivalent (kgoe) is also some times used denoting 0.001 toe. [83]

technologies and/or solutions which used concentrator systems to have more opportunities in the short/medium term. On the long run, the scenario is different: technologies based on quantum-dots structures, organic and photo-electrochemical cells could detain a remarkable share in the renewable energy market.

Qualification tests: CEI Standards

The Italian standard CEI EN 61646 1999 is entitled *Moduli fotovoltaici (FV) a film sottili per usi terrestri – Qualificazione del progetto e approvazione di tipo*. The standard outlines the requirements for the qualification of the project and approval of photovoltaic thin-film type to be used in long-term terrestrial applications and to operate in moderate climates outdoors. It was been written for the amorphous silicon technology, but it can also be applied to other thin-film PV modules. The purpose of the test is to determine the electrical and thermal characteristics of the module and to certificate that the module is able to withstand prolonged exposure in harsh climate conditions. Nevertheless, this standard does not apply to the modules used in systems with concentration and the CENELEC National Committees members agree with the internal rules of CEN/CENELEC to adopt this European Standard without any modification as a National Standard.

Therefore, the standard was meant to be used for amorphous silicon technology, but it can be applied to other thin film technologies. Then, the tests sequence may need to be modified regarding the characteristics of the technologies under examination. The tests sequence is based mostly on the EN 61215 standard for the qualification, the project, and the type approval of crystalline silicon photovoltaic modules for terrestrial applications. However, some changes were made accordingly the special characteristics of thin-film modules of amorphous silicon.

To highlight and separate the effects of degradation due to light exposure from other degradation mechanisms and to have the maximum power that the panels can supply, prolonged light exposure are used. The modules are annealed prior to thermal cycling and damp heat tests to separate the effects of annealing from other degradations due to these tests. For thin-film technologies different from amorphous silicon, the pre-treatment, such as prolonged exposure to light and annealing, may be different or even unnecessary. The standard provides compared to the previous addition of a test of leakage current in the wet environment since all types of thin-film modules are subject to corrosion due to moisture. The actual length of operation of the modules so qualified will depend on the goodness of their design , environment and conditions in which they are run .

The sampling devices are expected to be randomly selected eight modules (plus some spare) production according to the procedures indicated in the IEC 410. The modules must obviously have been manufactured using materials and components indicated in specification and in accordance with the drawings and process sheets so as not to invalidate the test. The standard requires that the modules should still be subject to normal inspection procedures, quality control and acceptance of the product provided by the manufacturer. It should be noted that they can be tested in experimental modules, too, not from an industrial production, provided that that is stated in the test report. The selected modules are then divided into groups and subjected to the sequence of qualification tests reported in Fig. B.1. Note that each block diagram section refers to the amount present in the standard.

Regarding to the tests of 10.2, 10.4, 10.6 and 10.7, it must be emphasized that the

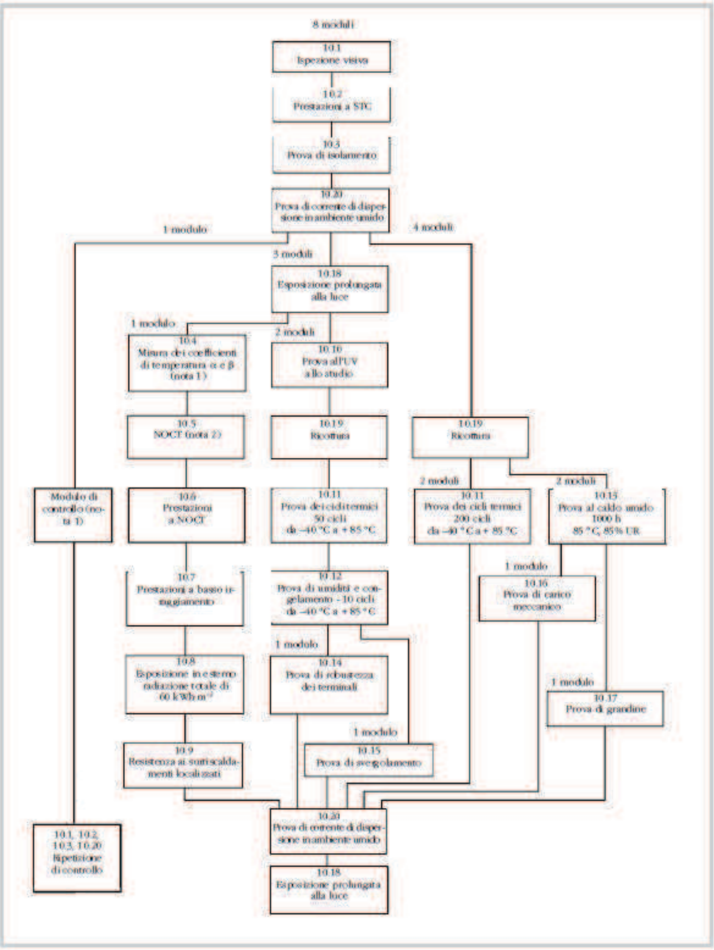

Figure B.1: Sequence of qualifying. Notes: May be omitted if alfa and beta are already known; If the modules are to be installed in the chassis, the NOCT (nominal cell operating temperature) can be replaced by the average equilibrium temperature of the junction of the cell in the normalized, with the module installed according to the manufacturer's instructions.
SOURCE: Statement of Italian CEI EN 61646.

procedures specified in EN 60891 relating to corrections to measured I-V characteristics as a function of temperature and radiation only apply to linear modules. If the module is not linear, these tests must be carried out within ± 5% of the radiation-specific and within ± 2°C temperature specification. Furthermore, any single test performed, regardless to the test sequences, has to preceded by the initial tests numbered as 10.1, 10.2, and 10.3.

Finally, to pass the qualification tests, and in turn to have the IEC approval, a module must meet all the following criteria:

1. the reduction of the maximum power output in standardized test conditions (STC) does not exceed the limit prescribed for each test;
2. after the last prolonged light exposure, the maximum output power STC is not less than 90% of the minimum value specified by the manufacturer in art. 4;
3. during the tests, on any specimen has not been detected any open-circuit or ground fault;
4. there is no visual evidence of a serious fault, as defined in art. 7;
5. meeting the requirements of the tests numbered as 10.3 and 10.20.

If two or more modules do not meet these standards of proof, it means that the project does not meet the requirements for qualification. Where it has been one module to not pass a test, two other modules that meet the requirements shall be subjected to the entire test sequence, starting from the beginning. If again one or both of these modules fails, it must be concluded that the project does not meet the requirements for qualification. If, however, both modules pass the test sequence, it must be concluded that the project meets the requirements for qualification [84].

Bibliography

[1] M. Gratzel. Dye-sensitized solar cell. *Journal of Photochemistry and Photobiology A*, 4:145–153, 2003.

[2] B. O'Regan and M. Gratzel. A low-cost, high-efficiency solar cell based on dye-sensitized colloidal tio2 films. *Nature*, 353:737–740, 1991.

[3] M. Gratzel. Photoelectrochemical cells. *Nature*, 414:338–344, 2001.

[4] M. K. Nazeeruddin, A. Kay, I. Rodicio, R. Humphry-Baker, E. Mueller, P. Liska, N. Vlachopoulos, and M. Graetzel. Conversion of light to electricity by cis-x2bis(2,2'-bipyridyl-4,4'-dicarboxylate)ruthenium(ii) charge-transfer sensitizers (x = cl-, br-, i-, cn-, and scn-) on nanocrystalline titanium dioxide electrodes. *Journal of the American Chemical Society*, 115:6382–6390, 1993.

[5] A. Hagfeldt and M. Gratzel. Light-induced redox reactions in nanocrystalline systems. *Chemical Reviews*, 95:49–68, 1995.

[6] `http://actu.epfl.ch/news/dye-sensitized-solar-cells-rival-conventional-ce-2/`.

[7] Fritts C. *Proc. Am. Assoc. Adv. Sci*, 33:97, 1883.

[8] Steven Hegedus Antonio Luque. *Handbook of Photovoltaic Science and Engineering.* March 2011.

[9] Niyazi Serdar Sariciftci Sam-Shajing Sun. *Organic Photovoltaics - Mechanisms, Materials, and Devices.* Taylor and Francis Group, 1996.

[10] D. M. Chapin, C. S. Fuller, and G. L. Pearson. A new silicon pn junction photocell for converting solar radiation into electrical power. *J. Appl. Phys.*, 25:676, 1954.

[11] Reynolds D. C. and et al. Photovoltaic effect in cadmium sulfide. *Physical Review*, 96:533, 534, 1954.

[12] Jenny D., Loferski J., and Rappaport P. *Physical Review*, 101:1208, 1209, 1956.

[13] Prince M. *J. Appl. Phys.*, 26:534 540, 1955.

[14] Loferski J. *J. Appl. Phys.*, 27:777–784, 1956.

[15] Wysocki J. and Rappaport P. *J. Appl. Phys.*, 31:571–578, 1960.

[16] Shockley W. and Queisser H. *J. Appl. Phys.*, 32:510–519, 1961.

[17] D.A. Cusano. Cdte solar cells and photovoltaic heterojunctions in ii-vi compounds. *Solid-State Electronics*, 6(3):217 – 218, 1963. ISSN 0038-1101. doi: http://dx.doi.org/10.1016/0038-1101(63)90078-9.

[18] Wysocki J. and et al. *Appl. Phys. Lett.*, 9:44–46, 1966.

[19] Alferov Zh. I. *Fiz. Tekh. Poluprovodn.*, 4:2378, 1970.

[20] Lindmayer J. and Allison J. *COMSAT Tech. Rev.*, 3:1–22, 1973.

[21] Hovel H. and Woodall J. Proc. 10th ieee photovoltaic specialist conf. 1973.

[22] Strong S. *Proc. 25th IEEE Photovoltaic Specialist Conf.*, pages 1197–1202, 1996.

[23] `http://en.wikipedia.org/wiki/Solar_power_by_country`.

[24] `http://www.nrel.gov/analysis/`.

[25] `http://en.wikipedia.org/wiki/Yingli`.

[26] `http://www.greentechmedia.com/articles/read/thin-film-solar-set-to-take-market-share-from-crystalline-solar-pv-1372/`.

[27] Fitzgerald M.C. and Mrohs M. High efficiency mono-crystalline solar cells with simple manufacturable technology. In *Proceedings: 21st European Photovoltaic Solar Energy Conference and Exhibition; Dresden, Germany*, 2006.

[28] Claudia Maggi. *Il fotovoltaico, stato dell'arte e aspettative*. Laboratorio Energia ERG, ENEA Bologna ARPA.

[29] `http://reneweconomy.com.au/2013/graph-of-the-day-current-solar-efficiencies-nowhere-nea`

[30] `http://www.greentechmedia.com/channel/solar`.

[31] Yang J., Banerjee A., and Guha S. Gate dielectrics for organic field-effect transistors: New opportunities for organic electronics. *Appl. Phys. Lett.*, 170:2977–2979, 1997.

[32] Hagedorn G. Hidden energy in solar cells and photovoltaic power stations. In *Proceedings: 9th European Photovoltaic Solar Energy Conversion; Freiburg, Germany*, 1989.

[33] `http://photonicsforenergy.spiedigitallibrary.org/article.aspx?articleid=1166247`, .

[34] `http://opticalengineering.spiedigitallibrary.org/article.aspx?articleid=1351688`, .

[35] Frerichs R. A solar grand plan. *Phys. Rev.*, 72:594–601, 1947.

[36] K. Zweibel, J. Mason, and V. Fthenakis. A solar grand plan. *Scientific American*, 67:1117–1127, 2008.

[37] M.A. Green, K. Emery, Y. Hishikawa, W.Warta, and E.D. Dunlop. Solar cell efficiency tables (version 42). *Progress in Photovoltaics: Research and Application*, 21:827–837, 2013.

[38] `http://investor.firstsolar.com/releasedetail.cfm?releaseid=755244`.

[39] Sinha P. Life cycle materials and water management for cdte photovoltaics. *Solar Energy Materials and Solar Cells*, 119:271–275, 2013.

[40] Max Marwede and Armin Reller. Future recycling flows of tellurium from cadmium telluride photovoltaic waste. *Resources, Conservation, and Recycling*, 69:35–49, 2012.

[41] Zweibel K. The impact of tellurium supply on cadmium telluride photovoltaics. *Science*, 328:699–701, 2012.

[42] B. L. Cohen. Anomalous behavior of tellurium abundances. *Geochim. Cosmochim. Acta*, 38:279–300, 1984.

[43] J. Hein, A. Koschinsky, and A. Halliday. Anomalous behavior of tellurium abundances. *Geochimica et Cosmochimica Acta*, 67:1117–1127, 2003.

[44] L.L. Kazmerski, F.R. White, and G.K. Morgan. *Appl. Phys. Lett.*, 46:268, 1976.

[45] `http://en.wikipedia.org/wiki/Copper_indium_gallium_selenide_solar_cells`, .

[46] Kronik L., Cahen D., and Schock H.W. Effects of sodium on polycrystalline cu(in,ga)se2 and its solar cell performance. *Advanced Materials*, 10:31–36, 1998.

[47] Neelkanth G. Dhere and Neelkanth G. Toward gw/year of cigs production within the next decade. *Solar Energy Materials and Solar Cells*, 91:15–16, 2007.

[48] `http://www.pv-tech.org/news/zsw_achieves_record_lab_cigs_cell_efficiency_of_20.8%`, .

[49] http://www.empa.ch/plugin/template/empa/3/131438/---/l=2.

[50] S. Anderson, E. C. Constable, and M. P. Dare-Edwards et al. Chemical modification of a titanium (iv) oxide electrode to give stable dye sensitisation without a supersensitiser. *Nature*, 280:571–573, 1979.

[51] P. Dare-Edwards, John B. Goodenough, Andrew Hamnett, Kenneth R. Seddon, and Raymond D. Wright. Sensitization of semiconducting electrodes with ruthenium-based dyes. *Faraday Discuss. Chem. Soc.*, 70:285–298, 1980.

[52] Md. K. Nazeeruddin, P. Pechy, and M. Gratzel. Efficient panchromatic sensitization of nanocrystallinetio2 films by a black dye based on atrithiocyanato–ruthenium complex. *Chem. Commun.*, 18:1705–1706, 1997.

[53] Md. K. Nazeeruddin, P. Pechy, and M. Gratzel. Engineering of efficient panchromatic sensitizers for nanocrystalline tio2-based solar cells. *J. Am. Chem. Soc.*, 123: 1613–1624, 2001.

[54] Kalyanasundaram K. and Gratzel M. Metal complexes as photosensitizers in photoelectrochemical cells. *Photosensitization and Photocatalysis Using Inorganic and Organometallic Compounds*, pages 247–271, 1993.

[55] G. Boscholoo and A. Hagfeldt. Characteristics of the iodide/triiodide redox mediator in dye-sensitized solar cells. *Accounts of chemical research*, 42:1819–1826, 2009.

[56] Smestad G., Bignozzi C., and Argazzi R. Testing of dye sensitized tio2 solar cells i: Experimental photocurrent output and conversion efficiencies. *Sol. Energy Mater. Sol. Cells*, 32:259–273, 1994.

[57] Smestad G., Bignozzi C., and Argazzi R. Testing of dye sensitized tio2 solar cells ii: Experimental photocurrent output and conversion efficiencies. *Sol. Energy Mater. Sol. Cells*, 32:273–288, 1994.

[58] Hagfeldt A. and Gratzel M. Molecular photovoltaics. *Acc. Chem. Res.*, 33:269–277, 2000.

[59] Zaban A., Ferrere S., and Gregg B. Relative energetics at the semiconductor/sensitizing dye/electrolyte interface. *J. Phys. Chem.*, 102:452–460, 1998.

[60] Julie M. Rehm, George L. McLendon, Yutaka Nagasawa, Keitaro Yoshihara, Jacques Moser, and Michael Gratzel. Femtosecond electron-transfer dynamics at a sensitizing dye-semiconductor (tio2) interface. *J. Phys. Chem.*, 100:9577–9578, 1996.

[61] Kamat P., Bedja I., Hotchandani S., and Patterson L. Photosensitization of nanocrystalline semiconductor films. modulation of electron transfer between excited ruthenium complex and sno2 nanocrystallites with an externally applied bias. *Synth. Met.*, 100:4900–4908, 1996.

[62] Randy J. Ellingson, John B. Asbury, Sue Ferrere, Hirendra N. Ghosh, Julian R. Sprague, Tianquan Lian, and Arthur J. Nozik. Dynamics of electron injection in nanocrystalline titanium dioxide films sensitized with [ru(4,4'-dicarboxy-2,2'-bipyridine)2(ncs)2] by infrared transient absorption. *J. Phys. Chem. B*, 102: 6455–6458, 1998.

[63] K Hara andT Horiguchi, T Kinoshitab, K Sayama, and H Arakawa. Influence of electrolytes on the photovoltaic performance of organic dye-sensitized nanocrystalline tio2 solar cells. *Sol. Energy Mater. Sol. Cells*, 70:151–161, 2001.

[64] Vlachopoulos N., Liska P., Augustynski J., and Gratzel M. Very efficient visible light energy harvesting and conversion by spectral sensitization of high surface area polycrystalline titanium dioxide films. *J. Am. Chem. Soc.*, 110:1216–1220, 1988.

[65] Liu Y., Hagfeldt A., Xiao X., and Lindquist S. Investigation of influence of redox species on the interfacial energetics of a dye-sensitized nanoporous tio2 solar cell. *Sol. Energy Mater. Sol. Cells*, 55:267–281, 1998.

[66] Greg P. Smestad. Education and solar conversion:: Demonstrating electron transfer. *Solar Energy Materials and Solar Cells*, 55:157–178, 1998.

[67] `http://infoscience.epfl.ch/record/64348`.

[68] M. Liberatore, F. Decker, L. Burtone, V. Zardetto, T.M. Brown, A. Reale, and A. Di Carlo. Using eis for diagnosis of dye-sensitized solar cells performance. *J Appl Electrochem*, 39:2291–2295, 2009.

[69] T. Halme, P. Vahermaa, K. Miettunen, , and Peter Lund. Device physics of dye solar cells. *Adv. Mater*, 22:210–234, 2010.

[70] Liyuan Han, Naoki Koide, Yasuo Chiba, and Takehito Mitate. Modeling of an equivalent circuit for dye-sensitized solar cells. *Appl. Phys. Lett.*, 84:2433–2435, 2004.

[71] W. Qing, Moser J., and Gratzel M. Electrochemical impedance spectroscopic analysis of dye-sensitized solar cells. *J. Phys. Chem. B*, 109:14945–14953, 2005.

[72] *Standards, IEC 60904-9 Photovoltaic devices – Part 9: Solar Simulator Performance requirements*. edition 2.0, 2007.

[73] S. Kohraku and et al. New method for solar cell measurement by led solar simulator. *3nd World Conference on Photovoltaic Energy Conference*, pages 1977–1980, 2003.

[74] J. Bisquert. Theory of the impedance of charge transfer via surface states in dye-sensitized solar cells. *Journal of Electroanalytical Chemistry*, 646:43–51, 2010.

[75] M. Gratzel. Conversion of sunlight to electric power by nanocrystalline dye-sensitized solar cells. *Journal of Photochemistry and Photobiology A*, 164:3–14, 2004.

[76] M. Gratzel. Perspective for dye-sensitized nanocrystalline solar cells. *Progress in Photovoltaics*, 8:171–185, 2000.

[77] H. Desilvestro, M. Bertoz, S. Tulloch, , and G. Tulloch. Packaging scale up and commercialization of dye-sensitized solar cells. *EPFL Press*, 2010.

[78] H. Matsui, K. Okada, T. Kitamura, , and T. Tanabe. Thermal stability of dye-sensitized solar cells with current collecting grid. *Solar Energy materialsand Solar Cells*, 93:6–7, 2009.

[79] B. Macht, M. Turrion, A. Barkschat, P. Salvador, K. Ellmer, , and H. Tributsch. Patterns of efficiency and degradation in dye sensitization solar cells measured with imaging techniques. *Solar Energy Materials and Solar Cells*, 73:163–173, 2002.

[80] Olsen E. et al. Preparation of tio2 films by layer-by-layer assembly and their application in solar cell. *Sol. Energy Mater. Sol. Cells*, 63:267–273, 2000.

[81] `http://en.wikipedia.org/wiki/Timeline_of_solar_cells`.

[82] Anna De. Lillo. *DOSSIER, Enea per il Fotovoltaico.* Roma, 2006.

[83] `http://en.wikipedia.org/wiki/Tonne_of_oil_equivalent`.

[84] CEI-EN61646. *Moduli fotovoltaici (FV) a film sottili per usi terrestri - Qualificazione del progetto e approvazione di tipo.* Gennaio 1999.